DEPARTAMENTO DE ASTROFISICA

Universidad de La Laguna

Bayesian analysis of the solar corona

Memoria que presenta
Dña. María Montes Solís
para optar al grado de
Doctora por la Universidad de La Laguna.

Director: Dr. Iñigo Arregui Uribe-Echevarría
Tutor: Dr. Manuel Collados Vera

INSTITUTO Đ ASTROFISICA Đ CANARIAS
marzo de 2019

Examination date: Mayo, 2019
Thesis supervisor: Dr. Iñigo Arregui Uribe-Echevarría
Thesis tutor: Dr. Manuel Collados Vera

Part of the material included in this document has been published in *The Astrophysical Journal* and *Astronomy & Astrophysics*

A la gente que no miente.

Agradecimientos

En primer lugar, quiero dar las gracias a mi director de tesis, Iñigo Arregui y a mi tutor, Manuel Collados, por darme la gran oportunidad de realizar esta tesis cuando mis esperanzas de dedicarme a la investigación ya se estaban desvaneciendo. En especial, agradecer a Iñigo toda su dedicación, preocupación, sinceridad, tiempo y apoyo en todo este camino recorrido. A pesar de todo el trabajo y los dolores de cabeza que seguro que le he ocasionado, espero que no desista de seguir educando mentes y seguir formando, a lo que a mi entender, son buenos investigadores. Aunque no he tenido mucho contacto con todos los integrantes, quiero dar las gracias también a todo el grupo de física solar del Instituto de Astrofísica de Canarias por su acogimiento y respeto.

Me gustaría también felicitar al grupo de física solar de la Universitat de les Illes Balears, por su calidad científica pero, sobre todo, por la calidad humana de todos sus integrantes: José Luis Ballester, Ramón Oliver, Roberto Soler, Jaume Terradas, Andrés Androver, en su día David Martínez Gómez (ahora en nuestro bando del IAC); y como no, Marc Carbonell. A todos ellos, gracias por la gran acogida en mi visita a Mallorca y en posteriores encuentros.

And good people is what I found in the solar and magnetospheric theory group of St. Andrews University. Although I spent only three weeks there, I could see a great working environment in which everybody work together as one. They did not hesitate to help me every time I needed it. Thanks Ineke De Moortel for your kindness and the opportunity to live that experience.

Pero sin duda, mis mayores agradecimientos van dedicados a mis padres. Por el apoyo que me han mostrado siempre para seguir adelante con cualquier cosa que me gustase y el esfuerzo que ha supuesto para ellos que yo haya podido llegar hasta aquí. Sobretodo, quiero darles las gracias por darme principios, confiar en mi para conseguir lo que me propongo y convertirme en la persona que soy. Aunque a veces supone ir a contra corriente, puedo dormir tranquila con lo que hago. En cuanto a mi hermana, que voy a decir de ella, salvo que ha sido mi gran compañía en la vida desde que llegó a casa con sus mofletes. Aunque haya distancia entre nosotras y siga haciendo de las suyas, siempre estaremos juntas de una forma u otra.

Luis, aparte de las gracias, quiero dedicarte un gran aplauso por el empeño que pusiste en que solicitase este trabajo y el que has puesto en animarme durante toda la tesis. Desde el principio has sido un gran apoyo. Por todo, por las risas, por los lloros y por la monocicleta, ¡muchas gracias!

Y por qué no, quiero dar gracias a todos aquellos que no creyeron en mi, me criticaron, ignoraron, y que así, me impulsaron a tener más determinación y éxito en la consecución de mis metas.

Por último, agradecer al Ministerio de Ciencia, Innovación y Universidades la concesión de la ayuda asociada a la contratación para la formación de doctores en centros Severo Ochoa y unida al proyecto SEV-2011-0187-03: "Física solar", gracias a la cual esta tesis ha sido posible.

Resumen

A pesar de los últimos avances hechos en instrumentación para obtener datos y el desarrollo de nuevas técnicas para analizarlos, la corona solar es una de las regiones del Sol con más incógnitas por resolver. Son necesarios nuevos métodos que permitan la comparación entre las observaciones y los modelos teóricos o numéricos para desvelar las condiciones y los procesos físicos que tienen lugar en esta región de la atmósfera solar.

Esta tesis pretende dar un paso adelante en el desarrollo de esos métodos mediante la elaboración de herramientas basadas en estadística bayesiana. La estadística bayesiana, en comparación con otro tipo de estadística, permite incluir la información de la que se dispone previamente a las mediciones y permite también incluir todo tipo de incertidumbres al estudio, además de las propias observaciones. Así, un análisis bayesiano de la corona hace posible la obtención de la probabilidad de que ciertos parámetros físicos tomen determinados valores o inferencia, comparar la plausiblidad de que distintos modelos expliquen lo observado y predecir la probabilidad de nuevas observaciones.

La tesis se centra principalmente en estudios de sismología coronal, en la que se comparan observaciones y modelos teóricos de ondas magnetohidrodinámicas. En particular, nos hemos centrado en el estudio de las ondas transversales en dos estructuras principales de la corona: los bucles coronales y los filamentos que conforman la estructura fina de las prominencias.

En el caso de los bucles coronales, hemos inferido en primer lugar los valores más probables del campo magnético que los define y su dependencia con la densidad del bucle. Además, hemos inferido el contraste de densidad entre el medio circundante o corona y el bucle, así como otros parámetros ligados a su estructura. También hemos calculado la plausibilidad de los mecanismos de absorción resonante, mezcla de fases y fuga de ondas, en explicar el amortiguamiento de las ondas transversales soportadas. Con esto último, hemos obtenido que ninguno de ellos parece explicar todas las observaciones. La evidencia depende en gran medida de los valores concretos del período de la onda y el tiempo de amortiguamiento que se miden; y dependen además de sus incertidumbres. Finalmente, hemos considerado la absorción resonante de ondas de las propagación para ver las evidencias resultantes de comparar un perfil de amortiguamiento exponencial con otro Gaussiano, pero en principio, ninguno de los perfiles es más adecuado que el otro en lo que respecta a los bucles coronales.

En lo que respecta a las prominencias, hemos obtenido también los valores más probables del campo magnético que define a sus filamentos. A continuación, hemos considerado el cociente entre el modo fundamental y el primer

armónico de las ondas transversales, para inferir el contraste de densidad de estas estructuras, así como la longitud de los filamentos. Cuando el modelo para el cociente de períodos en la aproximación de filamentos cortos se compara con el mismo modelo en la aproximación de filamentos largos, los resultados indican que cocientes entre períodos con valores entorno a la unidad son mejor explicados por la aproximación de filamentos largos, mientras que el resto de valores es más plausible cuando se considera la aproximación de filamentos cortos. Además de esto, hemos considerado un modelo que incorpora el efecto de los flujos de masa, para inferir la longitud total de los tubos de flujo de contienen el filamento. Después, hemos considerado los modelos de absorción resonante en el continuo de Alfvén, absorción resonante en el continuo lento y difusión de tipo Cowling, para inferir los parámetros asociados a ellos; así como calcular su plausibilidad a la hora de explicar las observaciones. El mecanismo que parece explicar el amortiguamiento de ondas transversales es claramente la absorción resonante en el continuo de Alfvén. Por último, cuando comparamos los perfiles exponenciales y Gaussianos de amortiguamiento en los filamentos, las evidencias de uno u otro dependen de los valores particulares de la longitud de amortiguamiento y la longitud de onda.

Finalmente, hemos presentado las futuras líneas de investigación que pueden derivarse de esta tesis.

Abstract

In spite of the instrumental improvements to acquire data and the new techniques developed to analysed them, the solar corona is one of the regions of the Sun with more unresolved questions. New methods to compare between observations and theoretical or numerical models are necessary to reveal the main physical conditions and processes of this atmospheric layer.

This thesis entails a step further those methods development through the elaboration of new tools based on Bayesian statistics. Contrary to others type of statistics, the Bayesian approach permits to include in our analyses observations, prior information before taking data, as well as all kind of uncertainties. Hence, Bayesian analyses about the solar corona allow the inference of physical parameters, the comparison between models by computing their associated plausibility, and further predict new observations.

The thesis is performed within the coronal seismology context, in which observations and magnetohydrodynamical models are confronted. In particular, we have centred on the study of transversal waves supported by two coronal structures: coronal loops and prominence threads.

Regarding coronal loops, we have first inferred the most probable values of the magnetic field strength and how it depends with the internal density. Moreover, we have inferred the density contrast between the surrounding corona and the loop densities, as well as other structural parameters. We have further computed the plausibility of resonant absorption, phase mixing, and wave leakage mechanisms in explaining the observed damping of transverse waves. Our results indicate that none of these mechanisms explains all the observations. The evidence depends on the particular values of the measured wave period and damping time, and also on their uncertainties. Finally, we have considered resonant absorption of propagating waves to compare the evidence by assuming an exponential decay and a Gaussian one. In principle, none of these profiles seem to be more adequate than the another in explaining the data.

Concerning to prominence threads, we have first obtained the most probable values of the magnetic field strength. Secondly, we have considered the ratio between the fundamental mode period and that of the first overtone in transverse waves, to infer the density contrast, as well as the length of the threads. When we have compared models of period ratios under the short and long thread approximations, the results indicate that period ratios around unity are better explained by the long thread approximation, while the rest of period ratio values are more likely for the short thread approximation. Next, we have assumed a model that includes a mass flow contribution, in order to infer the total length of flux tubes containing threads. Furthermore, we have

selected resonant absorption in the Alfvén continuum, resonant absorption in the slow continuum, and Cowling's diffusion as damping mechanisms. We have inferred their corresponding parameters and we have performed a plausibility comparison between them. Clearly, resonant absorption in the Alfvén continuum is the most plausible mechanism in explaining the damping process for threads. Lastly, we have considered resonant absorption in the Alfvén continuum of propagating waves to compare evidences of an exponential decay and a Gaussian one. Differently to coronal loops, the evidence for each profile depends on particular observed values of damping lengths and wavelengths.

To finish, we have posed some future work that derives from this thesis within coronal studies.

Contents

1

Introduction

We can only see a short distance ahead,
but we can see plenty there that needs to be done.
Alan Turing (1950)

The Sun is an almost spherical structure of plasma that is far away from being a normal or boring star. It supports life on Earth from a distance of ∼150 mill km and constitutes a laboratory where the study of extreme physical conditions help us to extend our knowledge in plasma physics, specially in solar like stars, and their effect on planets.

The Sun is classified as a main sequence G2-type star in the Hertzsprung-Russel diagram, with a mass of $M_\odot = 1.99\times10^{30}$ kg, a radius of $R_\odot = 6.96\times10^5$ km, and a composition of about 90% hydrogen, 10% helium, and some traces of heavier elements.

Theoretically, the main mechanisms that support the Sun is the transformation process of hydrogen into helium that takes place at the nucleus, together with a balance between pressure and gravity forces, so that they will maintain the Sun alive five billion years more. That global process can not be directly measured, so that the study of the Sun is based on different observations of the solar atmosphere.

The solar atmosphere is divided in four principal layers based on different observational and physical properties: photosphere, chromosphere, transition region, and corona (see Fig. 1.1). The study of the corona has been motivated in the last years by observations with space telescopes, since it had remained almost hidden before, due to the inherent difficulty to observed it. It is precisely this region of the solar atmosphere where this thesis is focused on, thus we

will describe in Section 1.1 some of its main features. How the use of coronal seismology helps to better understand this atmospheric layer will be exposed in Section 1.2. We will continue describing the main current problems in coronal seismology and the principal studies that are being considered to solve them in Section 1.3. Finally, in Section 1.4 we will describe how this thesis aims at contributing to the solution to the current problems and a brief outline of it.

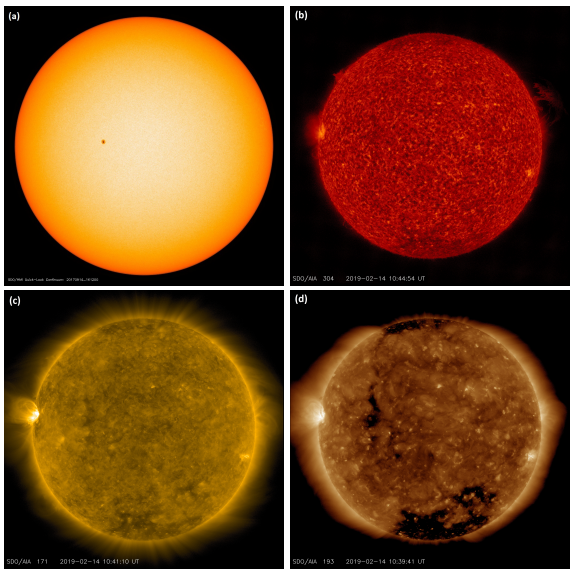

Figure 1.1: Images of different layers of the solar atmosphere from the Helioseismic and Magnetic Imager (HMI) and the Atmospheric Imaging Assembly (AIA) on board the Solar Dynamics Observatory (SDO) in February 14^{th}, 2019 (https://sdo.gsfc.nasa.gov/data/). Panel (a) shows the intensitygram with high cadence, panel (b) the upper chromosphere and lower transition region in the 304 Å channel, panel (c) presents the quiet corona and upper transition region in the 171 Å channel, and panel (d) the corona and hot flare plasma in the 193 Å channel.

1.1 The Corona

The solar corona is the outer and less dense layer of the solar atmosphere reaching up the limits of the solar system. Due to its weak emission in the

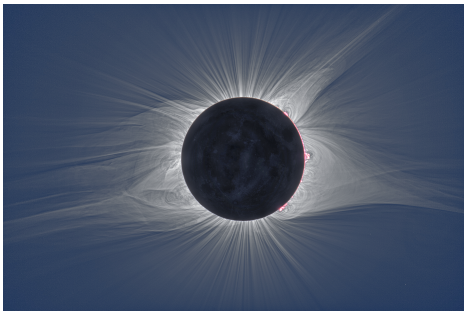

Figure 1.2: Image of the solar corona during the last total eclipse in August 21^{th}, 2017. (*© 2017 Miloslav Druckmüller, Marcel Bělík, Radovan Mrllák, Shadia Habbal*)

visible part of the solar spectrum in comparison to the rest of the atmosphere, the corona is invisible to the naked eye except during total eclipses (Fig. 1.2), when it appears like a crown, hence its name. In spite of the multiple observations of eclipses since Babylonian times (Guillermier & Koutchmy 1999), it was not until the 19th century, when first solar spectra were obtained, that this layer of the atmosphere was considered real. In the following years, new coronal lines associated to highly ionised elements were detected thanks to the invention of the spectroheliograph by George Ellery Hale and the coronagraph by Bernard Lyot. These detections reported the appearance of an unknown element baptised as *coronium* in 1869. However, in 1942 Edlén established that the *coronium* was in reality a highly ionised iron, giving the first estimation of the coronal temperature in million degrees kelvin and hence, representing a breaking point in solar studies. Since then, space-telescopes have permitted to obtain coronal images in other wavelengths, particularly in radio, X-rays (RX), and extreme ultraviolet (EUV) with satellites such as the Transition Region And Coronal Explorer (TRACE), Hinode, the Solar Dynamics Observatory (SDO), and the Parker Solar Probe.

Space observations have allowed us to know that the corona is highly inhomogeneous and dynamic on essentially all spatial and temporal scales, with plasma being controlled by the magnetic field behaviour. Coronal temperatures are high enough to be the plasma fully ionised, causing that thermal conduction occurs almost entirely along the magnetic field. Hence, the solar corona can be divided in two main components according to regions and structures where the magnetic field lines appear to be open or closed. The *open corona* is composed by coronal holes, which correspond to regions with low density observed as large

dark areas of the coronal disk and lasting from weeks to months (Fig. 1.1d). On the other hand, we also find thin streamers inside those coronal holes named *polar plumes* which are the source of the fast solar wind. Finally, the *closed corona* is mainly composed by coronal loops and other closed structures. It is the source of the slow solar wind.

Although under this division the corona could appear simple, both the open and closed components display structural and dynamical properties that despite their majestic appearance in observations, are difficult to define, classify, and study. In the following, we will briefly describe those coronal structures of relevance to this thesis.

Coronal Loops

Coronal loops are the basic components of the closed solar corona. These structures are believed to be composed by hot and dense magnetic flux tubes. Their length ranges from a few kilometres to several solar radii. They extend over the whole corona (except for coronal holes) connecting photospheric regions with different magnetic polarity.

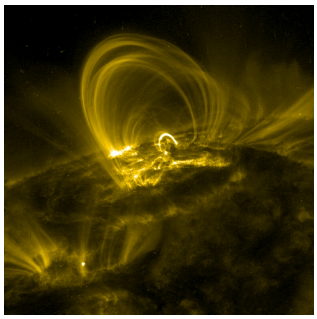

Figure 1.3: An example of coronal loops observed by TRACE in 2005, 171 Å filter.

Coronal loops are observable in EUV (Fig. 1.3), but the bulk of coronal loops is visible in X-ray wavelengths. Depending on the filter used to observe coronal loops, they can be classified as *cool loops* corresponding to arcs with temperatures in between 0.1 to 1 MK, *warm loops* with temperatures from 1 to 1.5 MK, and *hot loops* with temperatures above 2 MK. A given active region is usually highly multi-thermal, composed of the three cool, warm, and hot loops. Coronal loops can be found under different appearances apart from arcs, such as helmets or forming tunnel structures. In fact, they are rarely found in isolation.

Physical parameter	Values
Plasma temperature	T = 0.1 - > 2 MK
Electron density	$n_e = 10^8$ - 10^{10} cm^{-3}
Gas pressure	p = 0.1 - >100 dyn cm^{-2}
Length of loop	L ≈ 1 - 1000 Mm
Width of loop	w ≈ 5.5 - 16.8 Mm
Height of loop	h ≈ km - $R_\odot$
Filling factor	q_{fill}= 0.2 - 0.9
Width of threads	d_{thread} = 10 - 100 km
Oscillation frequency	P = 1 - 10 min
Magnetic field strength	B = 0.1 - 100 G
Flow velocity	v > 10 km s^{-1}

Table 1.1: Common coronal loop properties compiled from Aschwanden (2005); Reale (2014).

Despite the complexity of these structures, coronal loops are commonly characterised by cylindrical tubes totally filled of hot and dense plasma with almost no expansion in height and a constant and circular cross-section. However, low filling factors have been detected in these structures with high resolution imaging. Since thermal conduction perpendicular to magnetic lines is almost negligible, it is thought that coronal loops can be composed by threads as thin as those magnetic field lines not resolved by current instrumentation, instead of being monolithic tubes of plasma. Table 1.1 shows some typical values for coronal loop physical parameters. The large range of some parameter values is a manifestation of the great variety of coronal loop properties and of the difficulty for identifying what a coronal loop is. In addition, projection effects, overlapping of several structures along the line of sight, imaging resolution, etc make a challenge to directly measure coronal loop properties and the characteristics of their dynamics.

Prominences

Solar prominences or filaments are long structures of cool and dense material suspended in the surrounding corona, similarly to clouds in the Earth atmosphere. They are anchored to the photosphere (Fig. 1.4) and are long-lived with characteristic lifetimes ranging from a few hours to months.

Prominences are observed in chromospheric lines such as H_α 6562.8 Å or in HeII 304 Å, since the temperature of prominence plasma is so low that it is only partially ionised. While quiescent prominences are very stable as a whole and last for long times permitting their better characterisation observationally;

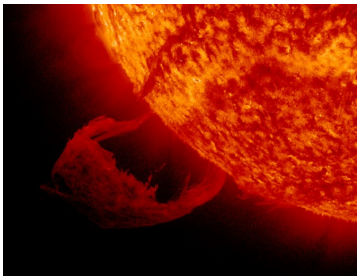

Figure 1.4: Example of a prominence observed in 2012 by SDO, 304 Å filter.

active region prominences are shorter, denser, and more dynamic, so their parameters are worse determined. Common observed features of these solar structures can be found in Table 1.2.

As in the case of coronal loops, prominences present many different plasma conditions and forms, like tornado ones, and their fine structure consists of myriads of threads. However, this fine structure is poorly understood because threads show dynamical processes affecting individually to each fibril or small groups of them, so how all threads together are coupled to create such a stable structure and how their changes affect the whole prominence is one of the many unsolved questions in prominence studies.

Their imposing appearance from early observations of the corona and their stability against the gravity, makes prominences one of the most impressive coronal structures. It is not well understood neither how they remain there, nor how their are formed, evolve, disappear, etc.

Physical parameter	Values
Electron density (at T = 0.1 MK)	$n_e = 1.3 \times 10^9$ - 3×10^{11} cm^{-3}
Gas pressure (at T = 0.1 MK)	p = 0.03 - 0.38 dyn cm^{-2}
Length of prominence	L $\approx$ 60 - 600 Mm
Width of prominence	w $\approx$ 4 - 30 Mm
Filling factor	q_{fill} = 0.001 - 0.1
Length of threads	L_{thread} = 5 - 35 Mm
Width of threads	d_{thread} = 200 - 400 km
Oscillation frequency	P = 3 - >40 min
Magnetic field strength	B = 4 - 40 G
Flow velocity (at T = 0.1 MK)	v = 2 - 13 km s^{-1}

Table 1.2: Common prominence properties collected by Aschwanden (2005).

Flares

Flares are huge energy releases that convert magnetic energy into heat, light, and accelerate particles of plasma (Fig. 1.5). They are the result of magnetic reconnection processes with energies reaching $\approx 10^{33}$ erg or more. They exist in many scales getting the name *microflare* when the energy is $\approx 10^{-6}$ times the energy of a strong flare, *nanoflare* with 10^{-9} of the energy, and *picoflares* with 10^{-12} times the flare energy. Strong flares can be responsible for many phenomena, such as coronal mass ejections (CMEs), oscillations or collisions between adjacent structures. However, small ones should not be despicable in coronal studies, since they take place with higher frequency than stronger ones, assuming a great role in the energy balance of the corona.

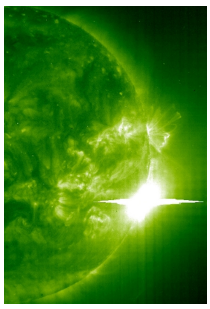

Figure 1.5: Example of a flare observed in 2003 by SOHO, 195 Å filter. *Credit: ESA&NASA/SOHO.*

The detection of flares is performed by observations in multiple wavelength ranges: radio, optical, EUV, X-rays, and gamma rays. They are normally classified by the total output of soft X-rays detected during one of these phenomena with letters B, C, M, and X assigned to increasing intensities (see e.g. Golub & Pasachoff 1997).

Their importance in solar physics resides in their possible role in the coronal energy budget and in solar storms affecting the Earth. Nevertheless, the answers to questions like where the energy is stored before and how is liberated are still unknown.

In spite of the existence of numerous studies of coronal structures, direct measurements of their magnetic fields and plasma parameters is a challenge due to intrinsic spatial and temporal complexity, but also because of limitations in observations, such as projection effects or the absence of accurate spectroscopic measurements. Methods to indirectly determine parameters and to improve the

accuracy of measurements in coronal structures are still needed.

For more information about the general structure of the corona and more specific studies of coronal loops, prominences, and flares, the reader is referred to Tandberg-Hanssen (1995); Golub & Pasachoff (1997); Aschwanden (2005); Reale (2014) and references therein.

1.2 Coronal Seismology

Since early detections (Tsubaki 1988), the ubiquity of coronal oscillations has become evident. Multiple oscillatory phenomena have been observed in coronal structures, specially in coronal loops and prominences. In coronal loops, several types of waves have been reported from first signs in radio emission (Aschwanden 1987). Slow propagating oscillations with velocities around 70 - 165 km s^{-1} and periods of 180 - 240 s (see e.g. Nightingale et al. 1999; De Moortel et al. 2000) are an example of those supported waves, but also fast propagating oscillations with projected speed of 1 - 4 Mm s^{-1} and 5 min periods (Tomczyk et al. 2007; Tomczyk & McIntosh 2009). Additionally, standing oscillations are displayed, mainly in the form of flare-excited transversal oscillations and involving fast (Aschwanden et al. 1999; Wang et al. 2002, 2003, see e.g.) or even slow (Wang et al. 2003) movements. Although the majority of these flare-excited oscillations in coronal loops are observed to be damped (see e.g. White & Verwichte 2012a; Nisticò et al. 2013; Anfinogentov et al. 2013, 2015), detections of amplification (Wang et al. 2012) or no modulation (Aschwanden & Schrijver 2011) have been also stated. Regarding prominences, a great evidence of all types of prominence oscillations also exists (Arregui et al. 2018): transverse modes (see e.g. Lin 2004; Lin et al. 2009; Okamoto et al. 2007; Ning et al. 2009), motions along the prominence axis (Vršnak et al. 2007), large amplitude oscillations (Isobe & Tripathi 2006; Tripathi et al. 2009), etc. For an extension of coronal wave observations, see e.g. reviews by Roberts (2000); Aschwanden et al. (2002); Aschwanden (2006); De Moortel & Nakariakov (2012); Arregui et al. (2012, 2018).

For explaining those coronal oscillations, magneto-hydrodynamic (MHD) theory has been developing and evolving since first theoretical studies by Edwin & Roberts (1983) and Roberts et al. (1984). Hence, slow longitudinal oscillations supported by coronal loops respond to features of slow magneto-acoustic waves (Nakariakov et al. 2000) with drivers in foot-points (De Moortel et al. 2002b), while fast propagating and standing oscillations respond to kink modes (Nakariakov et al. 1999; Aschwanden et al. 2002; Van Doorsselaere et al. 2008a; Goossens et al. 2011). For this latter type, several theoretical models have been developed to understand how oscillatory features change with different mod-

ifications of monolithic models commonly assumed, such as a longitudinally stratified density (Andries et al. 2005), expansion of the flux tube (Verth & Erdélyi 2008), and density profile (Soler & Terradas 2015). Many mechanisms were also proposed to explain their rapid damping, but studies rapidly focused on resonant absorption (Goossens et al. 2002; Ruderman & Roberts 2002b; Goossens et al. 2006; Terradas et al. 2010; Pascoe et al. 2010), phase mixing (Heyvaerts & Priest 1983), and wave leakage (Spruit 1982; Cally 1986, 2003; Berghmans & de Bruyne 1995). However, a clear evidence of any of those damping models explaining observations does not exist, in spite of the efforts made to clarify the issue (see e.g. reviews by Roberts 2000; Nakariakov & Verwichte 2005; Ruderman 2005; Aschwanden 2005). Even so, studies centred their attention on resonant absorption and analysed the effects of considering curvature in flux tubes (Van Doorsselaere et al. 2004; Van Doorsselaere et al. 2009; Terradas et al. 2006), non-circular cross-section (Ruderman 2003), various density profiles (Arregui et al. 2007; Soler et al. 2014), or effects of a non-exponential decaying profile (Pascoe et al. 2012; Hood et al. 2013; Pascoe et al. 2013). Concerning prominences, a wide variety of models for not only global waves, but also local waves have been created for explaining observations. In particular, prominence threads conforming their fine structure are normally described as a denser part of a longer flux tube (Díaz et al. 2002; Dymova & Ruderman 2005). From that point, some studies have included different ingredients to it, such as partial ionisation effects and flows (Soler et al. 2009b; Soler et al. 2009; Soler & Goossens 2011; Ballester et al. 2018). In view of the results, several theoretical models considered for coronal loops are also valid for any wave-guide in general, including prominence threads. Hence, when damping mechanisms are analysed in these structures, the resonant absorption mechanism seems to be the most likely in explaining observations in prominence threads (Arregui & Ballester 2011).

Both oscillatory observations and results from theoretical models opened a new window for searching information of the entire corona, through the use of coronal seismology. Coronal seismology encompasses the study of waves in the solar corona confronting the observations with MHD theory to recover physical quantities that are not directly observed and are of interest for the comprehension of coronal plasma physics (Fig. 1.6). The concept of coronal seismology was first suggested by Uchida (1970) and Roberts et al. (1984). However, the application of this discipline to solar physics was very limited until observations of coronal oscillations were available. Since then, the situation changed drastically, being coronal seismology rapidly transformed from a theoretical possibility to a viable technique.

First estimations using coronal seismology came from the hand of Aschwan-

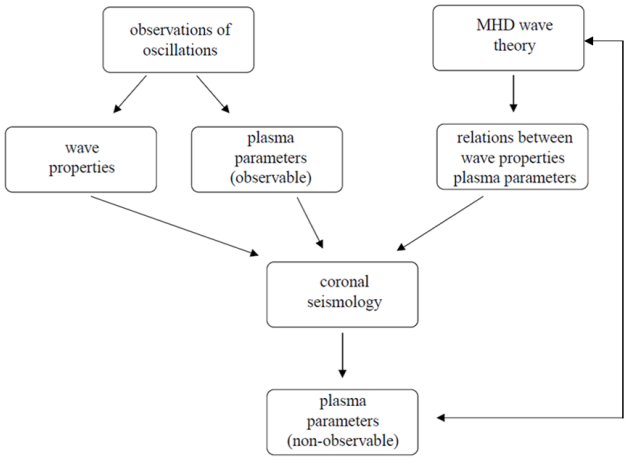

Figure 1.6: Sketch of the coronal seismology method by De Moortel (2005).

den et al. (1999) and Nakariakov & Ofman (2001) works, by using EUV imaging capabilities of TRACE. They used the definition of kink modes and the observed transverse oscillations to derive the magnetic field strength and damping times of those coronal loop oscillations. From those first estimations, the search for more accurate measurements of the magnetic field strength and other physical quantities of coronal loops, prominences and the corona in general has never stopped. For example, Van Doorsselaere et al. (2008a) used spectroscopic data together with imaging by Hinode to obtain a better estimation of the magnetic field strength, and Verwichte et al. (2009) searched for a better characterisation of coronal loops shape with STEREO data. Also of interest, De Moortel et al. (2002a) determined that periods, damping coefficients and decay exponent can be computable if the necessary number of oscillations is observed in a wavelet analysis. Contemporaneously, Terradas et al. (2002) inferred wave properties by obtaining two-dimensional maps of the amplitude distribution in coronal loops, and Goossens et al. (2002) analysed coronal loop properties by assuming resonant absorption as damping mechanism. Other studies have focused on computing the coronal Alfvén speed (Zaqarashvili 2003; Arregui et al. 2007; Goossens et al. 2008), the density scale height (Andries et al. 2005; Verth & Erdélyi 2008; Andries et al. 2009), information by considering multiple har-

monics (Andries et al. 2005; Van Doorsselaere et al. 2007), propagating waves (Goossens et al. 2012), etc. Practically all theoretical descriptions have been accompanied by a comparison with observational data, even for prominence threads (Lin et al. 2009). For a more extensive description of coronal seismology accomplishments see e.g. Goossens et al. (2008); Nakariakov (2008); Arregui et al. (2012); Andries et al. (2005) and De Moortel & Nakariakov (2012).

1.3 Role of Bayesian Statistics within Coronal Seismology

In solar physics, as in the rest of astrophysical research, the data are fixed and we cannot ask for a repetition of the physical process of interest to Nature. It is for that reason that any information as provided by oscillations, and thus by coronal seismology, is specially important. The method of seismological studies consists of three main steps: predict wave properties from a considered model as a function of its parameters, confront these predictions with the observed properties and extract from that comparison physical parameters. The last step normally represents a challenge, since the solution to the inverse problem might not exist or be unique due to measurement uncertainties.

The refinement of numerical techniques for doing predictions, more complex theoretical models, and improvements of inversion methods have permitted to extract very useful information about the corona, but the necessity of more efficient and better routines for obtaining indirect measurements of coronal features has to be still covered. Limitations related to mathematically ill-posed problems in the inference of parameters from observables and uncertainties from wave properties measurements must disappear. Due to the presence of uncertainties, new routines must be able to compare theoretical model predictions with observed data in a probabilistic way, so as to express the degree of certainty of predictions. But even when routines are capable of solving the problem, results depend on the underlying theoretical model that has been assumed. This makes model comparison the next necessary task to be performed for the new routines, in order to evaluate the plausibility of these models in explaining data.

In this context, the adoption of Bayesian techniques in coronal seismology has supposed a breakthrough. The Bayesian techniques permit to compare model predictions and observations by combining them with prior information and including the uncertainties. The results in form of probability density functions or posterior distributions, provide the probability of any statement i.e., hypothesis or parameters, permitting us then to infer those indirect measurements of interest and compute the model plausibilities to compare between different alternatives.

The success of the Bayesian approach can already be glimpsed in some coronal studies. Arregui & Asensio Ramos (2011) inferred the parameters associated to resonant absorption of coronal loop transverse oscillations i.e. the Alfvén travel time, the density contrast, and the transverse inhomogeneity length scale. In contrast with previous numerical and analytic studies by Arregui et al. (2007) and Goossens et al. (2008), not all models are equally probable with the plausibility for parameter values given by probability distributions. In a similar study by Arregui et al. (2013a), the authors performed the analysis of the density scale height and the magnetic field expansion in coronal loops by using models for period ratios of the fundamental mode period over that of the first overtone in transverse waves (Safari et al. 2007; Verth & Erdélyi 2008; Andries et al. 2005). Once the problem of inferring parameters given each model is solved, Arregui et al. (2013a) also asked the question of which model (uniform, density stratified, or expanded coronal loop) offers a more plausible explanation to data by further using Bayesian techniques. Motivated by the study that Soler et al. (2015) performed about changes of period ratios of the longitudinal modes with density profile along prominence threads, Arregui et al. (2015) considered alternative density profiles in coronal wave-guides in order to determine which was the most plausible profile, by continuing with Bayesian model comparison methods. In the same paper by Arregui et al. (2015), differences in resonant absorption depending on the assumed cross-field density variation were analysed by performing inference, model comparison and model averaging. Using analytical expressions by Pascoe et al. (2013) for Gaussian and exponential damping regimes, Arregui et al. (2013b) shows how to infer the density contrast and the transverse inhomogeneity length scale. The Bayesian study performed by Asensio Ramos & Arregui (2013) implemented a hierarchical model by considering a large number of events to define prior information for inferring parameters of resonant absorption mechanism. Finally, recent studies by Pascoe et al. (2017a,b) use a general damping profile for transverse coronal loops oscillations and Bayesian techniques to derive the cross-field density structure of resonant absorption mechanism and the role of different density profiles in EUV intensity. A recent review on these first applications of Bayesian analysis to coronal seismology can be found in Arregui (2018).

This thesis pretends to extend the Bayesian reasoning to the solar coronal field, especially to solve problems within coronal seismology but also as a starting point for applying them to more complex analyses such as the inversion of differential emission measurements, the computation of plausibilities for coronal heating models, etc.

1.4 Objectives and Outline

The aim of this thesis is to develop and apply Bayesian methods as a new way for obtaining information of the solar corona, comparing observations and theory. In particular, we have centred our attention in the analysis of coronal loops and prominences in the context of coronal seismology. The outline of this thesis is as follows:

The principles of Bayesian methods developed and used in this thesis will be explained in Chapter 2, together with a description of their advantages in front of previous methodologies.

In Chapter 3, we will approach in first instance the damping of standing transverse oscillations observed in coronal loops. We will first infer some physical parameters of these solar structures. Then, we will select three possible damping mechanisms to distinguish what is the most plausible one in explaining the observations. Regarding propagating waves in coronal loops, Gaussian and exponential damping profiles will be studied at the end of the chapter.

Next, we will focus on prominence threads in Chapter 4. We will apply the Bayesian techniques to standing transverse oscillations observed in these structures. Totally filled and partially filled tubes models will be considered to obtain physical properties of threads. We will further compare between the plausible damping mechanism of transverse oscillations in threads. In addition, the relation between the fundamental kink mode and its first overtone periods will be analysed for short and long thread approximations. Gaussian and exponential damping profiles of propagating waves will be studied at the end of the chapter.

Finally, future prospects will be treated in Chapter 5.

2

Bayesian techniques

'Totally mad,' he said, 'utter nonsense.
But we'll do it because it's brilliant nonsense.'
Douglas Adams (1980)

Statistics come from the human necessity to describe daily convictions, to quantify uncertainty to a question posed. Based on my experience, I am secure that my sister's name is Cristina (probability equal to 1), I do not know when it will rain next century in Madrid (probability equal to 0) and I will probably visit Paris one day (probability equal to 0.7). But our convictions of the real world change continuously with new experiences or events. If someone says to me that Paris is not interesting at all, then I would probably doubt about visiting Paris (probability equal to 0.4). Probabilities are beliefs, they are in the mind, not physically in the world.

Within statistics, *Bayesian probability theory* also called *probability theory as Logic*, permits translating convictions to the mathematical context in a natural way by including all our previous and current information, as well as uncertainties. Bayesian reasoning goes back to the essay by Bayes & Price (1763) and was given its current mathematical basis by Laplace (1774), but for two centuries, Bayesian statistic remained in the shadows. Fortunately, in 1931 the Bayesian thinking re-emerged thanks to the first edition of *Scientific Inference* work (Jeffreys & Jeffreys 1973) by Sir Harold Jeffreys. Since then, Bayesian probability theory has been applied to diverse problems such as decoding the enigma code in the second World War, filtering spam email (Rusland et al. 2017) or to a great variety of physical sciences (von Toussaint 2011), cosmology (Trotta 2008), exoplanet research (Gregory 2005), etc.

The Bayesian approach is based on the *Bayes' theorem* also called *Bayes' rule*, that can be simply expressed as

$$p(A|B) = \frac{p(A)p(B|A)}{p(B)}. \tag{2.1}$$

The Bayes' rule results by applying the sum and product rules of probability theory (see e.g. MacKay 2003; Gelman et al. 2013) and permits to obtain the conditional probability of any proposition, A, given any other proposition B. Normally, A represents parameters or models and B the available data and extra information in a scientific context, so that we can infer the probability of different parameter values or hypotheses based on our current state of information. Determining that conditional probability $P(A|B)$ is the ultimate goal of Bayesian statisticians.

The Bayesian approach is useful to compare between competing models or to solve the inverse problem (Fig. 2.1) of obtaining non-observable physical magnitudes from observed data, which is the common scenario given in scientific researches. But advantages of Bayesian statistics go far away. Apart from providing a simple way for answering scientific questions, the Bayesian approach permits to answer them incorporating all available prior information, uncertainties (not only in data but also in models), and removing nuisance parameters in a consistent manner that will be explained in the next sections.

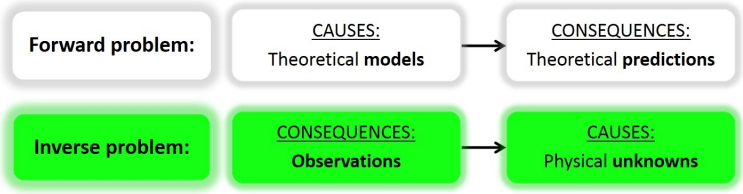

Figure 2.1: Forward and inverse procedures to solve physical problems.

But despite its numerous advantages, some controversy can be found in the literature when comparing Bayesian with frequentist statistics. In an attempt for choosing the best approach in describing the real world, frequentists accuse Bayesians of applying subjective principles through the inclusion of prior information which depends on the particular point of view of researchers. On the other hand, Bayesians accuse frequentists of avoiding relevant and available information into their analyses thus obtaining meaningless results. The reality is

that both Bayesian and frequentist statistic approaches assume certain subjective premises. However, subjectivity is unavoidable in any human activity, so to accept it as part of the scientific communication is the first step to advance and update our convictions (probabilities). In fact, the frequentist approach results by considering a special case of the Bayesian one when data is so numerous that prior information can be neglected. Hence, both can be useful for doing analysis depending on our aim; see Table 2.1 with some differences between both approaches. For more information about discussion between both thought currents and differences see e.g. Gregory (2005); VanderPlas (2014); Gelman & Hennig (2015).

	Frequentist	Bayesian
Probability	long-run frequency (probability of data, parameters fixed)	statement conviction (probability of parameter values, data fixed)
Input	large data set	any data, prior information, nuisance parameters, uncertainty
Results	model rejection confidence intervals	model plausibility credible intervals
Useful for	characterising data	inference, model comparison, prediction

Table 2.1: Comparison between frequentist and Bayesian approaches.

Bayesian probability of theory is the methodology selected to study the solar corona in this thesis, so that we dedicate an entire chapter to explain the fundamental Bayesian concepts. Starting with that point, we will first describe the main equations associated to Bayesian principles to infer parameters (Section 2.1), to compare between models (Section 2.2), to average models (Section 2.3), and to do predictions (Section 2.4). Then, we will discuss in Section 2.5 how to choose prior distributions and likelihood function focusing on those used in this thesis. Finally, the computation of integrals by direct numerical integration and Markov Chain Monte Carlo methods will be explained in section 2.6.

2.1 Parameter Inference

When the problem to solve is the inference of model parameters, a new notation is commonly introduced in Eq. (2.1). Hence, in the Bayesian framework the inference of a parameter set, $\boldsymbol{\theta}$, that characterises a model, M, conditional on

observed data, d, is performed by making use of the Bayes' theorem in the form

$$p(\boldsymbol{\theta}|M,d) = \frac{p(\boldsymbol{\theta}|M)p(d|M,\boldsymbol{\theta})}{p(d|M)}. \tag{2.2}$$

Bayes' theorem contains the following terms:

- Posterior, $p(\boldsymbol{\theta}|M,d)$. It is the posterior probability of parameter values, conditional on the assumed model and the observed data. The posterior distribution describes our updated state of knowledge about the values of the parameters.
- Prior, $p(\boldsymbol{\theta}|M)$. It is the prior probability of parameter values, before considering the data. By definition, it has to be specified before observations, otherwise the Bayesian analysis makes no sense.
- Likelihood function, $p(d|M,\boldsymbol{\theta})$. It is the probability of data given the model and parameters as certain. It relates theory with observations.
- Marginal likelihood, integrated likelihood or model evidence, $p(d|M)$. It represents the probability of the data given the model and independently of parameter values. It is the integral of the prior times the likelihood over the full parameter space,

  $$p(d|M) = \int_{\boldsymbol{\theta}} p(\boldsymbol{\theta}|M)p(d|M,\boldsymbol{\theta})d\boldsymbol{\theta}. \tag{2.3}$$

  Thus, the marginal likelihood is the normalisation factor in Bayes' rule and makes the posterior a proper probability distribution with unit area.

Instead of being interested on information about the global set of parameters, we are normally interested in isolating information of each parameter θ_i of selected model M. Obtaining that information comes easily from computing the marginal posterior as

$$p(\theta_i|M,d) = \int p(\boldsymbol{\theta}|M,d)d\theta_1...d\theta_{i-1}d\theta_{i+1}...d\theta_n, \tag{2.4}$$

which is an integral of the full posterior over the rest of the n model parameters. This integration process is called *marginalisation* and it is of special interest in Bayesian statistics because it permits to incorporate information from nuisance parameters, $\boldsymbol{\theta}^{\mathbf{nui}}$, but they can be excluded in our conclusions about physical magnitudes of interest. Examples of nuisance parameters are model parameters we are not interested on, unknown uncertainties, parameters included in

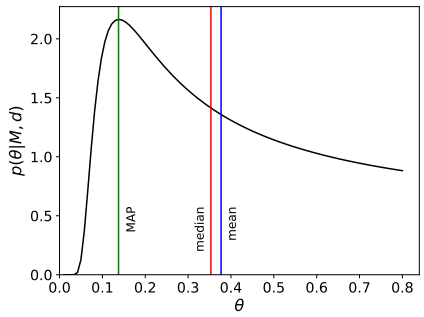

Figure 2.2: Statistics of an asymmetric posterior distribution. Values are: median=0.35, mean=0.38, and MAP=0.14.

the likelihood, etc. We include them as extra parameters in the $\boldsymbol{\theta}$ parameter vector to compute the global posterior and then we integrate it over all of those nuisance parameters.

In this thesis, parameters will be continuous variables, so that instead of providing single posterior numbers Bayes' rule will provide us entire distributions. Nonetheless, posterior distributions can be summarised by some statistics (point like or credible like) for communication purposes. The most used in Bayesian analysis are the *mean*, *median*, *Maximum A Posteriori (MAP)* estimate or parameter with maximum probability, and *credible interval* or *posterior bubble* which contains the most plausible parameter values. It is important to note here that credible intervals are not confidence intervals. Figure 2.2 shows differences between common statistics used to summarise information in Bayesian analysis. Normally, the median and the MAP values give us more useful information. For that reason, from now until the end of this thesis, we will use the median statistic to summarise distributions.

2.2 Model Comparison

The Bayesian framework also offers a straightforward method to compare the relative goodness of alternative models in explaining the observed data. Application of Bayes theorem to N alternative models (*hypothesis space*) leads to

$$p(M_k|d) = \frac{p(M_k)p(d|M_k)}{p(d)} \text{ for } k = 1, 2, ..., N; \tag{2.5}$$

where the N competing models may have a different number of continuous parameters.

If we then divide in pairs, the resulting posterior ratio or posterior odd, gives us a direct measure of the relative plausibility between two models M_k and M_j as

$$\frac{p(M_k|d)}{p(M_j|d)} = \frac{p(d|M_k)}{p(d|M_j)} \frac{p(M_k)}{p(M_j)} \; ; \; k \neq j. \tag{2.6}$$

This posterior odd has a first contribution coming from information of data or likelihoods and another contribution due to priors of models or prior odd. Normally, the prior odd is equal to 1 because we do not have any a priori reason to prefer one model over another before considering the data, $p(M_k) = p(M_j)$, so that we can define

$$BF_{kj} = \frac{p(d|M_k)}{p(d|M_j)} \; ; \; k \neq j. \tag{2.7}$$

This expression is called *Bayes factor* (see Kass & Raftery 1995) which equals the ratio of the two marginal likelihoods in Eq. (2.6). Hence, the Bayes factor numbers are descriptive statements of the evidence provided by the data in favour of one theory (k), as opposed to another (j).

Once the Bayes factors are computed, it is useful to consider twice the natural logarithm of these factors, $2 \ln BF_{jk}$, and to assess the level of evidence for one model against the alternative by following a criteria for classification. Thus, $2 \ln BF_{jk}$ may be viewed as a predictive score, with the criteria of classification fixed by each researcher. In our case, we have selected the evidence criteria developed by Kass & Raftery (1995), see Table 2.2. Following this criteria, one model is more plausible than another when the probability of data given the former model is almost three times the probability of data given the latter model.

$2 \ln BF_{kj}$	Evidence
0 - 2	Not Worth more than a bare Mention (NWM)
2 - 6	Positive Evidence (PE)
6 - 10	Strong Evidence (SE)
> 10	Very Strong Evidence (VSE)

Table 2.2: Kass & Raftery (1995) evidence classification.

2.3 Model Averaging

Sometimes, we have different models that depend on the same parameters and we are interested in inferring them. When in a model selection we try to determine which model explains better the data to infer next those parameters, we can find the evidence is not large enough in favour of any of them, so what model should we choose in the inference process? In those cases, the Bayesian approach allows us to infer the parameters by model averaging. Apart from adding information on prior density distribution and likelihood function, model averaging permits to include the uncertainty of models, i.e. the evidences of models in explaining observations. Instead of selecting only one model, we infer the marginal posterior distributions from an average of all of them. Hence, the marginal posterior of one parameter can be computed as

$$p(\theta_{\mathrm{i}}|d) = \sum_{k=0}^{M} p(\theta_{\mathrm{i}}|d, M_{\mathrm{k}}) p(M_{\mathrm{k}}|d), \tag{2.8}$$

where M is the number of models depending on θ_i. The model-averaged posterior in Eq. (2.8) is the average of the marginal posteriors computed by considering each model separately and weighted by the corresponding marginal likelihood. A clear view of the role of evidences here comes from considering one of the models as reference (in this case M_0) and expressing the previous equation as a function of Bayes factors in the following way:

$$p(\theta_i|d) = p(M_0|d) \sum_{k=0}^{M} p(\theta_i|d, M_k) BF_{k0}, \tag{2.9}$$

where BF_{k0} are the Bayes factors with respect to the reference model. In addition, the marginal likelihood of the reference model, $p(M_0|d)$ can be also computed using Bayes factors by considering that the sum of the M marginal likelihoods must be equal to 1:

$$p(M_0|d) = \frac{1}{1 + \sum_{k=1}^{M} B_{k0}}. \tag{2.10}$$

Although we will not use model averaging in this thesis, it is worthwhile mentioning it[1].

[1] We refer the reader to (Arregui et al. 2015) for an example of model averaging application.

2.4 Predictive Distributions

Finally, Bayesian statistics not only permits to extract information of parameters and models, but also about *future* data. Given a set of data, d, we can obtain the prior of hypothetical new data, $\tilde{d}$, also called *prior predictive distribution* which is described by

$$p(\tilde{d}|M) = \int_{\boldsymbol{\theta}} p(\tilde{d}, \boldsymbol{\theta}|M) d\boldsymbol{\theta} = \int_{\boldsymbol{\theta}} p(\boldsymbol{\theta}|M) p(\tilde{d}|M, \boldsymbol{\theta}) d\boldsymbol{\theta}, \tag{2.11}$$

The prior predictive distribution is the expected value of the likelihood of new data with respect to the old prior distribution. Similarly, we can obtain the *posterior predictive distribution* as

$$p(\tilde{d}|M, d) = \int_{\boldsymbol{\theta}} p(\tilde{d}, \boldsymbol{\theta}|M, d) d\boldsymbol{\theta} = \int_{\boldsymbol{\theta}} p(\boldsymbol{\theta}|M, d) p(\tilde{d}|M, \boldsymbol{\theta}) d\boldsymbol{\theta}. \tag{2.12}$$

when d and $\tilde{d}$ are independent. In this case, the posterior predictive distribution is the expected value of the likelihood but weighted with the posterior distribution of model parameters given old data. Note that the model M must be the same for both the old and the new data.

This procedure not only allows us to do predictions about new data $\tilde{d}$ given the model, but also permits to perform model checking by comparing those predictions with more real observations or by simulating from the model those new data, so as to check if the model really explains well our observations and where it can fail.

We will not apply predictive distributions to the main studies of this thesis. However, we will provide examples of its application in Chapter 5 as part of future guidelines within coronal seismology.

2.5 Definition of Prior Distributions and Likelihood Function

In the previous section, we have seen that Bayesian analysis depends on two main components: prior distributions and likelihood functions. They contain all the information we need to properly define our Bayesian statistical model. For this reason, it is of special importance to define priors and likelihoods adjusting to that knowledge as much as it is possible, whatever our proposition or unknown is. In this section, we will explain some of the most used priors focusing on those we have used in this thesis. Then, we will centre our attention in the likelihood function.

2.5.1 Prior

To start defining priors, we must consider a certain model and focus on what prior is adequate to describe information about its parameters. In particular, if we take a model with more than one parameter i.e. with a multidimensional *parameter space*, $\boldsymbol{\theta} = \{\theta_1, \theta_2, ..., \theta_n\}$, we will consider that all those parameters are independent, so that the global prior distribution is given by the product of individual priors defined for each parameter θ_i,

$$p(\boldsymbol{\theta}|M) = \prod_{i=1}^{n} p(\theta_i|M). \tag{2.13}$$

This assumption of independent parameters could be not realistic in some cases, but it is considered for simplicity as a useful starting point.

Concerning those individual priors, they can be divided into informative priors or non-informative priors. The former can be used to include valuable information of the particular parameter of interest. They can be normally accomplished by choosing conjugate priors, i.e. distributions of the same family than the likelihood such as Gaussian distributions, or by choosing empirical ones. The use of general expressions can introduce untreatable integrals during marginalisation. Regarding non-informative priors, they are introduced when our information about possible parameter values is poor. Flat or improper priors are the usual selection, though we must be aware of their limitations and possible alternatives.

Improper Prior

To represent an absolute lack of knowledge about parameters, sometimes improper priors are selected. Improper priors are characterised by considering no limits or infinite ones in ranges of plausible parameter values, which it could be seen as an advantage. However, we should not forget that the definition of posterior distribution includes an integral at the denominator in Eq. (2.2). If that integral is computable and finite under those infinite limits, then the so-called *posterior property* is satisfied and the use of our selected improper prior is not a problem. On the other hand, if this posterior property is not satisfied, we should be aware that we are extracting erroneous conclusions from a non-existing posterior distribution (see Tak et al. 2018, for completeness and more details). To ensure that the posterior property is satisfied, we must compute the integral before calculating posteriors. But this can result in an impossible task, so the simplest solution is to apply proper priors within defined limits.

Then, we have to find how to express our lack of knowledge about the parameter. In this case, solutions of the form of non-informative or vague priors can be used with very distant limits or with large variance and high tails.

None of the prior distributions proposed in this thesis will be improper, avoiding the posterior property problem.

Uniform Prior

The uniform or flat prior is a non-informative prior commonly selected when each parameter lies on a given plausible range with all values being equally probable. It is defined as

$$p(\theta_i|M) = \frac{1}{\theta_i^{\max} - \theta_i^{\min}};\ \theta_i \in (\theta_i^{\min}, \theta_i^{\max}) \tag{2.14}$$

and zero otherwise.

This type of non-informative prior works well for including vague information of location parameters which extend to a real range of values (negative and positive ones). However, it should be treated carefully with scale parameters i.e., parameters whose plausible range of values contains positive values, since for ranges large enough to contain some decades this flat prior is not completely non-informative. Suppose for example that one parameter takes values in the range $\theta_i \in [0.1, 100]$. Then,

$$\frac{\int_{10}^{100} p(\theta_i|M)d\theta_i}{\int_{0.1}^{10} p(\theta_i|M)d\theta_i} = 100.$$

Choosing a uniform prior implies that values in the first decade are 100 times less probable than those in the last decade of the selected interval. Hence, a uniform prior is not totally non-informative. This fact could be ignored, since its value does not affect importantly the posterior in the inference process because the prior is a constant value appearing in both numerator and denominator of Bayes' rule. However, this is not true for model comparison since Occam's razor varies strongly according to the prior and its range of application, as we will show at the end of this section.

One alternative choice to the uniform prior is the Jeffreys prior.

Jeffreys Prior

Jeffreys prior is a non-uniform prior which, equally to the uniform prior, is constant, but in the logarithmic scale. It is defined in the form:

$$p(\theta_i|M) = \frac{k}{\theta_i},$$

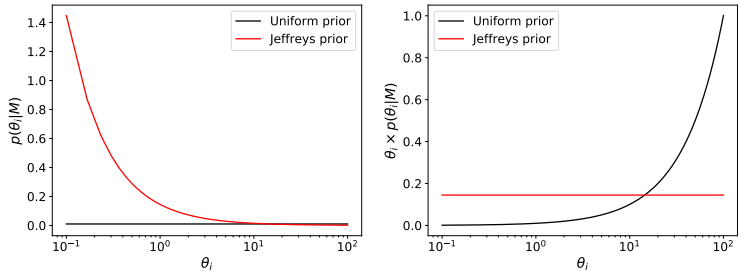

Figure 2.3: Left panel. Uniform and Jeffreys priors, p(θ_i|M). Right panel. Parameter times prior $\theta_i \times p(\theta_i|M)$.

where k is a normalisation constant derived from

$$\int_{\theta_i^{\min}}^{\theta_i^{\max}} p(\theta_i|M) = 1 \rightarrow k = \frac{1}{\ln\left(\frac{\theta_i^{\max}}{\theta_i^{\min}}\right)}.$$

Hence, the common final expression for the Jeffreys prior is

$$p(\theta_i|M) = \frac{1}{\theta_i \ln\left(\frac{\theta_i^{\max}}{\theta_i^{\min}}\right)}. \tag{2.15}$$

Figure 2.3 shows differences between the uniform and the Jeffreys priors given a parameter whose values are in between 0.1 and 100. The left panel shows how raw priors obtained with a Jeffreys prior give more plausibility to small parameter values. In the right panel, priors multiplied by the parameter are shown. We can appreciate changes in the global probability for large values of the parameter when a uniform prior is employed.

Gaussian Prior

Sometimes, we have related data from which priors can be constructed. Thus, contrary to previous non-informative priors, Gaussian prior permits us to include an available measurement of the particular parameter of interest, μ_{θ_i} with its corresponding uncertainty, σ_{θ_i} in the form

$$p(\theta_i|M) = \frac{1}{\sqrt{2\pi}\sigma_{\theta_i}} e^{-\frac{(\mu_{\theta_i} - \theta_i)^2}{2\sigma_{\theta_i}^2}}. \tag{2.16}$$

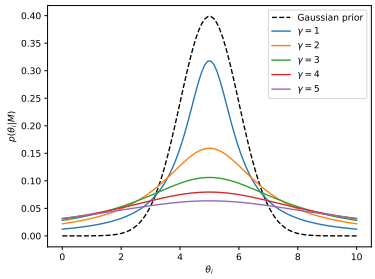

Figure 2.4: Gaussian and Cauchy prior distributions for different values of γ. A parameter measurement with $\mu_{\theta_i} = 5, \sigma_{\theta_i} = 1$ has been assumed.

The effect of this type of distribution in the inferred posterior distribution depends on the uncertainty; the larger the uncertainty is, the wider the posterior distribution is.

Cauchy Prior

The previous informative Gaussian prior restricts greatly the values of parameters because of probabilities tending to zero towards the tails. However, we are never so confident about that occurring for values in the tails. The Cauchy distribution, also called Lorentzian distribution, gives us the possibility of relaxing those probabilities with a special parameter, γ, which controls the height of the tails. The Cauchy prior distribution can be expressed as

$$p(\theta_i|M) = \frac{1}{\pi\gamma\left[1 + \left(\frac{\theta_i - \mu_{\theta_i}}{\gamma}\right)^2\right]}. \tag{2.17}$$

Figure 2.4 shows an example comparison between a Gaussian prior and multiple Cauchy distributions. We can appreciate that longer values of γ permit less constrained values of the parameter, with distributions formed by taller tails and less pronounced peaks.

Exponential Prior

Finally, we describe an exponential prior as

$$p(\theta_i|M) = ae^{-b\theta_i}, \tag{2.18}$$

with both a and b constants (a contains a normalisation constant).

In spite of emphasizing on those priors that we will use in the thesis, any distribution representing our knowledge about a parameter can be equally considered in our studies.

2.5.2 Likelihood Function

Regarding the likelihood function, the Gaussian profile is the most common choice when applying Bayesian methods since it represents Gaussian errors in data. We can consider data as the sum of a theoretical value of data and the uncertainty, $d = \Delta_{theor} + e$. In principle, this uncertainty e includes all type of uncertainties coming from the data and the model (itself or by independent variables).

Considering the simplest deterministic case in which the theoretical model does not contain any type of errors, the probability distribution of d is the same as the probability distribution of the uncertainty of the data, $e = d - \Delta_{theor}$. Hence, if the distribution of e is Gaussian, the likelihood function for a single data is expressed as

$$p(d|M,\boldsymbol{\theta}) = \frac{1}{\sqrt{2\pi}\sigma_d} e^{-\frac{(d-\Delta_{theor})^2}{2\sigma_d^2}}, \tag{2.19}$$

with σ_d its associated uncertainty. When instead of a single data, we have an entire dataset S, they are normally considered being independent, so that the total likelihood is a multivariate distribution resulting from the product of individual probabilities, i.e.

$$p(D|M,\boldsymbol{\theta}) = \prod_{s=1}^{S} \frac{1}{\sqrt{2\pi}\sigma_{d,s}} e^{-\frac{(d_s-\Delta_{theor})^2}{2\sigma_{d,s}^2}}, \tag{2.20}$$

with $\sigma_{d,s}$ the uncertainty associated to each single data.

Although we will limit our study to deterministic models, it is remarkable that for probabilistic models with uncertainties in the theoretical model, the likelihood is normally Gaussian with σ_{total} a combination of σ from each Gaussian contribution (Gregory 2005).

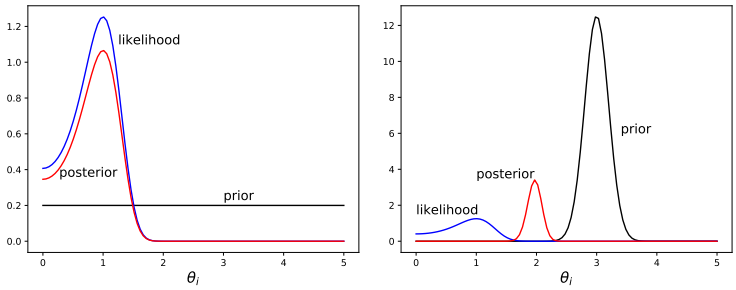

Figure 2.5: Comparison of posterior distributions obtained by considering a uniform prior (*left*) and a Gaussian prior (*right*) for the same considered likelihood.

Effect of Prior Distribution and Likelihood Function on Inference and Occam's Razor

Once the likelihood function is defined, we can analyse the effect of different priors in posterior distributions. Figure 2.5 shows two examples of posterior distributions for one model parameter, together with the corresponding prior distribution and likelihood function. At the left panel, a uniform prior has been assumed. Clearly, the posterior profile is almost equal to the likelihood function because information of data is very constrained and the prior is not. The opposite situation is also true. If the prior is very informative but the data are not, the major contribution to the posterior comes from the prior. The right panel shows the posterior resulting from considering the same likelihood that for the left panel but with a Gaussian prior. In this case, the influence of the prior is undoubtedly appreciated in the posterior which is now Gaussian like.

In order to see how priors and likelihoods affect model selection, let us assume a model, M, with a single parameter and a flat prior. By definition of density distribution, the posterior integral is

$$\int_{\Delta\theta} p(\theta|d, M)d\theta = p(\theta|d, M)\Delta\theta = 1, \tag{2.21}$$

so that $p(\theta|d, M) = 1/\Delta\theta$. On the other hand, if we take a Gaussian likelihood with a characteristic width $\delta\theta$,

$$\int_{\Delta\theta} p(d|\theta, M)d\theta = p(d|\hat{\theta}, M) \times \delta\theta = 1. \tag{2.22}$$

$\hat{\theta}$ represents the parameter value where the likelihood is maximum. Then, we can approximate the marginal likelihood as

$$p(d|M) = \int p(\theta|M)p(d|\theta, M)d\theta \approx p(d|\hat{\theta}, M)\frac{\delta\theta}{\Delta\theta}. \tag{2.23}$$

If we now compute the Bayes factor for two competing models, M_0 and M_1,

$$B_{10} \approx \frac{p(d|\hat{\theta}_1, M_1)}{p(d|\hat{\theta}_0, M_0)}\frac{\delta\theta_1}{\Delta\theta_1}\frac{\Delta\theta_0}{\delta\theta_0}. \tag{2.24}$$

Hence, we see that the Bayes factors depend on the uncertainty of the data, $\delta\theta$, but also on the width of the selected priors, $\Delta\theta$.

In general, the factor containing the widths for each model is called *Occam factor*, $\Omega_\theta = \delta\theta/\Delta\theta$ (even when the priors are not flat and likelihoods are not Gaussian). If a given model has a larger number of parameters or the ranges of the priors are wider, $\Delta\theta$ increases and the Occam's razor penalizes that model with a smaller evidence. The same happens if information about the data is so vague that the width of the distribution $\delta\theta$ is larger than the prior range. Thus, the choice of an appropriate prior and its boundaries requires some careful thought. Here is where Occam's razor acts within Bayesian statistics, by favouring simple models as more probable explanations to natural phenomena.

2.6 Integral Computation

One of the reasons why the Bayesian approach was not so popular until recent years was the impossibility of computing the complex integrals that arise when applying Eqs. (2.3) and (2.4). For low-dimensional parameter spaces, the use of simple direct numerical integration techniques is still feasible from the point of view of computational cost. Nevertheless, for high dimensional problems numerical integration strategies are required (Evans & Swartz 1995). Of special interest is the Markov Chain Monte Carlo (MCMC) sampling (Robert & Casella 2004; Sharma 2017). In this thesis, we will use both direct and MCMC approaches to give robustness to the obtained results and to test their goodness for future applications.

2.6.1 Direct Numerical Integration

In low-dimensional problems, sometimes an analytical approach is enough to solve integrals in our Bayesian study, but very often this situation is not possible. It is necessary to appeal to simple numerical or quadrature integration.

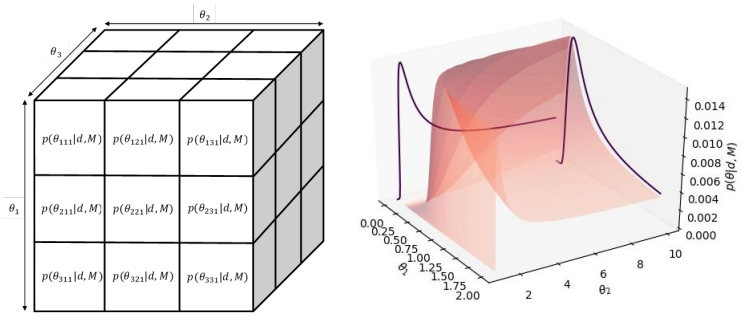

Figure 2.6: Left panel. 3D-array containing posterior values. Right panel. 3D-global posterior distribution and marginal posterior integrations resulting by integrating over each axis.

In our case, we have resorted to Simpson's or Kepler's rule to integrate. This rule consists on approximating the integrand to a parabola which goes through the same maximum, minimum and midpoint that the original function for each integration interval. The main advantage of this method is that the integral comes directly out to the evaluation of the original integrand on those three points. Furthermore, `Python` programming language permits us solving integrals of multi-dimensional arrays with this method [2].

To proceed, we first create our global posterior array with n times p dimensions; n is the number of model parameters and p is the number of selected points in each range of those parameters, see left panel of Fig. 2.6. Then, we integrate in each direction using `Python` to obtain the marginal posterior distributions, see right panel of Fig. 2.6.

The same procedure is applied to the computation of the marginal likelihood. The marginal likelihood can be obtained by using the multinomial likelihood or by calculating the probability of each observation with a simple likelihood to describe a distribution point by point.

In Appendix A.1, we show an example of all of Bayesian inference computations and `Python` programmes used with the numerical integration techniques explained here.

[2] Using the command *simps* from *scipy.integrate* package `https://docs.scipy.org/doc/scipy/reference/generated/scipy.integrate.simps.html`

2.6.2 Markov Chain Monte Carlo Method

Markov Chain Monte Carlo (MCMC) methods were introduced in the early 1950s during World War II (Robert & Casella 2011), although until the 1990s they were not used in statistics. This latter fact indeed provoked Bayesian analysis importance to increase to its current popularity. The basics of Monte Carlo integration consists of solving integrals by computing them as expected values:

$$\langle f(x) \rangle = \int p(x) f(x) dx = \frac{1}{n} \sum_{i=1}^{n} \alpha_i f(x_i), \tag{2.25}$$

where x_i are the more likely points under a weight function or probability distribution function (PDF), p(x). α_i is frequency or probability of each point.

Consequently, integrals are easily computable sampling $p(x)$, searching for α_i of each x_i. That is precisely what MCMC method is designed for. It samples $p(x)$ point by point in chains over x-space. Then, $f(x)$ is evaluated in those points and finally, the average is obtained.

MCMC algorithms can be more or less complex, but the majority of them have their origin on the oldest and most fundamental Metropolis-Hastings Sampler, whose algorithm can be summarised as follow:

+ Define a probability density function $p(x)$.
+ Define a *proposal density* $p(x_{i+1}|x_i)$.
+ Choose a starting point x_0
+ Repeat the following:
  - Given x_i, draw a new x_{i+1}.
  - Compute the *acceptance ratio* $a = \frac{p(x_{i+1})}{p(x_i)}$
  - If $a \geq 1$, accept the draw and add x_{i+1} to the chain.
    If $a < 1$, then draw a uniform random number $r \in [0, 1]$. Two possibilities exist in this case. If $r \leq a$, the new point x_{i+1} and is added to the chain. If not, x_i is added to the chain again.

The clear advantage of MCMC methods is the tremendous reduction of computational time and effort computing integrals, not only for one dimensional ones, but also for multidimensional integrals and multi-modal PDFs. MCMC is only valid for the long-term limit looking for stabilization of chains and this can be extremely long. The size of the proposal is also a difficulty, maybe the main one because if the proposal is too small or too large, the variable space will not

be entirely or well sampled loosing plausible peaks of probability. The election of the initialization point is crucial to reach the long-term limit efficiently, but that election is totally arbitrary depending on each researcher. Several techniques to avoid these problems and can be found in e.g Asensio Ramos & Arregui 2018; Gregory 2005, etc. Despite all these limitations, MCMC methods surely suppose a powerful tool, which is applicable to most of integration problems in science.

In this thesis, we use MCMC methods employing the *emcee* package of `Python` [3]. The *emcee* package is an implementation of the affine-invariant ensemble sampler proposed by Goodman & Weare (2010). Instead of going point by point, this sampler evolves K walkers, where the proposal distribution for each walker depends on the positions of the rest of the walkers in the complementary ensemble and then the process is repeated for each walker. The *emcee* sampler is an attempt to parallel that process by splitting the full ensemble into two. In addition, steps scale under affine-invariant transformations as the ensemble closes in on the posterior.

Marginal Posterior

In the inference problem, we are interested on obtaining marginal posteriors in Eq. (2.4). To this end, we can directly sample the global posterior and represent histograms of the samples in each direction of the parameter space. Remember that the number of repetitions of a given parameter in the sampling process is proportional to the sampled probability, in this case the posterior.

We must advice here that for simplicity, sampling codes are normally implemented only using the numerator of Bayes rule in logarithmic scale, since the denominator is a constant, thus the sampled parameter space does not change. However, this implies that MCMC methods can work even with improper priors. In this case, it is of special importance to verify that the posterior property is satisfied before sampling.

In order to see the applicability of both direct numerical integration and MCMC sampling method, we have included in Appendix A.2 MCMC computations to solve the polar rose example already solved in Appendix A.1.

Marginal Likelihood

The problem to solve is not trivial when we want to compute the marginal likelihood in Eq. (2.3). In this case, we must compute the expected value of

[3] Official documentation and examples of how emcee works and its limitations are in the following link: `http://dfm.io/emcee/current/`

the likelihood with respect to the prior:

$$p(d|M) = \langle p(d|M,\boldsymbol{\theta})\rangle = \int_{\boldsymbol{\theta}} p(\boldsymbol{\theta}|M)p(d|M,\boldsymbol{\theta})d\boldsymbol{\theta} = \frac{1}{n}\sum_{i=1}^{n}\alpha_i p(d|M,x_i) \quad (2.26)$$

To solve this, we have sampled the prior that is our weight function. Therefore, we obtain the more likely points of the space parameter for that prior, x_i and frequency α_i proportional to that prior (same notation that in Eq. (2.25)). Then, we evaluate the likelihood function in those points to finally compute its mean. In case we would be interested on knowing the probability of each data, this process should be repeated for each observation or data in order to obtain the entire marginal distribution.

Certainly, the difficulty of Bayesian analysis increases with dimensions, multi-modal distributions, hierarchical models, inclusion of uncertainties in the model, etc. However, Bayesian statistics have been recently implemented in coronal studies, so that simpler Bayesian studies are still required as a starting point to those more complicated scenarios. Hence, this thesis pretends to stablish the foundations of novel studies of the solar corona based on Bayesian statistics.

In next chapters, we will show how to apply all the Bayesian techniques explained here to real coronal problems.

3

Bayesian seismology of coronal loops*

It always seems impossible
until it's done.
Nelson Mandela

DAMPED transverse oscillations in solar coronal loops have attracted the attention of the coronal seismology community since first observations of these events were reported by Aschwanden et al. (1999) from the Transition Region and Coronal Explorer (TRACE) data. Interpreted as standing fast magnetohydrodynamics (MHD) kink modes (see Fig. 3.1), periods in between 258 and 320 s, loop lengths from 90 to 160 Mm, and horizontal displacements of 2 to 5.6 Mm were measured. In addition, Nakariakov et al. (1999) were able to estimate a damping time of (870 ± 160) s for one of those first events, which let glimpse to the quick nature of damping phenomena in transverse coronal loop oscillations. Subsequent studies using TRACE data were then performed involving horizontal motions of the loops (see e.g. Schrijver et al. 2002; Aschwanden et al. 2002; Verwichte et al. 2004; De Moortel & Brady 2007) and vertical ones (Wang & Solanki 2004); but further using other solar telescopes data. Observations from the Solar TErrestrial RElations Observatory (STEREO), for example, permitted to obtain more accurate estimates for loop lengths considering the three-dimensional geometry of long loops (Verwichte et al. 2009). The

*This chapter is based on: Montes-Solís, M., Arregui, I.: 2017, Comparison of damping mechanisms for transverse waves in solar coronal loops, The Astrophysical Journal, **846**, 89 (12pp) (Montes-Solís & Arregui 2017); and Arregui, I., Montes-Solís, M., Asensio Ramos, A.: 2018, Inference of magnetic field strength and density from damped transverse waves in solar coronal wave-guides, Astronomy & Astrophysics, submitted

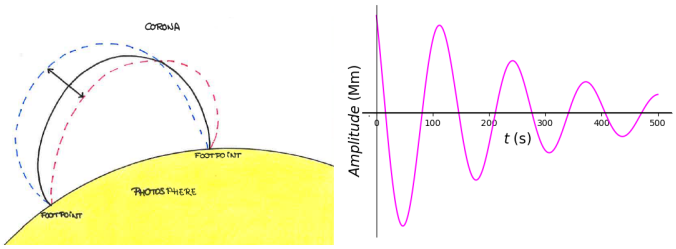

Figure 3.1: Sketch of a standing kink oscillating coronal loop (left) and an example of the ideal temporal variation of the amplitude for a damped oscillation (right).

Coronal Multi-channel Polarimeter (CoMP) was useful in detecting ubiquitous small amplitude ($\lesssim 1$ km s^{-1}) propagating fast waves in addition to the standing ones (Tomczyk et al. 2007; Tomczyk & McIntosh 2009), and current solar instruments on board the Solar Dynamics Observatory (SDO) are permitting to measure diverse transverse oscillations in coronal loops with unprecedented temporal and spatial resolution (see e.g. White & Verwichte 2012b; Verwichte et al. 2013; Nisticò et al. 2013; Goddard et al. 2016). These advances have allowed to extend first estimations of periods to values in between 100 s and 3 h, loop lengths above 70 Mm, horizontal displacements from 1 to 30 Mm, and damping times of a few periods.

Surely, the acquisition of fundamental features of magnetic fields and plasma properties conforming coronal loops becomes accessible with those observations. Hence, continuous estimations of the magnetic field strength emerged from observations with TRACE data by e.g. Nakariakov & Ofman (2001); Aschwanden et al. (2002), and Verwichte et al. (2004), who assessed values in the range $B = 4 - 90$ G. Searching for more accuracy in the determination of magnetic field strengths, Van Doorsselaere et al. (2008b) used spectroscopic data by Hinode, in addition to images, to obtain information on the mass density of a coronal loop and thus acquired a magnetic field strength of (39 ± 8) G. The advantages of taking into account geometric characteristics of loops were clearly visible with measurements using STEREO data by Verwichte et al. (2009). With a measured loop length of $L = (340 \pm 15)$ Mm and a period of $P = (630 \pm 30)$ s, they obtained an accurate associated magnetic field strength with a value of $B = (11 \pm 2)$ G. Multiple numerical simulations under different configurations have further tried to reproduce observed transverse waves and to compute the magnetic field strength with more or less success (De Moortel & Pascoe 2009; Selwa et al. 2011; Pascoe & De Moortel 2014; Chen & Pe-

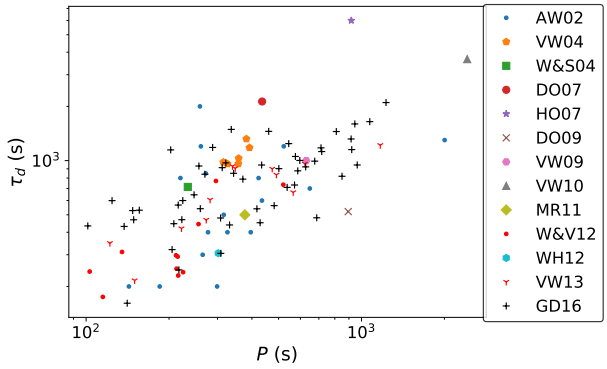

Figure 3.2: Scatter plot of damping times and periods obtained for some transverse coronal loop oscillations events reported in the literature. Data sources sorted in chronological order are: Aschwanden et al. (2002); Verwichte et al. (2004); Wang & Solanki (2004); Van Doorsselaere et al. (2007); Hori et al. (2007); Van Doorsselaere et al. (2009); Verwichte et al. (2009, 2010); Mrozek (2011); White & Verwichte (2012b); White et al. (2012); Verwichte et al. (2013); Goddard et al. (2016). The error bars are not included to not deface the plot.

ter 2015). In spite of all these and other analyses, efforts in computing more accurate values of the magnetic field strength continue nowadays.

The damping of transverse coronal loop oscillations plays also an important role in the determination of their physical quantities, since if the damping mechanism is known, it will represent an extra source of information about the physical conditions, specially of the cross-field distribution of the density (Arregui & Asensio Ramos 2014; Arregui et al. 2015). Although damping is not an omnipresent phenomenon (see e.g. Anfinogentov et al. 2013, 2015; Wang et al. 2012), it is commonly observed with damping times of only a few periods (see Fig. 3.2). Nonetheless, the difficulty in defining what a typical coronal loop is, since the physical parameters of observed loops cannot be directly measured, means that damping times from the first calculation by Nakariakov et al. (1999) were simple estimations, leading to the proposition of multiple damping mechanisms as plausible. For coronal loops, the discussion rapidly focused on mechanisms such as resonant absorption (Goossens et al. 2002; Ruderman & Roberts 2002a; Goossens et al. 2006), phase mixing of Alfvén waves (Heyvaerts & Priest 1983), lateral wave leakage (Spruit 1982; Cally 1986; Roberts 2000; Cally 2003) or foot-point leakage at the chromospheric density gradient (Berghmans & de Bruyne 1995; De Pontieu et al. 2001; Ofman 2002). Although

different methods exist to assess the plausibility between those and other alternative damping mechanisms (Roberts 2000; Ruderman 2005; Nakariakov & Verwichte 2005; Aschwanden 2005), the causative mechanism still remains largely unknown.

Apart from the aforementioned standing waves, the ubiquitous presence of propagating fast transverse waves was reported by Tomczyk et al. (2007) through the analysis of Doppler signals measured by CoMP. Neither intensity nor line-width variations were detected. Characteristics of the observed disturbances included amplitudes of less than 1 km s^{-1}, projected speeds of 1-4 Mm s^{-1}, and a period of about 5 min. Although first studies interpreted these oscillations as Alfvénic waves, Van Doorsselaere et al. (2008a) showed that they fit better with the fast magneto-acoustic interpretation. In a posterior study by Tomczyk & McIntosh (2009), measurements of the discrepancy between the inward and outward power of the waves, indicated for the first time in situ spatial wave damping of propagating disturbances. This was confirmed by Morton et al. (2014). As in the case of standing waves, the resonant absorption process was proposed as a plausible explanation to the observed damping, using analytical expressions for the damping length (Pascoe et al. 2010). That prediction was then analysed by Terradas et al. (2010) who found that if the statement is true, the damping is frequency selective with damping lengths inversely proportional to frequency. The good agreement between the observations and the predicted outward/inward power ratios strongly supported the idea that resonant absorption operates on these waves (Verth et al. 2010). Since then, different analytical and numerical studies have been performed focused on resonant absorption of propagating oscillations (Soler et al. 2011c,b; Goossens et al. 2012; Hood et al. 2013), concluding that standing and propagating waves seem not to differ with respect to the ability of this mechanism to explain observed damping scales. In the context of simulations and in view of those results, Pascoe et al. (2012, 2013) proposed that resonant absorption of propagating oscillations occurs with a Gaussian decay instead of the commonly used exponential profile at early times or a more general profile with a change between both profiles. Based on these studies, Arregui et al. (2013c) performed a Bayesian inversion to estimate the transverse density structuring of coronal loops. However, whether propagating waves damp having an exponential, a Gaussian, or a more general profile remains under intense discussion.

Motivated by all these studies, in this thesis we decided to apply Bayesian statistics to the study of standing and propagating transverse oscillations in coronal loops. We will first infer physical properties, such as magnetic field strength or densities in Section 3.1 using observations of standing oscillations. In Section 3.2, we will examine resonant absorption in the Alfvén continuum as

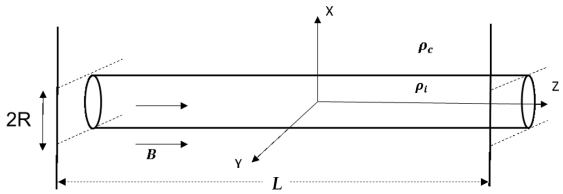

Figure 3.3: Sketch of the considered homogeneous flux tube representing a coronal loop.

damping mechanism inferring the parameters corresponding to the cross-field density structure of coronal loops. Then, we will consider this mechanism as an extra source of information in the inference of previous physical parameters. After that, we will infer parameters corresponding to two other plausible damping mechanisms, namely phase mixing in Section 3.3 and wave leakage in Section 3.4. In Section 3.5, the plausibility of the aforementioned mechanisms will be computed in order to clarify which one is responsible for the damping of transverse waves, if one exists. Moving to propagating oscillations, in Section 3.6, we will derive the parameters associated to resonant absorption in the Alfvén continuum when exponential and Gaussian decays are allowed to explain the damping tendency of this type of waves. Spatial scales in which exponential or Gaussian decays are more suitable in explaining the observed damping of propagating waves will be further obtained in the same section. Finally, a brief summary and the main conclusions of our study will be presented in Section 3.7.

3.1 Inference of Physical Parameters in Solar Coronal Loops

Our seismological study starts by considering a simple model for a coronal loop. In such a model, the coronal loop is represented by a homogeneous flux tube with internal density, ρ_i, embedded in a less dense coronal environment with density ρ_e (Fig. 3.3). Under the thin tube (TT) approximation, the phase speed (v_{ph}) of fast kink modes supported by coronal loops can then be approximated to the kink speed (c_k) expressed as

$$v_{ph} = c_k = v_{Ai}\left(\frac{2\zeta}{1+\zeta}\right)^{1/2}, \tag{3.1}$$

which depends on the internal Alfvén velocity, v_{Ai}, and the density contrast, $\zeta = \rho_i/\rho_e$ (Spruit 1982; Edwin & Roberts 1983).

Expanding the Alfvén speed as a function of the magnetic field strength, B, and internal density, the theoretical equation for the phase speed can be written in the following form

$$v_{ph} = \frac{B}{\sqrt{\mu\rho_i}} \left(\frac{2\zeta}{1+\zeta} \right)^{1/2}, \tag{3.2}$$

with the magnetic permeability μ considered equal to its free space value i.e., $\mu = \mu_0 = 4\pi \times 10^{-7}$ NA^{-2}.

Regarding the observations, Alfvén velocities, magnetic field strengths, and densities can not be directly measured, but can be estimated from the observed periods of the oscillations and the estimated lengths of the loops. For example, interpreting the first imaging observations of transverse coronal loop oscillations by Aschwanden et al. (1999) and Nakariakov et al. (1999) as kink modes, first estimations of phase speeds were derived by Nakariakov & Ofman (2001), leading to values of $v_{ph} = (1020 \pm 132)$ km s^{-1} and $v_{ph} = (1030 \pm 410)$ km s^{-1}, resulting from considering period and length measurements for two different events observed on 14th July, 1998 and 4th July, 1999 respectively. From those phase speed values and the theoretical expression in Eq. (3.1), the inference of the unknown parameters, $\boldsymbol{\theta} = \{\zeta, v_{Ai}\}$ can then be attempted through the combination of their different values. Using this technique, Nakariakov & Ofman (2001), obtained a value of the Alfvén speed $v_{Ai} = (756 \pm 100)$ km s^{-1}, after considering $\zeta = 10$ for the first event in 1998. The same is applicable to Eq. (3.2) with its associated unknown parameters, $\boldsymbol{\theta} = \{\zeta, \rho_i, B\}$, obtaining a magnetic field strength of $B = (13 \pm 9)$ G with $\zeta = 10$ and limiting the internal density to $n_e \in [10^{9.2\pm0.3}, 10^{9.3\pm0.3}]$ cm^{-3} ,estimated from the same observations. However, the main inconvenience of this procedure is that the density of a coronal loop is highly uncertain and difficult to estimate. Hence, repeating the process with some other values of ζ and ρ_i, the values of the internal Alfvén velocities and the magnetic field strengths will have a variability for the same observation; see Fig. 3.4.

Hence, as an example of how the density uncertainties can be included in the analysis, we perform the Bayesian inference of parameters for the second observation by Nakariakov & Ofman (2001) with phase speed $v_{ph} = (1030 \pm 410)$ km s^{-1}. Following the inference procedure explained in Chapter 2, we first investigate the Eq. (3.1) with uniform priors for the unknowns, $\boldsymbol{\theta} = \{\zeta, v_{Ai}\}$, over the plausible ranges $v_{Ai} \in [1, 2000]$ km s^{-1} and $\zeta \in [1.1, 10]$. The resulting marginal posterior distributions for both parameters are shown in Fig. 3.5. In Fig. 3.5a we find that the internal Alfvén speed can be properly inferred with a median value of $v_{Ai} = 829^{+343}_{-323}$ km s^{-1}. On the other hand, the density contrast

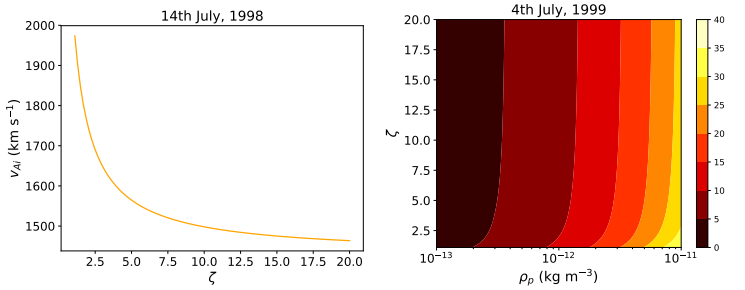

Figure 3.4: Left panel. Variability of the internal Alfvén velocity (v_{Ai}) for the event observed by TRACE on 14th July, 1998 with a phase speed $v_{ph} = (1020 \pm 132)$ km s^{-1} and applying Eq. (3.1) to a range of the density contrast (ζ). Right panel. Variability of the magnetic field strength (B) for different values of ζ and ρ_i for the event observed by TRACE on 4th July, 1999 with a phase speed $v_{ph} = (1030 \pm 410)$ km s^{-1}. Different colours indicate ranges of values of the magnetic field strength following the criteria in the colour bar.

(Fig. 3.5b) cannot be inferred with the information on the phase speed alone. Adopting now Eq.(3.2) with its corresponding unknowns, $\boldsymbol{\theta} = \{\zeta, \rho_i, B\}$, and repeating the inference process, leads to the marginal posterior distributions for the loop density and for the magnetic field strength in Figs. 3.5c,d respectively. In this case, uniform priors in the plausible ranges $B \in [0.01, 100]$ G and $\rho_i \in [10^{-13}, 10^{-11}]$ kg m^{-3} corresponding to particle densities in the range $n \sim [10^8 - 10^{10}]$ cm^{-3} (Priest 1982) are considered. Values for ζ remain the same and the marginal posterior for the density contrast is the same as the one shown in Fig. 3.5b. The results now show a well-constrained distribution for the magnetic field strength, that can therefore be properly inferred with a median value of $B = 22^{+11}_{-10}$ G. The same is not true for the loop density, for which no information can be gathered.

In summary, by adopting the simplest possible model for transverse loop oscillations under the TT approximation, measuring the phase speed of the waves, and considering uniform priors for the unknown parameters, the internal Alfvén speed and the magnetic field strength can be inferred, even if the densities inside and outside the wave-guide are largely unknown.

Nonetheless, in the results above, a large range of possible values for the wave-guide density was considered. To see how the density affects the inference of the magnetic field strength, we repeated its inversion by considering uniform priors over different ranges for both parameters, ρ_i and ζ. First, the maximum value of the density contrast was modified from $\zeta = 10$ up to $\zeta = 50$.

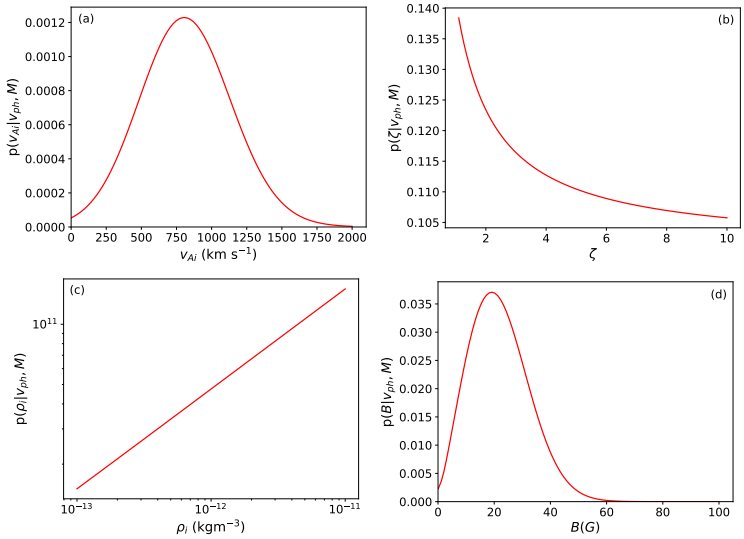

Figure 3.5: Marginal posteriors for the internal Alfvén speed (a), the density contrast (b), the internal density (c), and the magnetic field strength (d) for a transverse coronal loop oscillation with a phase speed value of $v_{ph} = 1030 \pm 410$ km s^{-1} (event of 4th July, 1999 by Nakariakov & Ofman (2001)). Uniform prior in ranges $v_{Ai} \in [1, 2000]$ km s^{-1}, $\zeta \in [1.1, 10]$, $\rho_i \in [10^{-13}, 10^{-11}]$ kg m^{-3}, and $B \in [0.1, 100]$ G have been considered. Median values of the inferred internal Alfvén speed and magnetic field strength are $v_{Ai} = 829^{+343}_{-323}$ km s^{-1} and $B = 22^{+11}_{-10}$ G respectively, with credible intervals of 68%.

Figure 3.6a shows the obtained results. We can see that the density contrast over which a uniform prior is considered does not introduce big changes in the inferred posterior for the magnetic field strength. A different result is obtained when the inversion is performed considering uniform prior distributions over different ranges for the internal density. Figure 3.6b shows marginal posterior distributions for the magnetic field strength computed by considering a uniform prior for the fixed range of $\zeta \in [1.1 - 10]$ and uniform priors over three different ranges for the wave-guide density. We can see that considering the lower density half-range with $\rho_i \in [10^{-13} - 10^{-12}]$ kg m^{-3} or the higher density half-range with $\rho_i \in [10^{-12} - 10^{-11}]$ kg m^{-3} produce rather different results. When the full range $\rho_i \in [10^{-13} - 10^{-11}]$ kg m^{-3} is taken, results similar to those obtained with the higher density half are found i.e., the contribution to

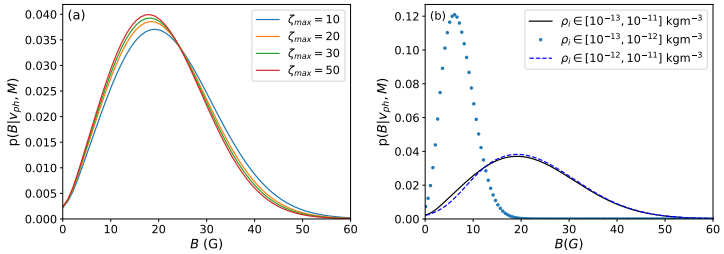

Figure 3.6: Marginal posteriors of the magnetic field strength by considering different values of $\zeta_{\max}$ (a) and ρ_i intervals (b), for the same event as Fig. 3.5. Median values remain almost the same than in the previous figure except for the dotted distribution in panel (b), whose median value is $B = (8 \pm 3)$ G.

the marginal posterior from the integral over the range $[10^{-13} - 10^{-12}]$ seems to be insignificant in comparison to the contribution from the integral over the range $[10^{-12} - 10^{-11}]$. We must mention here that when a parameter is left to vary over several decades, using a uniform prior is not the best choice (see Section 2 for more details). In this case, considering the density a scale parameter and using a Jeffreys prior (we refer the reader to Appendix B for a study that applies diverse uninformative priors to this problem).

Besides changing the range of variation over which uniform prior distributions are defined, the Bayesian formalism enables us to incorporate more informative priors about some properties of the emitting coronal plasma, such as the density from spectroscopy analyses. Let us assume we have an estimate for the loop density in the previously analysed event, with its corresponding uncertainty. We can use this information to construct a Gaussian prior for the density, by considering Eq. (2.16) for the unknown parameter $\theta_i = \rho_i$, centred on the spectroscopic estimate $\mu_{\theta_i} = \mu_{\rho_i}$, and with uncertainty $\sigma_{\theta_i} = \sigma_{\rho_i}$. Figure 3.7 shows the result of such an inversion for the magnetic field strength and the plasma density inside the wave-guide. Figure 3.7a shows the Gaussian prior for the density, for a given measured value of ρ_i with its uncertainty, and its corresponding posterior. The resulting posterior closely resembles the assumed prior, although the information on the data has slightly altered the posterior. Figure 3.7b shows a comparison between the marginal posterior distributions for the magnetic field strength using the uniform prior and the Gaussian prior in density. Using the information obtained from measuring the plasma density produces a shift in the marginal posterior for the magnetic field strength towards smaller values and a more constrained distribution. The last two panels

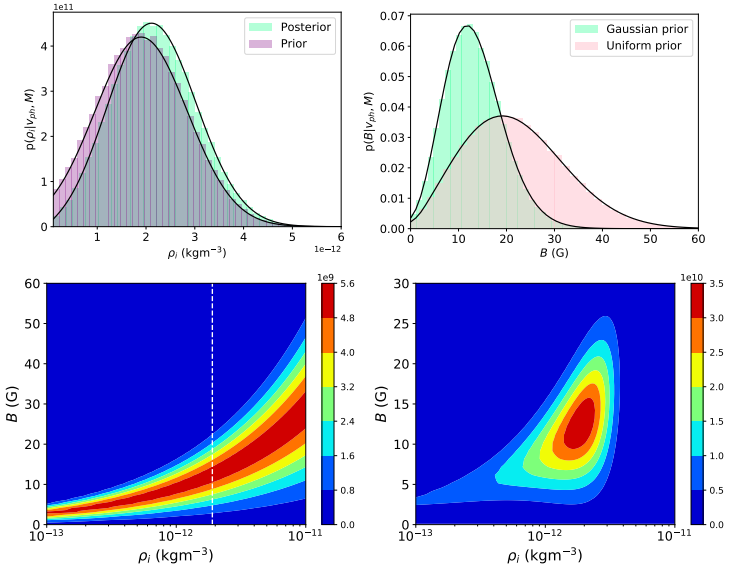

Figure 3.7: Upper panels. Gaussian prior with $\mu_{\rho_i} = 1.9\times10^{-12}$ kg m^{-3}, $\sigma_{\rho_i} = 0.5\mu_{\rho_i}$ and the associated posterior for ρ_i (left) and comparison between marginal posteriors for the magnetic field strength obtained for uniform and Gaussian priors (right). Observed event is the same as in previous cases. Posterior distributions obtained by considering a Gaussian prior take median values of $\rho_i = (2\pm1)\times10^{-12}$ kgm^{-3} and $B = (14\pm6)$ G. Coloured histograms in the same figures represent results integrating by MC methods. Bottom panels. Joint posteriors of B and ρ_i considering uniform (left) and Gaussian (right) priors in ρ_i. Colours indicate probability values following the bar criteria at the right of each plot.

show a comparison between the joint posteriors for the internal density and the magnetic field strength obtained by employing a uniform prior (Fig. 3.7c) and a Gaussian prior (Fig. 3.7d) for the internal density. As can be seen, the addition of information enables us to further constrain our estimates for both unknowns, wave-guide density and magnetic field strength.

However, by looking at Fig. 3.7c one may ask if, instead of using a Gaussian prior on density, it is not possible to consider a uniform prior over the full range of internal density values and then to perform a cut of the joint two-dimensional posterior at the plasma density value that has been measured (dashed line in Fig. 3.7c), or to simply insert the value of μ_{ρ_i} in ρ_i in Eq. (3.2) and solve the

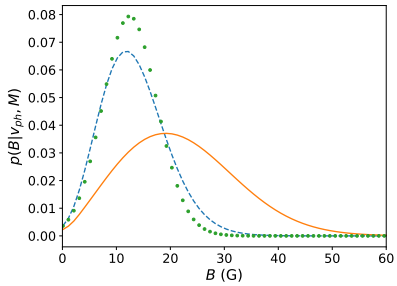

Figure 3.8: Comparison between marginal normalized posteriors of the magnetic field strength resulting by considering a uniform (blue dashed line) or a Gaussian (orange continuous line) prior for ρ_i, and by considering a cut off of the joint posterior (green dotted line) at the density value of $\rho_i = 1.9 \times 10^{-12}$ kg m^{-3}, equal to the mean of Gaussian prior. Median value of $B = (13 \pm 5)$ G is obtained for trimmed distribution.

modified inversion problem for two unknowns, $\boldsymbol{\theta} = \{\zeta, B\}$. Figure 3.8 shows a comparison between the result for the marginal posteriors for the options being discussed. The solid line is the result of the integration of the full posterior over the full range of values for ρ_i, which presents the most uncertain outcome with values for the magnetic field strength extending up to $\sim$ 60 G. The dotted-line shows the result of taking a cut of the joint posterior for B and ρ_i at the measured value for the plasma density. Although it is the most constrained distribution, it does not take into consideration the uncertainty on the measured plasma density. It just considers that this uncertainty is zero. Certainly, this is not the best option because it does not represent real measurements. Finally, the dashed curve is the posterior corresponding to the use of the Gaussian prior for the density. Hence, with this exercise we show that what one is willing to assume about the plasma density inside the wave-guide is capable of influencing the resulting inference of the magnetic field strength.

The event treated here represents only an example of the Bayesian inference application, but in reality all these techniques are not restricted to this case. They are applicable to any observed event for which periods and loop lengths are available. In Table B.1 of Appendix B, we have included medians obtained for the internal Alfvén speed and the magnetic field strength in other events when uniform and Gaussian priors are considered for the internal density. Also in Appendix B, some histograms and figures further summarise the results. As an example, Figure 3.9 contains the inferred median values of the magnetic field strength under the uniform prior assumption, as a function of the wave period. It displays the inversely proportional tendency of the magnetic field strength with the period. Apart from that, the majority of the observed events have periods in between 200 and 600 s with a large variability in the magnetic field strength value.

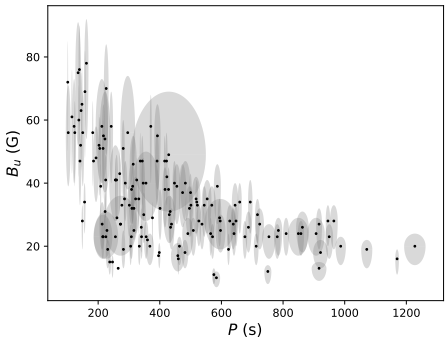

Figure 3.9: Median values of the inferred magnetic field strength under uniform prior assumption (B_u) as a function of the period of wave (P). Ovoids represent the area defined by the associated uncertainties of both magnitudes.

3.2 Resonant Absorption in the Alfvén Continuum

Due to the nature of Alfvén waves, they propagate along magnetic field lines. If the equilibrium parameters of the plasma where they exist vary continuously across the magnetic field, then the Alfvén speed and thus the Alfvén frequency may also vary continuously in that direction, conforming the so-called *Alfvén continuum*. In this context, a coronal loop modelled as a straight cylinder of zero-β plasma with length L and radius R, contains Alfvén waves when the loop is embedded in a uniform magnetic field in the longitudinal direction (see e.g. Edwin & Roberts 1983, for a review of oscillations in cylindrical geometry). In addition, coronal loops are denser than the solar corona, so that the density varies across the magnetic field in the radial direction from its internal to its external value i.e., it should have an Alfvén continuum in the transition between both media where $v_A(r) = B/\sqrt{\mu\rho(r)}$. Let us then consider that the transition occurs in a thin layer around the loop (Fig. 3.10) and that the coronal loop supports a kink oscillation, whose frequency will be in between the internal and the external Alfvén frequency values. Hollweg & Yang (1988) proposed that the energy exchange between the kink mode and the Alfvén oscillations in the thin boundary, could be the cause of the observed damping. This process of resonant absorption in the Alfvén continuum and resonances in general were amply studied (see e.g. Sakurai et al. 1991; Goossens et al. 1992, 1995). However, these studies were not supported by observations until Aschwanden et al. (1999) and Nakariakov et al. (1999) analysed TRACE data. Motivated by those observations, Ruderman & Roberts (2002b) focused their study specifically on resonant absorption in the Alfvén continuum generated

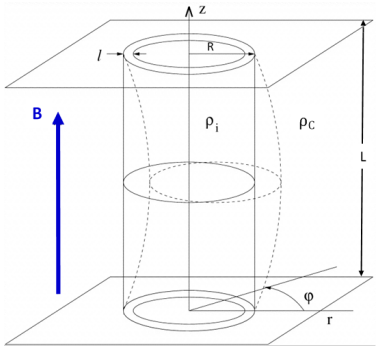

Figure 3.10: Sketch of the considered model for resonant absorption mechanism. *Adapted from Ruderman & Roberts (2002b).*

in solar coronal loops. For that purpose, they considered cylinders previously described, anchored to an ideal infinitely conducting plasma and they applied the thin tube ($R << L$) and thin boundary ($l << R$) approximations, in addition to the stationary state of the kink mode. With all those ingredients, they derived a simple analytical expression for the relation between the damping time and the period of kink modes, also denominated the damping ratio,

$$\frac{\tau_d}{P} = \frac{2}{\pi}\,\frac{R}{l}\frac{\zeta+1}{\zeta-1}. \tag{3.3}$$

In this expression, τ_d is the damping time, P the oscillation period, l the thickness of the non-uniform layer, and $\zeta = \rho_i/\rho_c$ the density contrast between the internal (ρ_i) and external (ρ_c) densities. The factor $2/\pi$ arises from considering a sinusoidal profile for the density variation in the radial direction at the non-uniform layer, $\rho(r)$, that in principle can be chosen freely [†]. Ruderman & Roberts (2002a) applied Eq. (3.3) to the observation by Nakariakov et al. (1999) in order to obtain information about how strongly inhomogeneous is the observed coronal loop. In particular, they estimated a thickness of the non-uniform layer equal to $l/R \approx 0.23$ upon assuming a density contrast of $\zeta = 10$.

Since then, multiple studies have been performed focusing on resonant absorption of transverse coronal loop oscillations. For example, Goossens et al. (2002) pointed out that not necessarily all loops should have the same value of l/R. Using the same Eq. (3.3), they computed the inhomogeneity scale for the

[†]The most commonly employed density variations are: linear with an associated factor in Eq. (3.3) of $4/\pi^2$, sinusoidal with a factor of $2/\pi$, and parabolic with $4\sqrt{2}/\pi^2$ (Arregui et al. 2015).

11 loop oscillations events compiled by Ofman & Aschwanden (2002), assuming a value of ζ for the density contrast. Although theoretical studies indicated that only resonant absorption in thin layers is appreciable in observations, Van Doorsselaere et al. (2004) and Arregui et al. (2005) extended the study to consider thick boundaries, finding small differences in comparison to analytical expressions. More recently, Arregui et al. (2015) compared the suitability of different density profiles in the resonance layer showing that differences are not considerable except for strong damping regimes with ratios smaller than unity, not corresponding to easily observable values. For more studies of this process see e.g. Aschwanden (2005); Nakariakov & Verwichte (2005); Aschwanden (2006); Ruderman & Erdélyi (2009), and references therein.

In this thesis, we analyse resonant absorption with a Bayesian analysis taking this damping mechanism as certain. Hence, we assume the model by Ruderman & Roberts (2002b) and use Eq. (3.3) to determine, in several cases, the posterior distributions for both parameters involved in the cross-field density inhomogeneity, $\boldsymbol{\theta} = \{\zeta, l/R\}$. For this purpose, we start by considering values of ζ and l/R within plausible ranges in coronal loops, $\zeta \in [1.1, 10]$ and $l/R \in [0.01, 2]$. Introducing directly these parameters in Eq. (3.3), the values for the damping ratio predicted by theory are in a wide range $\tau_d/P \sim (0.5 - 10^4)$, containing observed values and with larger damping ratios corresponding to the smallest parameter values (Fig. 3.11). It is important to note that not all coronal loops have necessarily the same radial density profiles, but we wanted to keep the analysis simple.

Once we have selected the plausible ranges, we apply Bayes' theorem in Eq. (2.2) with uniform priors and consider as observable the damping ratio, $d = \tau_d/P$. Figure 3.12 represents the result of the global posterior in 3D

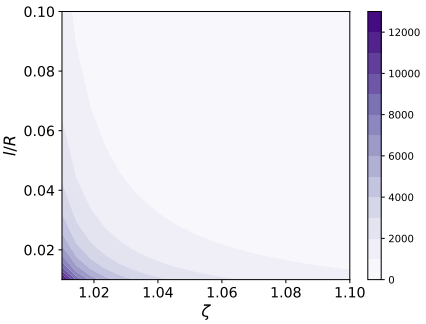

Figure 3.11: Values of the theoretical damping ratio as a function of the considered values of the density contrast (ζ) and the thickness of the inhomogeneous layer (l/R). Zoom in the smallest values of parameters region was done for clarity, with darker purple colours indicating larger values of the damping ratio, according to colour-bar.

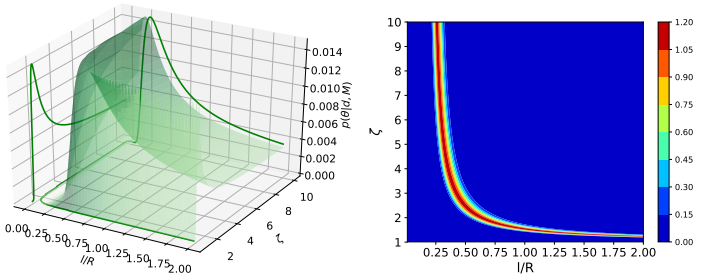

Figure 3.12: Left panel. 3D global posterior. Right panel. 2D map of posterior probabilities in the parameter space for resonant absorption model. Colours indicate the value of the posterior according to the bar. For both panels, an observable (τ_d/P) equal to 3 has been selected with an associated uncertainty of 50% (left) and 10% (right).

(left panel), and 2D (right panel) when we consider a damping ratio equal to, $\tau_d/P = 3 \pm 0.3$. In the 3D posterior, we can appreciate the region of the parameters space that is more probable in coronal loops under the assumed conditions. When we focus on the 2D figure that represents the projection of the posterior probability in the parameter space, we appreciate how uncertainties of both the density contrast and the inhomogeneity scale are related. Thus, larger values of l/R correspond to a smaller uncertainty in the determination of the density contrast value, as it was already indicated in the previous study of Arregui et al. (2007); see also Arregui & Asensio Ramos (2014).

Marginalising that joint posterior by using Eq. (2.4), the results for this damping mechanism look like in Fig. 3.13 with the preceding value for the damping ratio, but also for other plausible values and uncertainties. In principle, both the density contrast, ζ, and the transverse inhomogeneity length scale, l/R, can be properly inferred, despite the posteriors for the density contrast show long tails as was already noted by Arregui & Asensio Ramos (2014). The posterior densities peak at lower values for both unknowns, the larger the damping ratio is (Figs. 3.13a and 3.13c) and their distributions have broader shapes the larger the uncertainty in the observed damping ratio is (Figs. 3.13b and 3.13d). Applying these Bayesian techniques to the real event observed by Nakariakov et al. (1999) with $\tau_d/P = 3.4 \pm 0.7$, the mean values of the posterior distributions for both parameters are $\zeta = 4^{+4}_{-2}$ and $l/R = 0.4^{+0.5}_{-0.1}$.

Going now one step further, we realised that the period and phase speed in kink modes permit us to express the damping time in Eq. (3.3) in the alternative

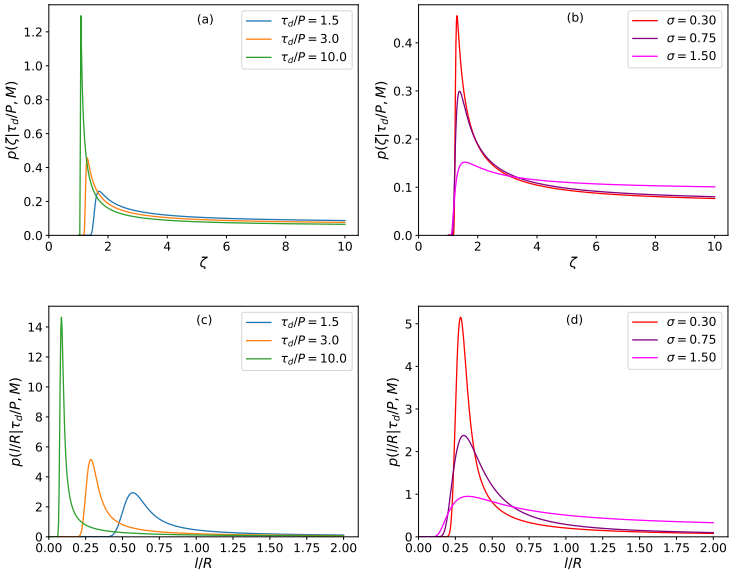

Figure 3.13: Marginal posterior distributions for resonant absorption parameters $(\zeta, l/R)$ under plausible conditions in solar coronal loops. Left panels. Results for different values of the damping ratio, τ_d/P, with an uncertainty of 10%. Right panels. Results for a fixed damping ratio, τ_d/P=3, and three values for its uncertainty.

form

$$\tau_d = \frac{2}{\pi}\frac{R}{l}\frac{\zeta+1}{\zeta-1}\frac{2L}{v_{ph}}, \tag{3.4}$$

with v_{ph} from Eq. (3.2). Thus, we can use resonant absorption as an extra source of information in the determination of the magnetic field strength of solar coronal loops. In this scenario, we have three observables, $d = \{v_{ph}, \tau_d, L\}$, considered as independent (see Chapter 2 for the description of the likelihood in this case) and four parameters, $\boldsymbol{\theta} = \{\rho_i, \zeta, B, l/R\}$ in two equations. We do the inference for the event observed by Nakariakov & Ofman (2001) on 4th July, 1999 analysed in the previous section. For that purpose, we take three synthetic damping times, $\tau_d = (500, 800, 1200 \pm 50)$ s, as plausible examples,

the observed length, $L = 190$ Mm with no uncertainty, and the measured phase speed, $v_{ph} = (1030 \pm 410)$ km s^{-1}. We use uniform priors over given ranges for all parameters, which remain the same as before.

Figure 3.14 displays the marginal posterior distributions and the joint probability distributions for the magnetic field strength, the density contrast, and the transverse density inhomogeneity length scale. The posterior for the magnetic field strength does not show appreciable differences in comparison to the inversion without the use of the damping time (Section 3.1), whatever the value of the damping ratio is (Figure 3.14, left panel at the bottom). The remaining panels in Fig. 3.14 show that the two parameters that define the cross-field variation of the density (ζ and l/R) can be constrained better or worse, depending on the actual value of the damping time (left panels) and relations between the posterior probabilities of the three parameters in the model (right panels). Comparing these results with those in Fig. 3.13, we see that, although the considered uncertainty is also of 10%, the posterior distributions associated to results without damping are better inferred since fewer parameters are involved in the analysis.

Hence, the parameters related to the density structuring in coronal loops can be inferred if resonant absorption is considered, but no critical information is added when this mechanism is used to infer the magnetic field strength.

3.3 Phase Mixing

In the previous section, we saw the importance of the Alfvén continuum in resonant absorption. Nonetheless, in a dissipative medium the Alfvén continuum further implies the creation of small-scale local perturbations with amplitudes increasing in time and with length-scales decreasing, so that Alfvén waves are mixed in the non-homogeneous layer of solar coronal loops. When, in addition, resonant absorption of a kink mode occurs, this process is enhanced around the resonance region by the extra energy injected by the kink mode. Hence, Alfvén waves interact more quickly mixing their phases and behaving as an oscillator weakly coupled by friction. Apart from the consequent dissipation of the energy, this phase mixing process produces an amplitude decay of the Alfvén waves similar to that produced by resonant absorption in kink modes. Phase mixing was first discussed by Heyvaerts & Priest (1983) as another plausible mechanism in explaining the heating of coronal structures, including a study of its effect on the damping process of transverse oscillations. In their model (Fig. 3.15), Heyvaerts & Priest (1983) considered an Alfvén continuum produced by changes in the magnetic field due to an inhomogeneity operating in the perpendicular direction to those lines in a planar geometry. By solv-

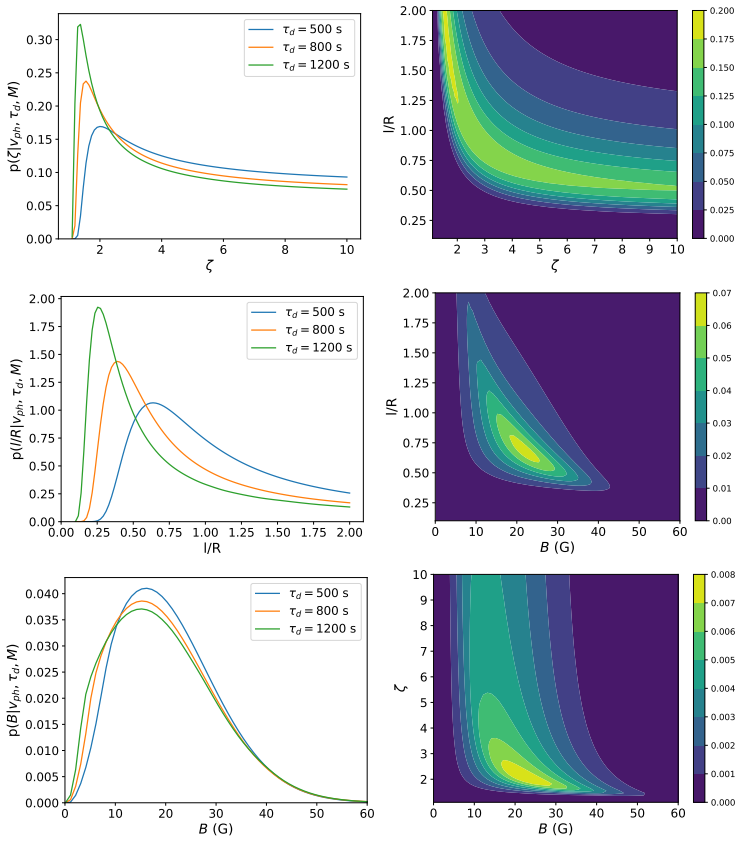

Figure 3.14: Left panels: Marginal posterior distributions of resonant absorption parameters (ζ, l/R) and magnetic field strength (B) for three different values of the observed damping time (τ_d) with an associated uncertainty of 50 s in all cases. The considered event is the same as in previous cases, with an observed phase speed $v_{ph} = (1030 \pm 410)$ km s^{-1} and length $L = 190$ Mm. Uniform priors have been used for all involved parameters. Right panels: Joint posteriors of l/R and ζ (top), l/R and B (middle), and ζ and B (bottom) for the first considered damping ratio value $\tau_d = (500 \pm 50)$ s.

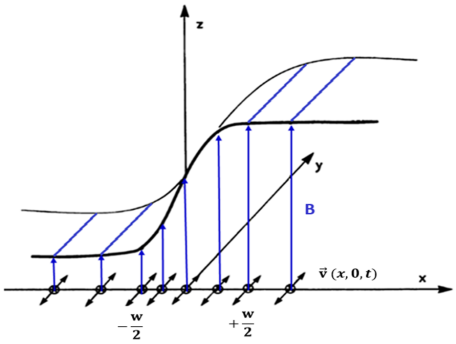

Figure 3.15: Sketch of the considered model for phase mixing. *Adapted from Heyvaerts & Priest (1983).*

ing the linear MHD equations in a weakly dissipative medium, an analytical expression for the damping ratio of Alfvén waves, later described by Roberts (2000) is obtained as

$$\frac{\tau_d}{P} = \left(\frac{3}{\pi^2 \nu}\right)^{1/3} w^{2/3} P^{-1/3}, \tag{3.5}$$

with ν the coronal kinematic shear viscosity coefficient ($\nu = 4 \times 10^{-3}$ Mm^2 s^{-1}) and w the transverse inhomogeneity length scale.

Although resonant absorption and phase mixing are in essence the same physical process (see the discussion by Cally & Maddison 1997 and Soler & Terradas 2015) but implying different types of waves and at different scales, phase mixing is not consistent with transverse motions observed in coronal loops. However, it is of great importance and has been deeply studied for years for its possible implications in the coronal heating problem (see e.g. Cally 2017; Ruderman & Petrukhin 2017; Pagano & De Moortel 2017; Pagano et al. 2018).

Phase mixing is included in this study by continuity in the discussion by Ofman & Aschwanden (2002), who proposed an alternative interpretation for this mechanism by involving the friction between adjacent unresolved thin loop strands with local Alfvén wave coupling. Thus, in spite of the fact that the formula in Eq. (3.5) is only valid in the strongly developed regime and the value of the kinematic viscosity is kept constant, we perform a Bayesian inference of the associated model parameters.

Note that in Eq. (3.5), the theoretical prediction does not enable to factorize the damping rate as a sole function of model parameters since the oscillation period is present at the right-hand side of this equation. For this reason, we perform the inference by assuming particular values for the period in the

range $P \in [150, 1250]$ s. This leaves us with an inversion problem with one observable, $d = \tau_d/P$, and one unknown, $\boldsymbol{\theta} = \{w\}$. When plausible values for this unknown are considered in the range $w \in [0.5, 20]$ Mm, theoretical damping ratios $\tau_d/P \sim [0.3 - 6]$ are obtained (Fig 3.16), matching well with values of observed damping time scales.

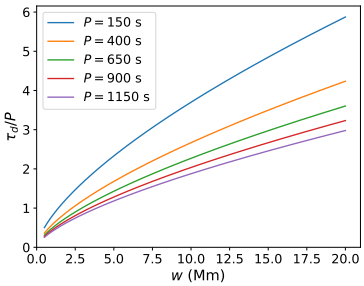

Figure 3.16: Values of the theoretical damping ratio as a function of the considered values of the inhomogeneity region width (w) for some fixed periods.

Figure 3.17 shows the resulting posterior distributions for this mechanism when a uniform prior is considered for the parameter w. As in Fig 3.13, different damping ratios and uncertainties have been analysed. Only the posteriors computed for the case $P = 150$ s are shown in panels a and b to not deface the plot. The posteriors shift toward larger values of w for longer periods (Fig. 3.17a). The inference results for this mechanism show that the length scale w can be properly inferred although a larger upper limit in the parameter range is needed for the case $\tau_d/P = 10$. The posteriors show broader distributions the larger the uncertainty in the observed damping ratio is (Fig. 3.17b) and move towards larger values of the parameter w with increasing periods (Fig. 3.17c).

3.4 Lateral Wave Leakage

Until now in this chapter, we had considered phenomena regarding transverse trapped modes in coronal loops. However, these structures in the corona can additionally support leaky modes, in particular the counterpart of the kink mode or principal leaky mode, that could play an important role in the observed damping of kink modes. In this context, Cally (1986) gave the theoretical principles of leaky modes in flux tubes but for years, several studies dismissed the principal leaky modes as a possible explanation of the damping in coronal loops, focusing on new scenarios with other types of leakage processes such as foot-point leakage (Ofman 2002), lateral leakage with curvature effects

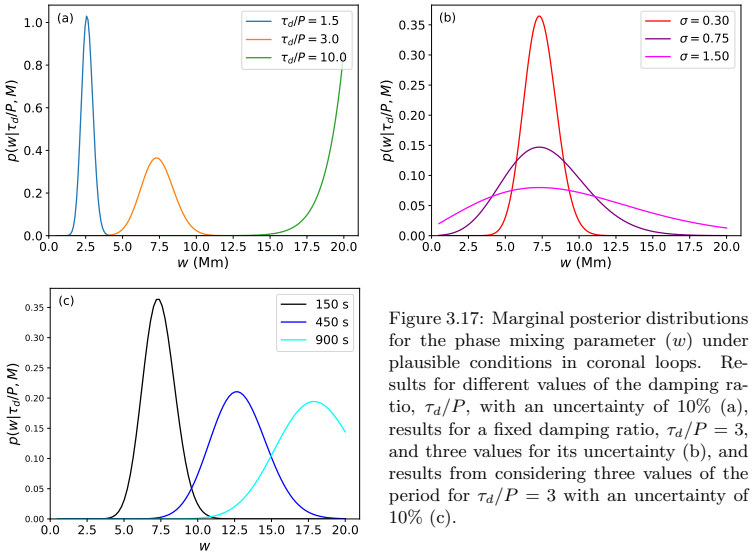

Figure 3.17: Marginal posterior distributions for the phase mixing parameter (w) under plausible conditions in coronal loops. Results for different values of the damping ratio, τ_d/P, with an uncertainty of 10% (a), results for a fixed damping ratio, $\tau_d/P = 3$, and three values for its uncertainty (b), and results from considering three values of the period for $\tau_d/P = 3$ with an uncertainty of 10% (c).

(Smith et al. 1997), gravity effects (Terradas et al. 2007), etc. Nonetheless, the damping times derived from all these studies are too long to be consistent with observations, except for lateral wave leakage of very short and thick loops (Cally 2003).

This lateral wave leakage mechanism proposed by Cally (2003) consists of a radiating wave oscillating with the kink mode frequency (principal leaky mode) that looses part of its energy to the background corona. The considered scenario for this mechanism is similar to the one for resonant absorption but here the non-homogeneous layer in the border of the tube is not included (Fig. 3.18), so that the possible influence of the density contrast is ignored. Following Cally (2003), the analytic approximate solution for the damping ratio under the TT assumption, takes the form

$$\frac{\tau_d}{P} = \frac{4}{\pi^4}\left(\frac{R}{L}\right)^{-2}, \tag{3.6}$$

valid for $\rho_i >> \rho_c$. If the considered values of this relation between radius and length are in the plausible range $R/L \in [10^{-4}, 0.3]$, theory predicts damping ratios in the range $\tau_d/P \sim (0.5 - 10^5)$, including observed values (Fig. 3.19).

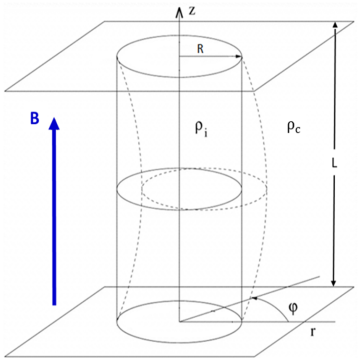

Figure 3.18: Sketch of considered model for wave leakage. *Adapted from Ruderman & Roberts (2002b).*

In this thesis, we have taken into account lateral wave leakage as plausible damping mechanism continuing with the discussion by Ofman & Aschwanden (2002), but also as a new approach to study this model. Due to limitations in instrumentation leaky modes cannot be resolved to extract information but can be important in the energetics of the oscillations.

It is appreciable in this case that the theoretical damping rate in Eq. (3.6) is only a function of the coronal loop radius to length ratio, R/L. This enables us to solve the inference problem with one observable, $d = \tau_d/P$, and one parameter, $\boldsymbol{\theta} = \{R/L\}$. Figure 3.20 shows the results for this mechanism. The ratio between the radius and the length of coronal loops can be properly inferred. The posterior distributions shift toward smaller values of R/L the larger the damping ratio is (Fig. 3.20a) and have broader shapes the larger the

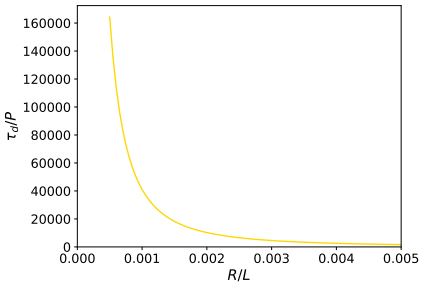

Figure 3.19: Values of the theoretical damping ratio as a function of the considered values of the relation between the radius and the length (R/L) of coronal loops.

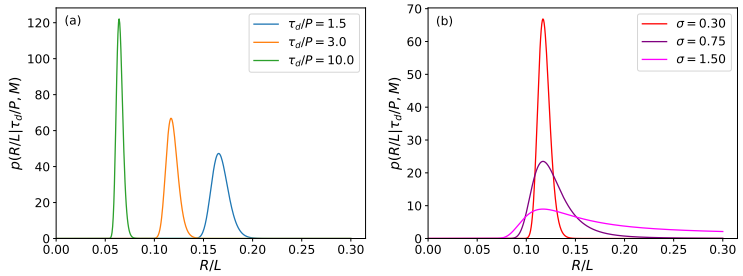

Figure 3.20: Marginal posterior distributions the wave leakage parameter (R/L) under plausible conditions in coronal loops. (a) Results for different values of the damping ratio, τ_d/P, with an uncertainty of 10%. (b) Results for a fixed damping ratio, $\tau_d/P = 3$, and three values for its uncertainty.

uncertainty in the observed damping ratio (Fig. 3.20b).

We remark here that many other mechanisms have been proposed for explaining observations of damped transverse waves in coronal loops, as for example the existence of currents or non-ideal effects. We have applied Bayesian techniques to those most cited mechanisms in literature for consistency with observations (resonant absorption, phase mixing, and wave leakage), though our methods are applicable to any other model that has a theoretical basis.

3.5 Comparison between Damping Models

Until now, we have focused on the inference of different physical properties and parameters of solar coronal loops by analysing standing kink modes with and without damping, and Alfvén waves. However, the difficulty in defining what a typical coronal loop is produces among other things a lack of consensus about which mechanism is at the origin of the observed damping. For that reason, multiple methods exist to assess the plausibility between alternative damping mechanisms (Roberts 2000; Ruderman 2005). For instance, Ofman & Aschwanden (2002) proposed a method based on the use of scaling laws between the observed periods and damping times. Their suggestion is based on the assumption that each damping mechanism is characterised by a particular power law, with a distinct power index between the damping time and the oscillation period. The application of this method has given results that support both phase mixing (Ofman & Aschwanden 2002) and resonant absorption (White & Verwichte 2012b; Verwichte et al. 2013). On the other hand, it was

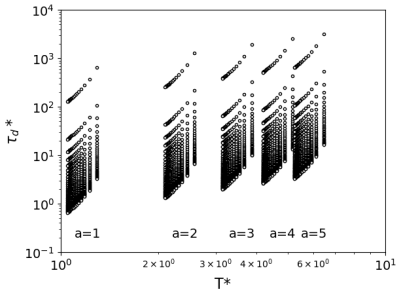

Figure 3.21: Different scaling laws between normalized damping times and periods by considering resonant absorption. Different values of model parameters have been considered. Adapted from Arregui et al. (2008).

pointed out by Arregui et al. (2008) that the use of scaling laws to discriminate between damping mechanisms is questionable, since the resonant damping model is able to produce data realisations for which different scaling laws with different indexes may be obtained (Fig. 3.21). The major drawback to the method by Ofman & Aschwanden (2002) is the faultiness of the assignment of a single power index to a particular damping mechanism, even more so when the damping time depends on a number of loop parameters that might have an intrinsic variability and values that are highly uncertain.

From our side and for the first time, we propose Bayesian statistics to compare between plausible damping mechanisms of transverse oscillations in coronal loops. The comparison is performed in two principal ways. First, we consider plausible values for the observed damping ratio, $d = \tau_d/P \in [0.01, 10]$, and compute the marginal likelihood in Eq. (2.3) associated to each damping mechanism in the previous Sections 3.2, 3.3, and 3.4, with uniform priors in the same ranges considered therein. Figure 3.22a shows the results from the computation of marginal likelihoods for the three considered damping mechanisms as a function of the damping ratio. Resonant absorption and wave leakage offer more plausible explanations for low damping ratio values, while the evidence for phase mixing attains larger values from low to intermediate values of the damping rate. We note that for phase mixing, as the analytic expression for the damping ratio is a function of the wave period, its marginal likelihood is computed for particular values of the period. These results are determined for a fixed value of the uncertainty on the observed damping ratio of 10%. Figures 3.22b-d show the marginal likelihoods separately for each mechanism, for three different values of the error on the measured damping ratio. In all three cases, increasing the uncertainty produces a decrease on the maximum value of the marginal likelihood, as well as some spread out of the distributions.

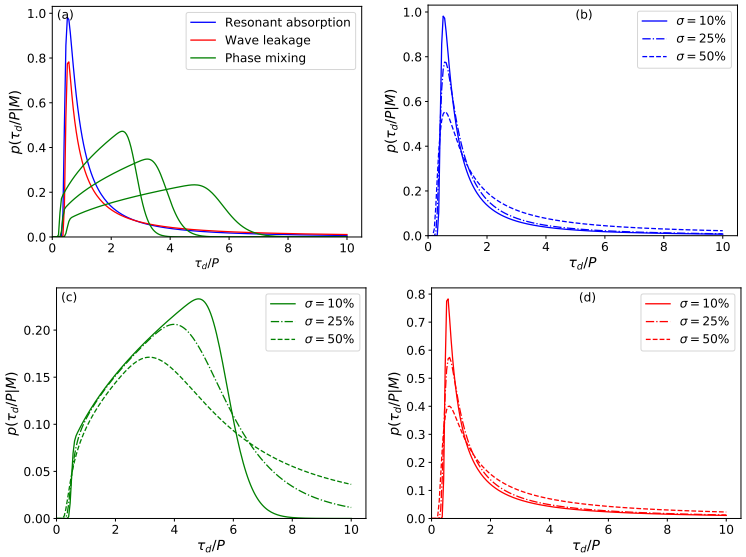

Figure 3.22: (a) Marginal likelihoods computed for the three considered models as a function of the observable damping ratio in the range $\tau_d/P \in [0.01, 10]$ for a fixed value of $\sigma = 10\%$. For phase mixing, three fixed values of period $(150, 500,$ and $1250\ s$ from right to left) have been taken. (b)-(d): Marginal likelihoods for each mechanism separately for three different values of uncertainties, $\sigma = 10\%, 25\%, 50\%$. For each mechanism the same colour as in panel (a) is applied.

Once we had a look to the marginal likelihoods to see the observable space in which the model shows more evidence, we compute the Bayes factors given by Eq. (2.7) in a one-by-one comparison as a function of the same range of observables. This gives us the quantitative assessment of the relative performance between the three damping mechanisms. In the following, we use the subscripts 0, 1, and 2, to identify resonant absorption, phase mixing, and wave leakage, respectively. Figure 3.23 shows the distribution of Bayes factors as a function of the damping ratio corresponding to one-to-one comparisons between the three mechanisms. An error measurement on the damping ratio of 10% is assumed. In Fig. 3.23a, we see that very strong evidence for resonant absorption in front of phase mixing is obtained for the lowest and the largest considered values of the damping ratio, in between 0 and 0.5 and for $\tau_d/P > 9$.

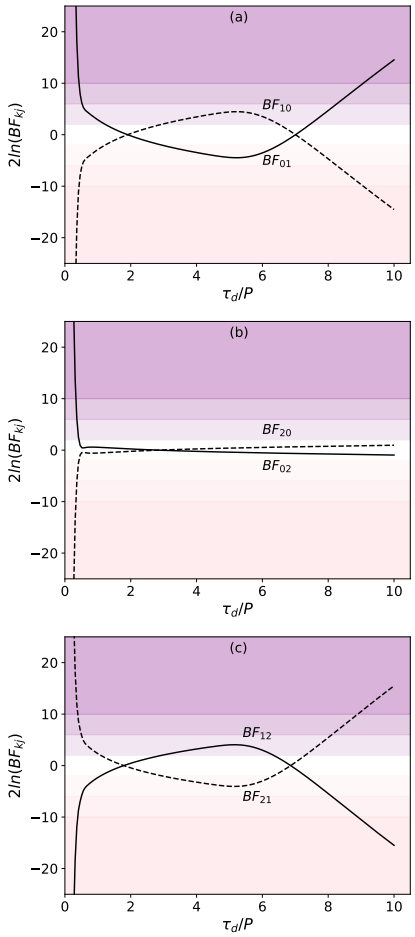

Figure 3.23: Bayes factors for the one-to-one comparison between resonant absorption, phase mixing, and wave leakage mechanisms, here represented with the subscripts 0, 1, and 2 respectively, in the range $\tau_d/P \in [0.01, 10]$ with uncertainty of 10%. For phase mixing, $P = 150$ s is fixed. Colours indicate levels of evidences in Table 2.2 with darker ones for stronger evidences.

The first interval corresponds to extremely strong damping regimes in which the damping time is shorter than the oscillation period. The second, to rather weak damping regimes. For intermediate damping ratio values, the evidence favours phase mixing, with values for $2\ln BF_{10}$ in between 2 and 5, which correspond to positive evidence, according to the levels of evidence in Table 2.2. For the comparison between resonant absorption and wave leakage, Fig. 3.23b shows very strong evidence in favour of resonant absorption again for the lowest values of the damping ratio, followed by a decrease of $2\ln BF_{02}$ until both Bayes factor lines intersect. For intermediate and large values of the damping ratio, the evidence is inconclusive since the magnitude of both Bayes factors is below ± 2. Finally, Fig. 3.23c shows the confrontation between phase mixing and wave leakage, with results that are akin to those between resonant absorption and phase mixing in Fig. 3.23a. Wave leakage is the favoured model for strong and weak damping regimes, while positive evidence for phase mixing is obtained in the intermediate damping regime with $\tau_d/P \in (2-7)$.

If we now think on values of damping ratios themselves, we deal with one particular value, as for example $\tau_d/P = 5$ gives information about how quick is the damping of the wave but not about individual values of the damping time or the period i.e., $\tau_d/P = 5$ can be obtained by multiple combinations of these two observables, such as $\tau_d = 10$ s and $P = 2$ s or by observing $\tau_d = 15$ s and $P = 3$ s. To extract then the maximum information, we calculate the Bayes factors between the three damping models in such a two-dimensional plane with the two observables of interest, the period and the damping time, $d = \{P, \tau_d\}$. The damping ratios resulting for different combinations of τ_d and P on a wide range of values have a fixed uncertainty of 10%.

Figure 3.24 shows the obtained Bayes factor distributions. The general conclusion is that the evidence for any of the considered models against an alternative depends on the particular combination of observed periods and damping times. In particular, for resonant absorption against phase mixing, Fig. 3.24a shows at the upper-left corner, corresponding to large values of the damping ratio, strong (purple) and very strong (grey) evidence in favour of resonant absorption. The lower-right corner corresponding to low damping ratios shows very strong evidence (white) in favour of the phase mixing model. In the remaining regions different coloured bands denote positive (pink for resonant and green for phase mixing) or insignificant evidence (yellow), depending on the particular combination of the two observables. In the comparison between resonant absorption and wave leakage, Fig. 3.24b, most of the (τ_d, P)- plane is coloured in yellow resulting in a lack of evidence for a particular model. Grey and purple regions (very strong and strong evidence) indicate the dominance of the resonant damping mechanism for the lowest values of the damping ratio

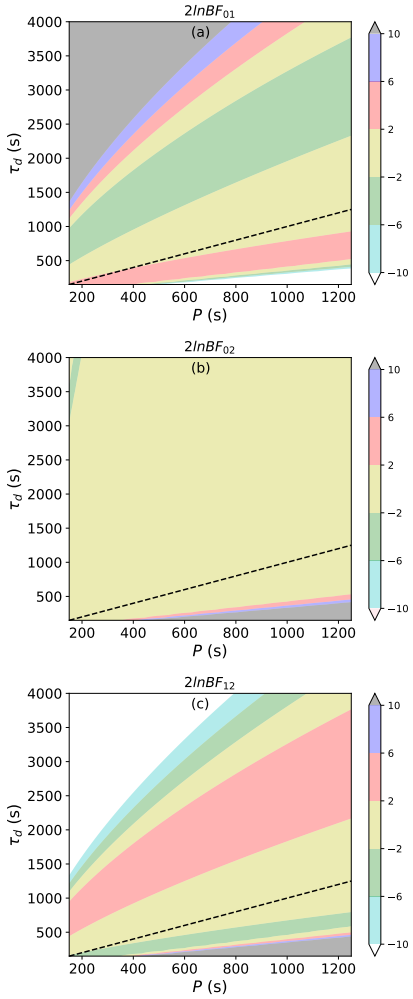

Figure 3.24: Bayes factors in the one-to-one comparison between resonant absorption, phase mixing, and wave leakage mechanisms as a function of the observables period (P) and damping time (τ_d) with uncertainties of 10% for each damping ratio resulting in each τ_d, P combination. The dashed lines indicate $\tau_d = P$. The different levels of evidence of Table 2.2 are indicated in the colour bars. NW (yellow), PE (green/red), SE (blue/purple), VSE (white/grey).

and positive evidence (green for wave leakage and pink for resonant) is found in very narrow regions of the plane of observables. Finally, Fig. 3.24c shows the results from the comparison between phase mixing and wave leakage. The white (very strong evidence) and the blue (strong evidence) regions are located at period and damping time combinations corresponding to large damping ratios and point out to the dominance of the wave leakage model over phase mixing. For low damping ratios, we find very strong evidence (grey) in favour of phase mixing. The remaining combinations lead to positive (pink for phase mixing and green for wave leakage) or inconclusive evidence (yellow) depending on the observables. In the three panels of Fig. 3.24, focusing in observations with values of the damping ratio larger than 1, which are located in the upper-left side of the dashed line, resonant absorption and wave leakage are more plausible than phase mixing but no distinction can be made to favour any of them. Phase mixing seems to be the most plausible mechanism in the intermediate region of the observable (τ_d, P)-plane (green colour in Fig. 3.24a and pink colour in Fig. 3.24c).

3.5.1 Application to Real Data

So far, model comparison is pursued by considering hypothetical values for observed periods, damping times, and their measurement errors. The full potential of the method here presented is discernible when applied to real events of damped transverse loop oscillations. For this reason, we consider a selection of 89 loop oscillation events for which periods and damping times are listed in the databases presented by Verwichte et al. (2013) and Goddard et al. (2016), discarding events for which errors were not reported. The considered events and their oscillation properties are presented in Table B.3. They are sorted in increasing value for their corresponding damping ratio value in order to locate the events easily according to results. We further include for each event the inferred parameters, computed following the methods described in Sections 3.2, 3.3, and 3.4.

Figure 3.25 shows scatter plots that display Bayes factor and damping ratio values for the selected 89 events for each one-to-one model comparison between our three damping mechanisms. The colours indicate the level of evidence, based on the magnitude of the corresponding Bayes factor. The Bayes factor values are also listed in Table B.3. The conspicuous result is that the blue colour, which corresponds to absence of evidence for any damping mechanism, dominates in all three panels.

For the comparison between resonant absorption and phase mixing (left panel), in approximately 78% of the events we have not sufficient evidence to

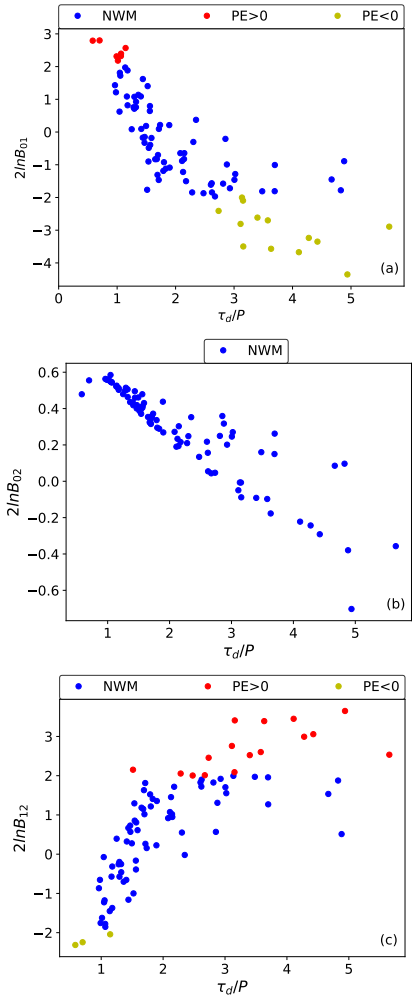

Figure 3.25: Representation of the Bayes factors computed for the 89 events selected from Verwichte et al. (2013) and Goddard et al. (2016) in Table B.3. The different panels correspond to the three one-to-one comparisons between resonant absorption, phase mixing, and wave leakage, here represented with the subscripts 0, 1, and 2 respectively.

favour one model or the other (NWM). Some events (coloured in red and yellow) show positive evidence for either resonant absorption or for phase mixing. The evidence is positive for resonant absorption in 8% of the events, with strong damping (low values of τ_d/P) and positive evidence for phase mixing in about 14% of the events, with damping ratio values in between 3 and 6. In the middle panel, the analysis for resonant absorption vs. wave leakage is shown. In all events the Bayes factor and therefore the evidence is not strong enough to support any of the two mechanisms. Finally, the right panel shows the comparison between phase mixing and wave leakage. For 79% of the events the evidence is inconclusive, with the events distributed among the full range of damping ratios. Only for 3% of the events we obtain positive evidence in favour of wave leakage, for loop oscillations with very strong damping, and for another 18% positive evidence in favour of phase mixing.

3.6 Propagating Waves

Observations of fast propagating waves by CoMP (Tomczyk et al. 2007; Tomczyk & McIntosh 2009) opened a new window for researching conditions in coronal loops within coronal seismology. Those oscillations showed also damping in a very few periods. Then, theory for the spatial damping of fast propagating kink waves due to resonant absorption was rapidly developed by a number of studies (Terradas et al. 2010; Verth et al. 2010; Soler et al. 2011c,b; Hood et al. 2013), which indicated that the amplitude decays in space along the loops in an analogous way in which time damping occurs for standing waves. However, simulations by Pascoe et al. (2012, 2013) showed that the commonly used exponential decay considered in previous analyses does not fit well to the simulated amplitude decays, with a Gaussian profile being more plausible at the beginning of the decrease in amplitude produced by the damping process.

Hence, under the same assumptions considered for temporal resonant absorption in Section 3.2, an analytical expression for the spatial damping ratio can be derived, with the form (Hood et al. 2013; Pascoe et al. 2013)

$$\frac{L_d}{\lambda} = \left(\frac{2}{\pi}\right)^2 \frac{R}{l}\frac{\zeta+1}{\zeta-1} \tag{3.7}$$

for an exponential decay or

$$\frac{L_g}{\lambda} = \frac{2}{\pi}\left(\frac{R}{l}\right)^{1/2} \frac{\zeta+1}{\zeta-1} \tag{3.8}$$

for a Gaussian one. Here L_d, L_g are the damping lengths for exponential and Gaussian profiles respectively, λ is the wavelength of the fast propagating

wave, l/R and ζ are the cross-field inhomogeneity parameters (length scale and density contrast described in Section 3.2). The first factor in the equations corresponds to a linear density variation at the non-uniform layer, resulting in a right-hand term identical to the one for the damping time over the period for standing kink waves, if the same density profile is applied. It must be noted that in Chapter 3.2 a sinusoidal density profile was used when temporal damping of standing kink waves was considered.

These analytical expressions have been already employed together with Bayesian techniques by Arregui et al. (2013b) searching for the transition point between both profiles and the parameters of transverse density structuring. Since then, the interest in damping of fast propagating waves has decreased because of the remaining necessity of high quality data. For this reason, we decided to revise and complete the work by Arregui et al. (2013b) with tools developed here.

In particular, we infer those parameters linked to the density structuring as in the cited work but considering a slight modification. In this case, we assume each profile separately i.e., resonant absorption of propagating waves occurs following a unique profile, exponential or Gaussian, from the beginning to the end. This fact could be seemed a step back regarding the previous study, however differences in parameters derived by one or the other profile require attention, since they indicate changes in plasma conditions. In this way, we obtain marginal posteriors for the model parameters in Eqs. (3.7) and (3.8) associated to exponential ($\boldsymbol{\theta_d} = \{\zeta_d, l/R)_d\}$) and Gaussian profiles ($\boldsymbol{\theta_g} = \{\zeta_g, l/R)_g\}$). To perform such a task, we consider uniform priors over the same plausible ranges than in resonant absorption of standing waves i.e., $l/R \in [0.01, 2]$ and $\zeta \in [1.1, 10]$, and an observable spatial damping ratio of $d = L_d/\lambda = L_g/\lambda = 3.0 \pm 0.3$. Figure 3.26 shows the resulting posterior distributions for the density contrast and the thickness of the non-uniform layer for both damping profiles. In general, all distributions can be inferred although they show long tails. Regarding the density contrast (Fig. 3.26a), the posterior distribution associated with the exponential damping profile (black) reaches a maximum probability in a small value of the parameter, $\zeta_{d,\max} \simeq 0.19$, while the posterior distribution corresponding to Gaussian damping profile peaks in a density contrast equal to $\zeta_{g,\max} \simeq 0.09$. If we now analyse the results for the thickness of the non-uniform layer (Fig. 3.26b), the tendency is the opposite. Smaller values of the parameter are better explained by a Gaussian damping profile (red) with maximum probability in $l/R)_g = 0.05$, while the distribution associated with the exponential profile peaks at $l/R)_d = 0.14$.

In conclusion, taking one simple observation, different structures of the coronal loops are plausible depending on the assumed decay. While a dense

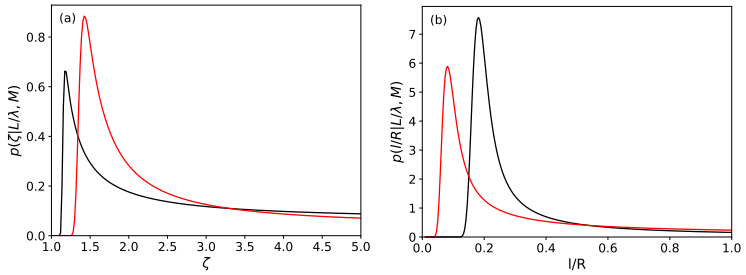

Figure 3.26: Marginal posterior distributions for cross-field density structuring parameters under the assumption of an exponential (black line) or a Gaussian (red line) decay of propagating oscillations by resonant absorption in coronal loops. An spatial damping ratio of $L_d/\lambda = L_g/\lambda = 3$ has been fixed with an associated uncertainty of 10%.

loop with a short transition region is more suitable by considering a Gaussian profile, a loop with the density comparable to the background corona density and a wider transition layer is obtained considering an exponential profile in the study.

On the other hand, we have seen the utility of Bayesian statistics in comparing between models. So, we decided to apply the same tools developed in comparing damping models for confronting exponential and Gaussian profiles. As in Section 3.5, we first obtain results from the marginal likelihood computations taking a range of observables of $L/\lambda \in [0.01, 10]$. The results are represented in Fig. 3.27 (note that L does not denote the loop length, it indicates a generic damping length in the remaining of this section). It is appre-

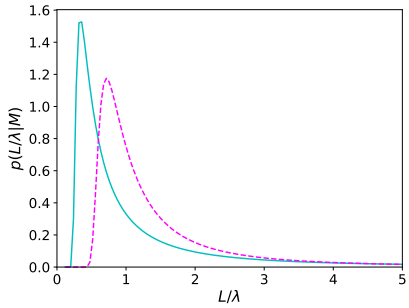

Figure 3.27: Marginal likelihoods for exponential (blue continuous line) and Gaussian (purple dashed line) decays by resonant absorption. The observable values have been taken in the interval $L/\lambda \in [0.01, 10]$ with an associated uncertainty of 10%. Here, L/λ-axis goes up to 5 for clarity.

ciable that for observable values smaller than about the unity (corresponding with damping lengths smaller than the wavelength) the exponential profile is the most probable, while spatial damping ratios of about 1 are better explained by the Gaussian decay. For the rest values of L/λ values the evidence is not large enough to support any profile.

The next step in the analysis of propagating oscillations is to compute the Bayes' factors as a function of the same spatial damping ratio considered before. Figure 3.28 shows the results. We have labelled the exponential profile with the number 0 and the Gaussian one with 1. Thus, we can see that the exponential profile shows strong evidence in very strong damping regimes but for the rest of the observed ratios the evidence does not support any of the two considered profiles.

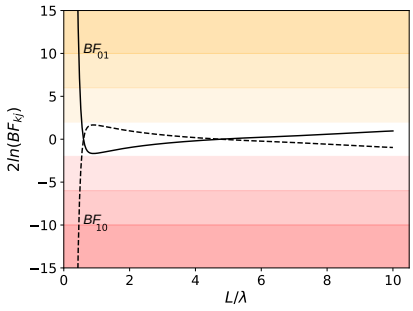

Figure 3.28: Bayes factors for the comparison between exponential and Gaussian decays, here represented with the subscripts 0 and 1 respectively. Values in the range $L/\lambda \in [0.01, 10]$ have been considered with an uncertainty of 10%. Colours indicate levels of evidence in Table 2.2.

Finally, we split as in the previous section the spatial damping ratio in the two dimensional space of observables, the damping length (L) and the wavelength (λ). Results from this computation are shown in Fig. 3.29 with colours indicating the level of evidence indicated in Table 2.2 and the dashed black line displaying $L = \lambda$. In general, the evidence is not strong enough to support any profile (blue) in almost all the observable plane, except for values at the right bottom corner with very strong evidence and green bands with positive evidence in favour both cases of the exponential profile.

To conclude, when we compare between exponential and Gaussian profiles for damping of propagating waves, the exponential decay seems to be more likely at very early locations while the Gaussian one seems to fit better at a specific point, but in general the evidence does not support any of them in a conclusive way.

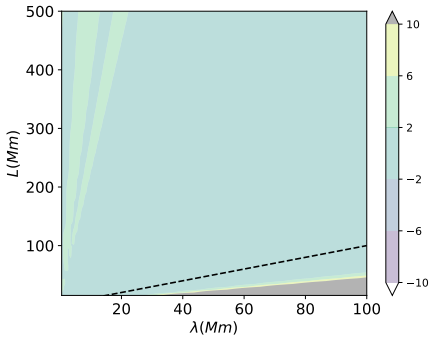

Figure 3.29: Bayes factors in the comparison between exponential and Gaussian decays by resonant absorption as a function of the observables length (L) and wavelength (λ) with uncertainties of 10% for each spatial damping ratio resulting in each L, λ combination. The dashed lines indicate $L = \lambda$. The different levels of evidence of Table 2.2 are indicated in the colour bars. NW (blue), PE (dark blue/green), SE (purple/green), VSE (white/grey).

3.7 Conclusions

In this chapter, we have inferred several physical properties of solar coronal loops applying Bayesian techniques, with the following results:

- Regarding the inference of physical properties in coronal loops, the internal Alfvén velocity and the magnetic field strength can be inferred for any observed transverse oscillation event. Changes in the considered density contrast range do not produce significant variations in the posterior of the magnetic field strength. However, this is not the case if we introduce an estimation of the coronal loop density, or we change the range for its plausible values. Hence, information on the density of the loops is crucial. In addition, the values of magnetic field strength have been updated for a large amount of events.

- With respect to resonant absorption in the Alfvén continuum, the density contrast and the inhomogeneity scale can be inferred with both attaining smaller values for larger damping ratios. When we introduce resonant absorption as an extra source of information to determine the magnetic field strength, parameters associated to the cross-field density structuring are constrained worse and the posterior distribution corresponding to the magnetic field strength is almost unaffected.

- When phase mixing or wave leakage are considered as plausible damping mechanism, the width of the inhomogeneity region and the ratio between radius and loop length can be inferred.

Apart from inferring physical features of coronal loops, we have performed with Bayesian tools, the comparison between damping models, as well as a comparison between Gaussian and exponential decays under resonant absorption. The main conclusions are:

- Concerning the comparison between damping models, the evidence is not large enough to support neither resonant absorption nor phase mixing or wave leakage, since plausibilities depend on the particular values of the damping time and the period for each observed event.
- For propagating waves, exponential or Gaussian decays are suitable for different coronal loop conditions when the same observable is considered. When both exponential and Gaussian profiles are compared, realistic spatial damping ratios do not provide us with evidence in favour of any of the profiles.

4

Bayesian seismology of prominence threads *

When the sun is in eclipse and disappears,
you can see its greatness.
Lucio Anneo Séneca

UNDERSTANDING the physical plasma conditions, dynamics, and energetics of solar prominences is a challenge. High resolution imaging observations in H_α with e.g., the Swedish Solar Telescope (SST) and Hinode have enabled us to resolve the fine structures forming the prominence bodies. These structures consist of fine threads not thicker than $\sim$ 0.2 - 0.3 arc sec ($\sim$ 145 - 218 km) (Lin 2004; Lin et al. 2005; Okamoto et al. 2007; Lin et al. 2008). Characterising the physical properties and dynamics of these fine threads is key to understanding the field of solar prominences.

Ample observational evidence exists about the presence of waves in prominences (Oliver & Ballester 2002; Arregui et al. 2018). These observed waves are classified in large and small amplitude oscillations and imply both transverse or longitudinal motions with respect to the structures (see e.g. Yi et al. 1991; Yi & Engvold 1991; Terradas et al. 2002; Foullon et al. 2004; Berger et al. 2008;

*This chapter is based on: M. Montes-Solís and I. Arregui, 2019, Astronomy & Astrophysics, **622**, A88 (12pp) (Montes-Solís & Arregui 2019b); and M. Montes-Solís and I. Arregui, 2019, Highlights on Spanish Astrophysics X, Proceedings of the XIII Scientific Meeting of the Spanish Astronomical Society held on July 16 - 20, 2018, in Salamanca, Spain. B. Montesinos, A. Asensio Ramos, F. Buitrago, R. Schödel, E. Villaver, S. Pérez-Hoyos, I. Ordóñez-Etxeberria (eds.), **514** (6pp) (Montes-Solís & Arregui 2019a).

Tripathi et al. 2009). Focussing on small amplitude oscillations, these waves display a wide range of periods and typical velocity amplitudes consistent with the timescales of transverse motions in threads reported by Lin et al. (2007, 2009). Mass flows have also been detected, with velocities in the range 15 – 46 km s^{-1} (Zirker et al. 1998; Lin et al. 2005; Okamoto et al. 2007; Ning et al. 2009). These plasma flows can possibly affect wave propagation properties.

Several theoretical models with different levels of complexity have been proposed to explain prominence thread oscillations. Simple fibril models under the zero plasma-β approximation in Cartesian geometry (Joarder et al. 1997; Díaz et al. 2001) laid the foundations of thread oscillation studies to more complex and realistic models in cylindrical geometry focussed on fast magneto-hydrodynamics wave properties (Díaz et al. 2002; Dymova & Ruderman 2005). Posterior studies by Soler & Goossens (2011) considered the influence of mass flows on the different oscillating modes.

Damping of transverse waves in threads is a commonly observed phenomenon with typical ratios of the damping time to the period in the range 1 to 10 (Arregui et al. 2011). Diverse mechanisms have been considered to explain the damping process in threads. Non-ideal effects were considered in uniform media with and without flows (Carbonell et al. 2004; Terradas et al. 2005; Carbonell et al. 2006; Carbonell et al. 2009), in stratified media with and without flows (Soler et al. 2007, 2008; Soler et al. 2009) and with partial ionisation effects (Forteza et al. 2007, 2008). Among partial ionisation effects, only Cowling's diffusion seems to be efficient enough to produce strong damping compatible with observations (Soler et al. 2009b,a). Wave leakage has also been considered as damping mechanism (van den Oord & Kuperus 1992; Schutgens 1997a,b; van den Oord et al. 1998) but some issues such as different damping rates for vertical and horizontal oscillations still remain unclear (Schutgens & Tóth 1999; McLaughlin & Hood 2006; McDougall & Hood 2007). Resonant absorption of kink waves in the Alfvén continuum, first proposed by Arregui et al. (2008) in the context of prominence threads, is another candidate to explain this phenomenon with damping timescales compatible with those observed. In a subsequent work by Soler et al. (2009c), damping from resonant absorption in the slow continuum was further considered, but for typical prominence parameters, the resulting damping times seem to be too long in comparison to those observed. Additional information on damping mechanisms for prominence oscillations can be found in Arregui & Ballester (2011) and Arregui et al. (2018).

Apart from the aforementioned standing waves, the ubiquitous presence of propagating fast transverse waves was reported by Tomczyk et al. (2007) through the analysis of measurements by CoMP. Although most of studies concerning to propagating oscillations have been focused on coronal loops con-

ditions, they are in general adaptable to any coronal wave-guide, including prominence threads. Hence, specifying for particular conditions in these structures, Soler et al. (2011a) gave the analytical damping lengths for resonant absorption and Cowling's diffusion of a partially ionised plasma and determined the insignificant role of Cowling's diffusion in front of resonant damping under certain thread conditions. However, whether propagating waves damp having an exponential, a Gaussian, or a more general profile remains under intense discussion.

In this chapter, we will perform Bayesian seismological studies of standing and propagating oscillations in prominence threads. In Section 4.1, we will start by analysing the magnetic field strength of quiescent prominence threads by assuming standing waves supported by fully and partially filled flux tubes. Parameters of plausible damping models will be inferred in Section 4.2, where a comparison of their plausibility in explaining observations will be further carried out. In Section 4.3, the relation between the fundamental and the first overtone kink mode period will be considered in order to infer the lengths and densities of threads under the short and long thread approximations. Plausible values of the period ratio for both limits, short and long will be also displayed. Next in Section 4.4, observed flows in prominence threads will be included in the inhomogeneous tube model, so that the total length of flux tubes in threads will be inferred by analysing the temporal evolution of the wave period. Regarding propagating oscillations, in Section 4.5 exponential and Gaussian decays will be studied in the particular case of prominence threads. Finally, our main conclusions will be exposed in Section 4.6.

4.1 Magnetic Field Strength

In Chapter 3, the magnetic field strength of coronal loops was inferred under different considerations, with the result that the measurement of the density turns out to be of vital importance. In this section, we apply the same theoretical and Bayesian methods in the framework of prominence threads.

4.1.1 Totally Filled Homogeneous Tubes

We first assume that threads can be modelled as homogeneous thin flux tubes with an internal prominence density, ρ_p, in a coronal environment with density ρ_c, similarly to the model considered for coronal loops (Fig. 3.3). Under this assumption, the phase speed of fast kink modes in threads can be simply expressed by the same Eqs. (3.1) and (3.2). However, typical density contrast values in prominence threads are sufficiently large to further simplify those

equations as

$$v_{ph} = c_k = \sqrt{2} v_{Ai} \text{ and } v_{ph} = \sqrt{\frac{2}{\mu_0 \rho_p}} B. \tag{4.1}$$

Figure 4.1 shows the dependence of the kink (or phase) speed with density contrast. The adequacy of the large contrast approximation is visible for values larger than 200, typical in principle of prominence threads.

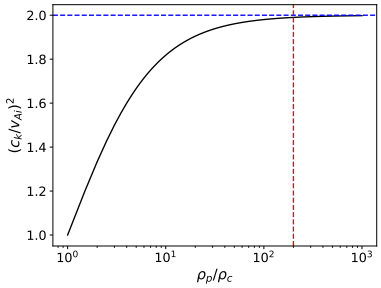

Figure 4.1: Kink speed (c_k) variability with the density contrast (ζ). Red and blue dashed lines indicate the approximated value of the density contrast and kink speed respectively from which the curve tends to 2. *Inspired on panel a in Fig. 3.8 by Soler et al. (2009b).*

Observationally, the phase speed of transverse kink waves in quiescent prominence threads can be estimated (Lin et al. 2009). By assuming that the phase speed estimated from observations is equal to the kink speed, $v_{ph} \approx c_k$, given in Eq. (4.1) and taking this as the observable data, $d = v_{ph}$, the inference of the unknown parameters $\boldsymbol{\theta} = \{\rho_p, B\}$ can be attempted.

In their analysis, Lin et al. (2009) took a fixed value of $\rho_p = 5 \times 10^{-11}$ kg m^{-3} and solved Eq. (4.1) for the magnetic field strength in a forward analysis. Their results for the 10 analysed threads are shown in the third column of Table 4.1. The assumption of a particular value of ρ_p enables in principle to estimate the magnetic field strength. The main drawback of this procedure is that the density of prominence plasmas is highly uncertain and difficult to estimate with some accuracy. Repeating the procedure for values of density in an extended plausible range leads to a variability in the inferred magnetic field strength, see Fig. 4.2a.

In contrast, we have performed the Bayesian inference of the magnetic field strength by assuming uniform priors in Eq. (2.14) for both parameters. Assuming plausible ranges for $B \in [0.01, 50]$ G and $\rho_p \in [10^{-12}, 10^{-9}]$ kg m^{-3}, theoretical model predictions cover the range of phase speeds $v_{ph} \in (0 - 6000)$ km s^{-1}.

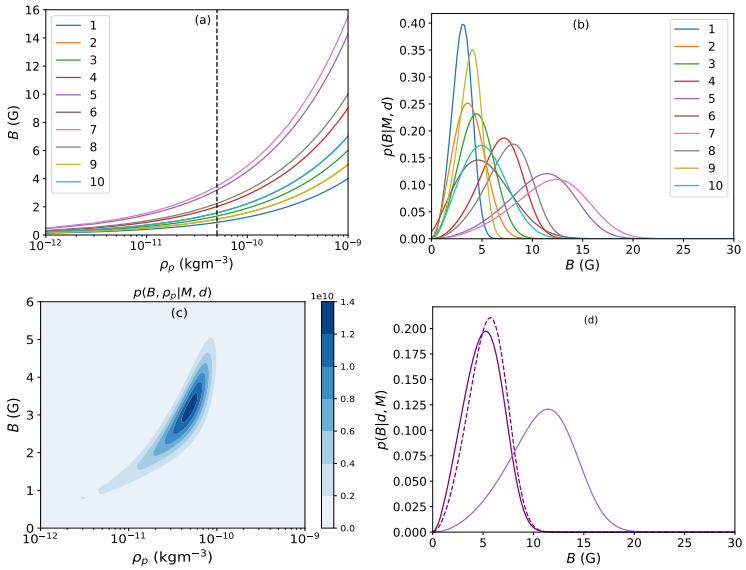

Figure 4.2: (a) Curves obtained for each observed thread by Lin et al. (2009) in the forward problem using Eq. (4.1). (b) Posterior distributions of magnetic field strength (B) for each considered thread obtained with Bayesian methods. Each number and colour in (a) and (b) correspond to each observed thread according to legends and Table 4.1. (c) Global posterior computed for the fifth thread, considering a Gaussian prior of the internal density (ρ_i) centred in a value equal to $\rho_p = 5 \times 10^{-11}$ kg m^{-3} and given an uncertainty of 50 %. (d) Comparison of posterior distributions of the magnetic field strength in totally filled tube (purple line), partially filled tube (magenta line), and partially filled tube considering a Gaussian prior for the proportion of thread length centred in $L_p/L = 0.5$ with 50% of uncertainty (dashed magenta line).

Thread #	v_{ph} (km s^{-1})	B_{Lin} (G)	B_u (G)	B_G (G)	B_u^{par} (G)	B_G^{par} (G)
1	16 ± 3	0.9 ± 0.3	3^{+1}_{-1}	$1.0^{+0.3}_{-0.2}$	2 ± 1	1.8 ± 0.5
2	20 ± 6	1.1 ± 0.5	4^{+2}_{-2}	$1.2^{+0.5}_{-0.4}$	2 ± 1	2 ± 1
3	24 ± 6	1.3 ± 0.5	5^{+2}_{-2}	1.5 ± 0.5	2 ± 1	3 ± 1
4	36 ± 6	2.0 ± 0.4	7^{+2}_{-2}	2.2 ± 0.6	4 ± 1	4 ± 1
5	57 ± 9	3.2 ± 0.7	11^{+4}_{-3}	3.4 ± 0.9	5 ± 2	6 ± 2
6	28 ± 12	1.6 ± 0.9	5^{+3}_{-3}	$1.7^{+0.8}_{-0.7}$	3^{+2}_{-1}	3^{+2}_{-1}
7	62 ± 10	3.5 ± 0.8	12^{+4}_{-4}	4 ± 1	6 ± 2	6 ± 2
8	40 ± 6	2.3 ± 0.8	8^{+3}_{-2}	2.4 ± 0.6	4 ± 1	4 ± 1
9	20 ± 3	1.1 ± 0.2	4^{+1}_{-1}	1.3 ± 0.3	2 ± 1	$2.3^{+0.5}_{-0.8}$
10	28 ± 9	1.6 ± 0.7	5^{+2}_{-3}	$1.7^{+0.7}_{-0.6}$	3^{+2}_{-1}	3 ± 1

Table 4.1: Summary of results from the analysis of threads observed by Lin et al. (2009). The columns contain the thread number (#), the phase velocity (v_{ph}), the magnetic field strength derived by Lin et al. (2009) (B_{Lin}), and the median and errors at the 68% credible interval for the magnetic field strength computed using uniform priors (B_u), Gaussian priors for the density of the thread (B_G), and for a partially filled tube using uniform priors (B_u^{par}), and Gaussian priors for the proportion of thread (B_G^{par}).

Figure 4.2b shows the Bayesian inference result obtained for each thread analysed by Lin et al. (2009), in terms of marginal posterior distributions for the magnetic field strength. The median and errors at the 68% credible interval are given in Table 4.1. For all threads, the marginal posteriors can be properly inferred. Figure 4.2b shows that the distributions spread over a range of values ranging from below 1 up to 20 G, despite the fact we are considering values up to 50 G as plausible. When we compare this finding with the classic result in Fig. 4.2a, the difference now is that the values of magnetic field strength that spread over a given range because of the variability in density, now have a different plausibility given by the Bayesian analysis. For instance, values of the magnetic field strength for thread number 7 (pink) range from a little above 0 to 16 G approximately when inserting the typical density in Eq. (4.1) (see Fig. 4.2a). However, in panel b of the same figure, we clearly see that among all those values, magnetic field strength values in between 10 to 15 are more likely. It is worth noting that the distributions for different threads belonging to the same prominence display rather different maximum a posteriori estimates. This is indicative of the highly inhomogeneous nature of the magnetic field strength

at small scales. Note that the transverse non-uniformity of the field strength would need to be counteracted by gas pressure forces to provide the constant total pressure in the transverse direction, which is an ingredient that has not been included in the model under consideration. If we compare our results using uniform priors and a range of density values (column B_u in Table 4.1) with those by Lin et al. (2009) using a fixed prominence density (column B_{Lin} in Table 4.1) we appreciate significant differences. The results by Lin et al. (2009) seem to be more precise and ours more uncertain. This is because Lin et al. (2009) remove all the uncertainty on the prominence density.

Instead of fixing a value of the density as in Lin et al. (2009), Bayesian methods enable us to mimic this by considering a Gaussian prior centred in $\rho_p = 5 \times 10^{-11}$ kg m^{-3} and with some uncertainty. An example result is shown in Fig. 4.2c where the joint posterior for the magnetic field strength and the density for the thread number five is plotted. Now, comparing the column B_{Lin} with the column B_G corresponding to calculations with Gaussian priors in Table 4.1, we see that we obtain similar results, with the advantage that the Bayesian results have the uncertainty correctly propagated. If we compare the result for thread number five using uniform prior (purple line in Fig. 4.2b or its summary value in Table 4.1), with that obtained using the Gaussian prior, we see that a better constrained magnetic field strength is inferred for this latter case. The accuracy in the magnetic field strength inference thus depends strongly on the precision in observationally estimated prominence densities. In the absence of information on the internal density, this parameter cannot be properly inferred, as has been noted in Fig. 3.5c of Section 3.1 in the context of coronal loop oscillations. Figure 4.3 shows posterior distributions for the magnetic field strength, for the fifth thread, computed using different priors for the density. Besides the uniform prior, two Gaussian priors centred at two density values are used. The results for each case clearly differ.

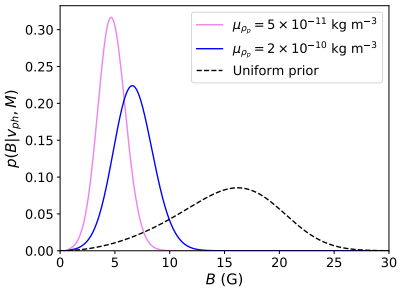

Figure 4.3: Posterior distributions of the magnetic field strength (B) considering a Gaussian prior of the internal density (ρ_i) centred in a value equal to $\rho_p = 5 \times 10^{-11}$ kg m^{-3} (pink), a Gaussian prior centred in a value equal to $\rho_p = 2 \times 10^{-10}$ kg m^{-3} (blue), and a uniform prior (black dashed line). Uncertainties in Gaussian priors are considered to be of 50 %. The totally filled tube and the plausible ranges for the parameters of Fig. 4.2 have been assumed.

Hence, density measurements are key to determine more accurately magnetic field strength values in prominence threads.

4.1.2 Partially Filled Inhomogeneous Tubes

According to observations, prominence threads are cool over-densities immersed in longer flux tubes. Theoretically, these inhomogeneous tubes are anchored to the photosphere through the so-called evacuated plasma region (Fig. 4.4), whose density value (ρ_e) is normally considered to be similar to that in the corona ($\rho_e \approx \rho_c$). If we then consider the thread with length L_p as part

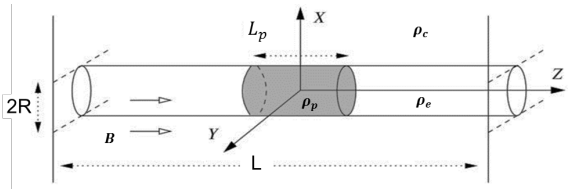

Figure 4.4: Sketch of a partially filled tube. *Adapted from Díaz et al. (2002).*

of a longer flux tube of total length L, the period can be approximated by $P \approx \pi\sqrt{L_p(L-L_p)}/\sqrt{2}v_{Ai}$ (Soler et al. 2010). This period can be easily transformed to phase velocity ($v_{ph} = 2L/P$) with the following form

$$v_{ph}^{par} = \frac{2}{\pi\sqrt{\frac{L_p}{L}\left(1-\frac{L_p}{L}\right)}} v_{ph}^{tot}, \tag{4.2}$$

where we have denoted v_{ph}^{tot} for the phase velocity in Eq. (4.1) for the totally filled tube and v_{ph}^{par} for a partially filled tube. In this model, the space of parameters becomes larger with the ratio between the length of the thread and the total length, L_p/L, as an additional parameter. Under these conditions, we inferred the magnetic field strength for each thread analysed by Lin et al. (2009) to quantify the differences with the previous results using the fully filled homogeneous tube. Figure 4.2d shows an example of comparison between the marginal posteriors for the magnetic field strength in a totally filled tube (purple line) and in a partially filled tube (magenta line) for the thread number five. Uniform priors have been considered for all parameters with the ratio of the length of the thread to the total length in the plausible range $L_p/L \in (0,1)$, which includes values in between the two limiting cases of $L_p/L = 0$ (the thread does not exist) and $L_p/L = 1$ (the thread occupies the full length of the tube).

The posterior distribution for the partially filled tube shows more constrained values of the magnetic field strength than the posterior corresponding to the totally filled tube (see the median values at the sixth column of Table 4.1). Additionally, it peaks at a smaller value of this parameter. Figure 4.2d further includes a dashed magenta line resulting from considering a Gaussian prior for the new parameter centred at $L_p/L = 0.5$ with an uncertainty of 50%. In the last column of Table 4.1 the corresponding median value of the magnetic field strength for each thread has been included. Solutions are very similar to those obtained by considering a uniform prior over the full range of L_p/L.

The previous analyses are not only valid for quiescent prominence threads but also for active region prominence threads provided measurements of phase speeds or total lengths are available.

4.2 Damping Models

Damping of transverse oscillations is a commonly observed phenomenon in threads, see e.g. Ning et al. (2009). A number of theoretical models have been put forward to explain the damping process in prominences (Arregui & Ballester 2011). In this work, we consider three damping mechanisms, namely resonant absorption in the Alfvén continuum (Arregui et al. 2008); resonant absorption in the slow continuum (Soler et al. 2009c); and Cowling's diffusion in a partially ionised plasma (Soler et al. 2009a,b) to extract information of physical features in prominence threads and to compute the plausibility of each damping mechanism in explaining observations, in a similar way as it was done in Chapter 3 for coronal loops.

4.2.1 Infinitely Long Tubes

The first selected damping model is resonant absorption in the Alfvén continuum, considering the same infinite and thin magnetic tube that we adopted for coronal loops as certain (Fig. 3.10). It was suggested in the context of prominence plasmas by Arregui et al. (2008). Considering large density contrast ratios, $\rho_p >> \rho_e$, the damping ratio in Eq. (3.3) only depends on the transverse inhomogeneity length scale in the form

$$\frac{\tau_d}{P} = \frac{2}{\pi}\frac{R}{l}. \tag{4.3}$$

Thus, the use of observational values of the damping ratio, $d = \tau_d/P$, and the theoretical expression in Eq. (4.3), permits to infer the damping model

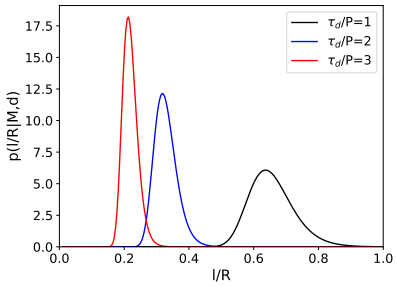

Figure 4.5: Posterior distributions of the thickness of non-uniform layer (l/R) for resonant absorption in the Alfvén continuum. Three different damping ratios (τ_d/P) with an associated uncertainty of 10% are considered.

parameter for resonant absorption in the Alfvén continuum, $\boldsymbol{\theta} = \{l/R\}$. As for coronal loops, the possible values that l/R can take are restricted by the model itself with $l/R = 0$ for a tube with a jump on density between ρ_p and ρ_c and $l/R = 2$ for a fully non-uniform continuous variation of density. This leads to theoretically predicted damping ratios in the range $\tau_d/P \approx [0.3, \boldsymbol{\infty})$, compatible with observed values in prominence threads.

Figure 4.5 shows resulting posterior distributions for the damping model parameter when a uniform prior and three different values of the damping ratio with a given uncertainty are considered. All distributions can be inferred with short values of l/R being more plausible for larger damping ratio values. These results are akin to those obtained in the previous Chapter 3 for the transverse inhomogeneity length scale in coronal loop oscillations damped by resonant absorption.

The next considered damping model in prominence threads is resonant absorption in the slow continuum. In this case, the damping is produced by an energy transfer from the global kink mode to slow mode oscillations at the boundary of the magnetic flux tube. Relaxing the zero-β approximation, the existence of slow magneto-acoustic waves cannot be discarded since the plasma in threads has chromospheric properties. This mechanism was first considered by Soler et al. (2009a) in the context of prominence threads. They derived an analytical expression for the damping ratio of the form

$$\frac{\tau_d}{P} = \frac{2}{\pi}\frac{R}{l}\left(\frac{k_z R}{1+\frac{2}{\gamma\beta}}\right)^{-2}, \tag{4.4}$$

with $k_z R$ the longitudinal wavenumber normalised to the radius of the tube, $\gamma = 5/3$ the adiabatic constant of a mono-atomic gas, and β the plasma-β parameter.

Taking the damping ratio as observable, $d = \tau_d/P$, and Eq. (4.4), we can attempt to infer the three parameters associated with damping by resonant absorption in the slow continuum, $\boldsymbol{\theta} = \{l/R, \beta, k_z R\}$. Plausible ranges of the model parameters $l/R \in [0.01, 2]$, $\beta \in [0.01, 1]$, and $k_z R \in [10^{-3}, 0.1]$ lead to theoretically predicted damping ratios in the range $\tau_d/P \sim [154, 10^{13}]$.

Figure 4.6 shows the resulting marginal posteriors associated with the three model parameters for resonant absorption in the slow continuum, with uniform prior assumptions for all parameters. All distributions can be inferred with the same tendency to peak in larger parameter values for smaller damping ratio values. In the panel (a), posterior distributions associated with the thickness of non-uniform layer peak at a similar value of l/R, regardless of the value of τ_d/P, which is a value that is similar to the l/R value for resonant absorption in the Alfvén continuum. In the panel (b), posterior distributions for the plasma-β parameter peak at small values indicating that the zero plasma-β approximation in prominence threads seems to be a good approximation. In the panel (c), posteriors have been also inferred for $k_z R$ for the three considered

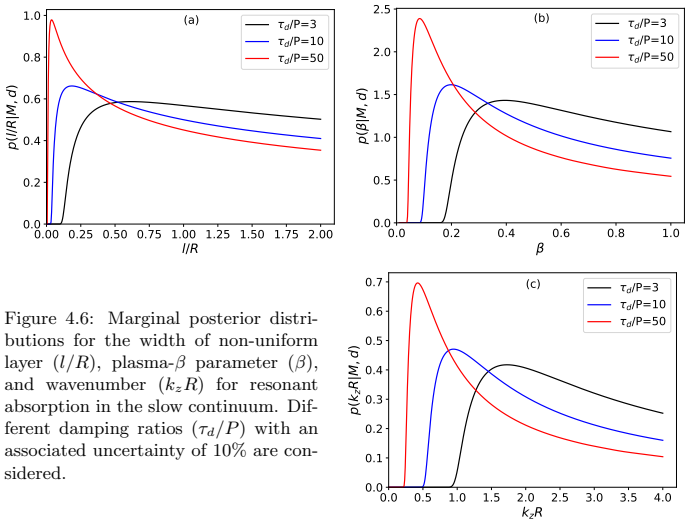

Figure 4.6: Marginal posterior distributions for the width of non-uniform layer (l/R), plasma-β parameter (β), and wavenumber ($k_z R$) for resonant absorption in the slow continuum. Different damping ratios (τ_d/P) with an associated uncertainty of 10% are considered.

damping ratios, but the range of possible wavenumber values in threads had to be extended until $k_z R = 4$, otherwise this mechanism is not able to explain those damping ratios. Much larger damping ratios need to be considered to have a proper inference with the typical reduced wavenumbers.

Instead of using the adiabatic constant of an ideal gas in Eq. (4.4), we could ask ourselves if results would change considering a more realistic adiabatic constant. Repeating the inference process with the value derived by Van Doorsselaere et al. (2011) ($\gamma = 1.10 \pm 0.02$) to define a Gaussian prior for the adiabatic index γ, we found that the posterior distributions of the model parameters do not differ significantly.

Finally, we consider the mechanism of Cowling's diffusion in partially ionised plasmas. This process consists of a magnetic diffusion in the perpendicular direction to the magnetic field lines due to ion-neutral collisions. Considering the analysis by Soler et al. (2009b,a), the theoretical expression for the damping ratio can be expressed as

$$\frac{\tau_d}{P} = \frac{\sqrt{2}}{\pi k_z R \tilde{\eta}_c}, \tag{4.5}$$

where $\tilde{\eta}_c$ is the Cowling's diffusion coefficient in dimensionless form.

As with previous damping models, we want to infer the parameters associated with this model, $\boldsymbol{\theta} = \{k_z R, \tilde{\eta}_c\}$, for different damping ratios, $d = \tau_d / P$. However, plausible values of Cowling's diffusion coefficient in prominence threads are not well known, so we first explore those plausible values in this kind of coronal structures.

To that end, we initially note that to determine the Cowling's diffusion coefficient is difficult because of its dependence on multiple unknown quantities in the form (Leake 2005)

$$\tilde{\eta}_c = \frac{\eta_c}{v_{Ap} R} \text{ where } \eta_c = \frac{B^2 \chi_n^2}{\mu_0 \alpha_n} \tag{4.6}$$

$$\text{and } \alpha_n = \frac{1}{2} \chi_n (1 - \chi_n) \frac{\rho_p^2 \Sigma_{in}}{m_n} \sqrt{\frac{16 k_B T_p}{\pi m_i}}, \tag{4.7}$$

with $\chi_n = 2 - 1/\tilde{\mu}_p$, $\tilde{\mu}_p$ the ionisation degree of the plasma, $\Sigma_{in} = 5 \times 10^{-19}$ m^{-2} the ion-neutral cross-section, m_n and m_i the neutral and ion masses, B the magnetic field strength, ρ_p, T_p, and R the density, temperature, and radius of the thread respectively. The first step we perform to simplify the analysis is to assume the prominence plasma is only constituted by neutral and ionised hydrogen, $m_n \approx m_i$. The Cowling's diffusion coefficient can then be computed

as

$$\tilde{\eta}_c = \frac{2.88 \times 10^{-8} B \chi_n}{R \sqrt{T_p \rho_p^3 (1-\chi_n)}}, \tag{4.8}$$

with all quantities in the SI. To estimate plausible limits of this parameter, we now contemplate threads with $R = 100$ km, $\rho_p = 5 \times 10^{-11}$ kg m^{-3}, $T_p = 8000$ K, $B = 5$ G, and χ_n varying according to the ionisation degree in the range $\tilde{\mu}_p \in [0.51, 0.99]$. Hence, the diffusion coefficient takes values in the range $\tilde{\eta}_c \in [10^{-4}, 0.5]^{\dagger}$ with typical wavenumbers, $k_z R \in [10^{-3}, 0.1]$, and plasma-$\beta \in [0.01, 1]$, theoretically predicted damping ratios for the Cowling's diffusion mechanism take values in the range $\tau_d/P \sim (30 - 10^7)$, which points to this mechanism being unable to provide the observed damping timescales.

In spite of this, we performed the inference of the two relevant parameters, $k_z R$ and $\tilde{\eta}_c$, for three different damping ratio values. The resulting posteriors are shown in Fig. 4.7. Uniform priors have been considered. Posterior distributions can be inferred with posteriors corresponding to wavenumbers peaking at larger values for smaller damping ratios. For the inference of the Cowling's coefficient, we had to extend the range of considered values up to $\tilde{\eta}_c = 4$ to obtain posterior distributions corresponding to small damping ratios. Typical values of the diffusion coefficient seem to be adequate for damping ratios of about tens.

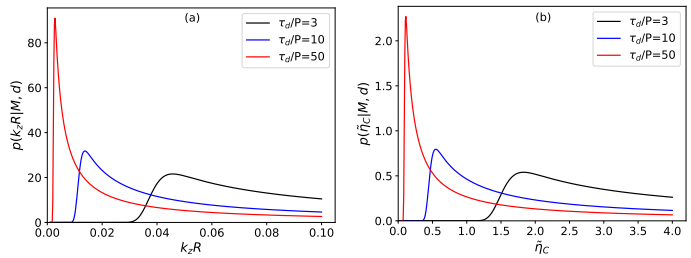

Figure 4.7: Marginal posterior distributions for wavenumber ($k_z R$) and Cowling's coefficient ($\tilde{\eta}_c$) for Cowling's diffusion. Three different damping ratios (τ_d/P) with associated uncertainty of 10% are considered.

†The expression 4.8 is valid for solar atmospheric layers if they are assumed to be conformed in their majority by hydrogen plasma. For typical conditions in the photosphere (T=5000 K, $\rho \sim 10^{-4}$ kg m^{-3}), the chromosphere (T=8000 K, $\rho \sim 10^{-8}$ kg m^{-3}), and the corona (T=10^6 K, $\rho \sim 10^{-12}$ kg m^{-3}), resulting Cowling's diffusion coefficient are $\tilde{\eta}_c^{\rm phot} \in [8 \times 10^{-14}, 2 \times 10^{-10}]$, $\tilde{\eta}_c^{\rm chrom} \in [7 \times 10^{-8}, 2 \times 10^{-4}]$, and $\tilde{\eta}_c^{\rm cor} \in [6 \times 10^{-3}, 14]$ respectively, by considering the same radius and magnetic field strength.

Plots considering different uncertainties are not included in this case but the tendency is the same as in the previous chapter in the context of coronal loops i.e., the larger the uncertainty is, the wider the posterior distributions are.

Model Comparison

The causative mechanism of damping of transverse oscillations not only remains unknown for coronal loops, but also for prominence threads. A simple evaluation of the capacity of each damping mechanism to reproduce observed damping ratios can be obtained by inserting typical values for the model parameters in Eqs. (4.3), (4.4), and (4.5). The ranges so obtained and previously discussed in Section 4.2.1 point towards the Alfvén resonance as the most plausible mechanism. However, one must be aware that those so-called typical values are highly uncertain and cannot be measured directly. Therefore, different combinations of typical values would lead to different predictions of τ_d/P for each model, which could have a large variability.

We first use the marginal likelihood, as defined in Eq. (2.3), to calculate the likelihood of a given model to reproduce a given observed damping ratio, considering how different combinations of model parameters contribute to theoretical predictions that are close to observed data. In our case, we considered a 10 % uncertainty on the observable, $d = \tau_d/P$. Uniform and independent priors for all parameters of the damping models have been contemplated. The values for these parameters are enclosed in the same plausible ranges for prominence conditions used in the inference analysis.

Figure 4.8 shows marginal likelihoods corresponding to each damping mechanism, as a function of the observable damping ratio. Resonant absorption in the Alfvén continuum (Fig. 4.8a) has the largest plausibility for very strong damping regimes, which have values of τ_d/P even below 1. The marginal likelihood for resonant absorption in the slow continuum (Fig. 4.8b) spreads over much larger damping ratio values, peaking at a damping ratio around 470. Finally, the marginal likelihood for Cowling's diffusion (Fig. 4.8c) is more compatible with observed damping ratios in the range $5 \times 10^6 - 5 \times 10^7$. Hence, each mechanism seems to explain better different ranges of τ_d/P, but only the Alfvén resonant absorption shows a marginal likelihood that has its largest values for damping ratios compatible with those observed.

To assess the relative plausibility between models, Bayes factors using Eq. (2.7) must be computed. This is done in a one-to one comparison between the three mechanisms. Figure 4.9 shows Bayes factors, B_{ij}, as a function of the observable damping ratio, with the subscripts $ij \in [0, 1, 2]$ corresponding

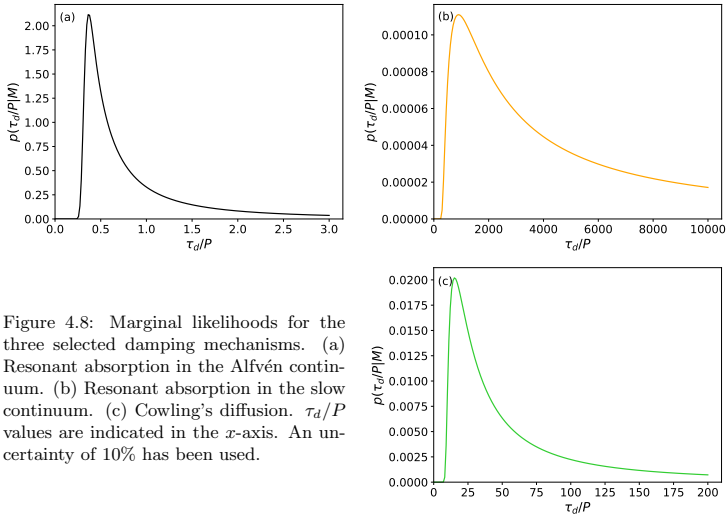

Figure 4.8: Marginal likelihoods for the three selected damping mechanisms. (a) Resonant absorption in the Alfvén continuum. (b) Resonant absorption in the slow continuum. (c) Cowling's diffusion. τ_d/P values are indicated in the x-axis. An uncertainty of 10% has been used.

to resonant absorption in the Alfvén continuum, resonant absorption in the slow continuum, and Cowling's diffusion respectively. Hence, when confronted to the other alternatives, resonant absorption in the Alfvén continuum is the only mechanism for which Bayes factors showing strong evidence is obtained in the region of typically observed damping ratios of the order of units.

In the comparison between resonant absorption in the Alfvén continuum and resonant absorption in the slow continuum (Fig. 4.9a), we find strong evidence in favour of the first model for damping ratios up to 125, in which Bayes factor reach values up to 100 (the figure was cut in the vertical direction for clarity). In the rest of the interval, resonant absorption in the slow continuum dominates with very strong evidence. In the comparison between resonant absorption in the Alfvén continuum and Cowling's diffusion (Fig. 4.9b), we find strong evidence in favour of resonant absorption for the lowest values of damping ratio ($\tau_d/P < 9$), intermediate values do not show enough evidence to support any of the two models and the rest of values ($\tau_d/P > 13$) are better explained by Cowling's diffusion. Finally, in the comparison between resonant absorption in the slow continuum and Cowling's diffusion (Fig. 4.9c), we find very strong evidence in favour of Cowling's diffusion for all damping ratios below $\tau_d/P \sim 200$. For the remaining damping ratio values, the evidence is not

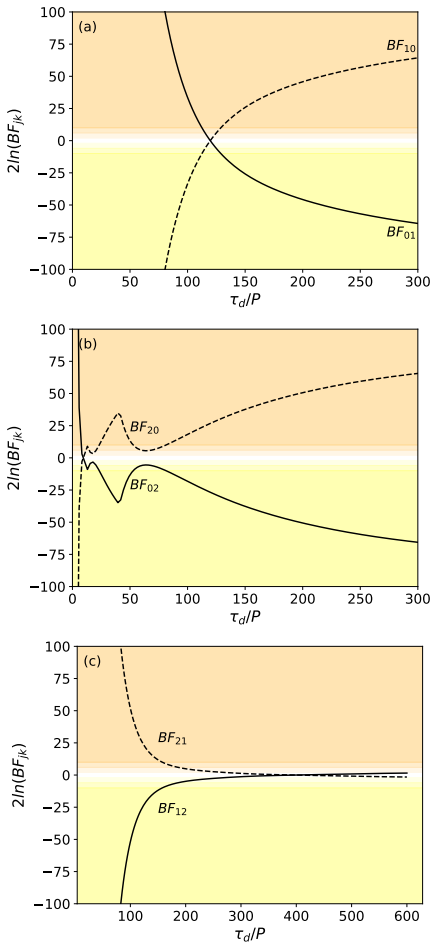

Figure 4.9: Bayes factors as a function of the damping ratio (τ_d/P) with an associated uncertainty of 10%. Subscripts 0, 1, and 2 correspond to resonant absorption in the Alfvén continuum, resonant absorption to the slow continuum, and Cowling's diffusion respectively.

strong enough to support any of these two models.

Soler et al. (2009a) already found that the damping time due to resonant absorption in the Alfvén continuum is much shorter than that corresponding to resonant absorption in the slow continua. In a situation with both, the former would damp the oscillations much earlier. In this Bayesian context, the computation of marginal likelihoods has to be done separately and gives a measure of how many times different combination of parameters would lead to a given observable.

4.2.2 Partially Filled Inhomogeneous Tubes

The partially filled tube model tries to mimic observed prominence threads, so that the infinite tubes considered in the previous analysis do not seem to adjust to the reality. Hence, we assume now the same damping mechanisms but in a partially filled tube. All the analytical expressions for the damping ratios were derived by Soler (2010)[‡]. The equation for the damping ratio of resonant absorption in the Alfvén continuum remains the same since it does not depend on the longitudinal direction, but damping ratios corresponding to resonant absorption in the slow continuum and Cowling's diffusion need to be modified by replacing the wavenumber $k_z R$ to include the factor $2/\sqrt{(L_p/L(1-L_p/L))}$. Eqs. (4.4) and (4.5) become

$$\frac{\tau_d}{P} = \frac{R}{l}\frac{L_p/L(1-L_p/L)\left(1+2/\gamma\beta\right)^2}{2\pi} \tag{4.9}$$

for resonant absorption in the slow continuum and

$$\frac{\tau_d}{P} = \frac{\sqrt{L_p/L(1-L_p/L)}}{\sqrt{2}\pi\tilde{\eta}_c}, \tag{4.10}$$

for Cowling's diffusion.

Repeating the inference analysis with these expressions for the damping ratios, we first obtain the posterior distributions of model parameters, $\boldsymbol{\theta}_{\rm RASC} = \{l/R, \beta, L_p/L\}$ and $\boldsymbol{\theta}_{\rm CD} = \{\tilde{\eta}_c, L_p/L\}$. Figure 4.10 shows the posterior distributions corresponding to resonant absorption in the slow continuum. The range of plausible values for the thread length is $L_p/L \in [0.001, 1]$ and the rest of parameter ranges remain equal to those considered in the analysis for the infinite tube, as well as the assumption of uniform priors. Distributions by considering infinitely long tubes have been also included for comparison. In

[‡]The expression for resonant absorption in the slow continuum (Eq. 4.9) is not presented in Soler (2010), but it can be derived following a procedure described in his thesis.

both partially and totally filled tubes, posterior distributions show the same tendency, but those corresponding to a partially filled tube have smaller probabilistic amplitudes. Regarding the relation between the length of the thread and the total length, its associated posterior distribution is not well inferred since at the largest values of the parameters it shows a high tail. However, for the smallest ones up to 0.2 approximately, the probability is zero, so that the smallest threads do not support transverse waves which damp in 3 periods by resonant absorption in the slow continuum.

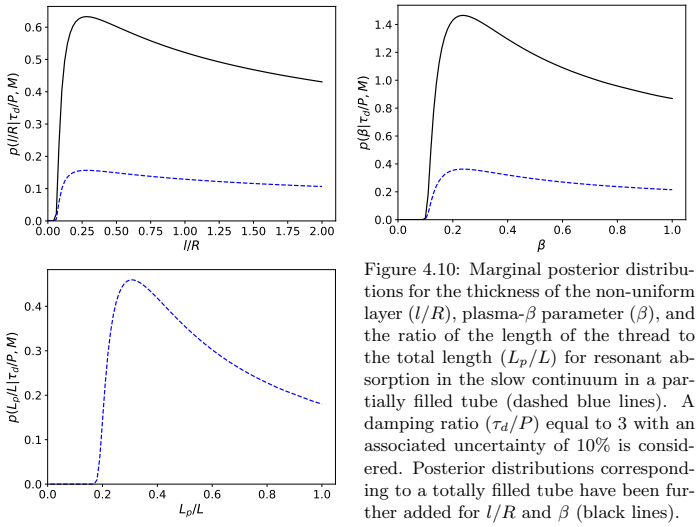

Figure 4.10: Marginal posterior distributions for the thickness of the non-uniform layer (l/R), plasma-β parameter (β), and the ratio of the length of the thread to the total length (L_p/L) for resonant absorption in the slow continuum in a partially filled tube (dashed blue lines). A damping ratio (τ_d/P) equal to 3 with an associated uncertainty of 10% is considered. Posterior distributions corresponding to a totally filled tube have been further added for l/R and β (black lines).

Moving to Cowling's diffusion, Fig. 4.11 shows the corresponding posterior distributions for a partially filled tube. It is appreciable that the Cowling's diffusion coefficient (left panel) is much smaller than in a totally filled tube, so that we have not to extend the plausible range of this parameter to larger values. In fact, the posterior is well constrained from about 0.005 to 0.06, peaking at around 0.035. Unfortunately, the posterior distribution for the length of the threads cannot be well inferred, and any information can be extracted about the plausibility for different values.

Continuing with the comparison between damping mechanisms in inhomogeneous tubes, we computed the marginal likelihood associated with each damping mechanism and Bayes factors in the one-by-one comparison. Fig-

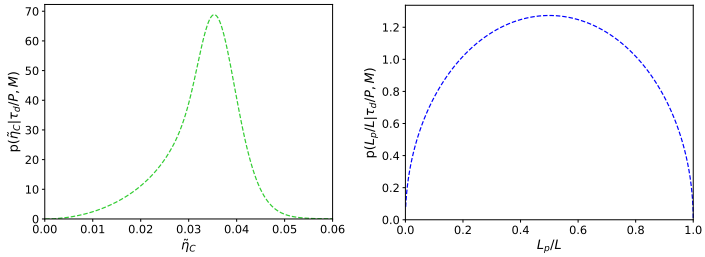

Figure 4.11: Marginal posterior distributions for Cowling's coefficient ($\tilde{\eta}_c$) and the ratio of the length of the thread to the total length (L_p/L) for Cowling's diffusion in a partially filled tube. A damping ratio (τ_d/P) equal to 3 with associated uncertainty of 10% is considered.

ure 4.12 displays the marginal likelihoods for resonant absorption in the slow continuum and Cowling's diffusion in the considered scenario (marginal likelihood of resonant absorption in the Alfvén continuum was already presented in panel a of Fig. 4.8). In both cases, the damping ratios are several orders of magnitude smaller than those obtained for an infinitely long tube. While plausible damping ratios for an infinite tube were of thousands by considering resonant absorption in the slow continuum, in a partially tube they do not extend up to the unity. Regarding Cowling's diffusion, instead of obtaining damping ratios of dozens in a infinite tube, damping ratios around decimals up to one seem to be more plausible in partially filled tubes. Hence, under prominence threads conditions, resonant absorption in the Alfvén continuum

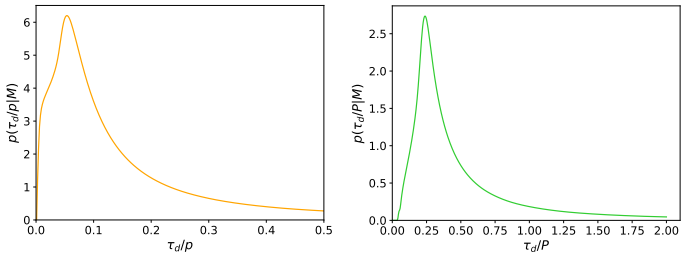

Figure 4.12: Marginal likelihoods for resonant absorption in the slow continuum (left) and Cowling's diffusion (right) when a partially filled tube is considered. τ_d/P values are indicated in the x-axis. An uncertainty of 10% has been used.

and Cowling's diffusion could explain small damping ratios up to 2 or 3 approximately. In contrast, larger values are not in agreement with any of the considered damping models.

To accomplish how many times one mechanism is more plausible than another, we compute Bayes factors. Figure 4.13 shows the results of these computations, where subscripts 0, 1, and 2 refer to resonant absorption in the Alfvén continuum, resonant absorption in the slow continuum, and Cowling's diffusion, respectively. In the comparison between both resonance models (panel a), we observe that the strongest damping regime is better explained by resonant absorption in the slow continuum. Then, positive evidence in favour of resonant absorption in the Alfvén continuum is obtained for values of the damping ratio up to 8, damping ratios around 9 do not show enough evidence to support any resonance model and a positive evidence in favour of resonant absorption in the slow continuum is obtained in between 9 and 10. Comparing resonant absorption in the Alfvén continuum with Cowling's diffusion (panel b), Cowling's diffusion evidence dominates in front of that corresponding to resonant absorption in the Alfvén continum. For intermediate values of the damping ratio up to 6 approximately, evidence is not worth a bare mention. Then, for damping ratios around 7 positive evidence supports resonant absorption in the Alfvén continuum as the most plausible mechanism and values around 10 are more likely for Cowling's diffusion. Confronting resonant absorption in the slow continuum with Cowling's diffusion (panel c), damping ratios close to zero show strong evidence in favour of resonant absorption in the slow continuum but for the rest of damping ratios, the evidence is not strong enough to support any of these two mechanisms except for values around 5 or 10 with slight positive evidence for Cowling's diffusion mechanism.

4.3 Lengths and Densities of Prominence Threads

One of the main difficulties with prominence thread seismology in comparison to coronal loop seismology is that threads occupy only part of a longer magnetic flux tube whose total length cannot be directly measured. Hence, the ratio of the length of the thread to the length of the tube, L_p/L, is a relevant parameter upon which periods and damping times of transverse thread oscillations depend (Soler et al. 2010; Arregui et al. 2011).

It was first suggested by Díaz et al. (2010) that the ratio of the period of the fundamental transverse kink mode to twice that of the first overtone period can be used as a tool for prominence seismology. Their analysis was based on the configuration by Díaz et al. (2002) in which the thread consists of cool material with density ρ_p occupying a length L_p embedded in a longer flux tube of length

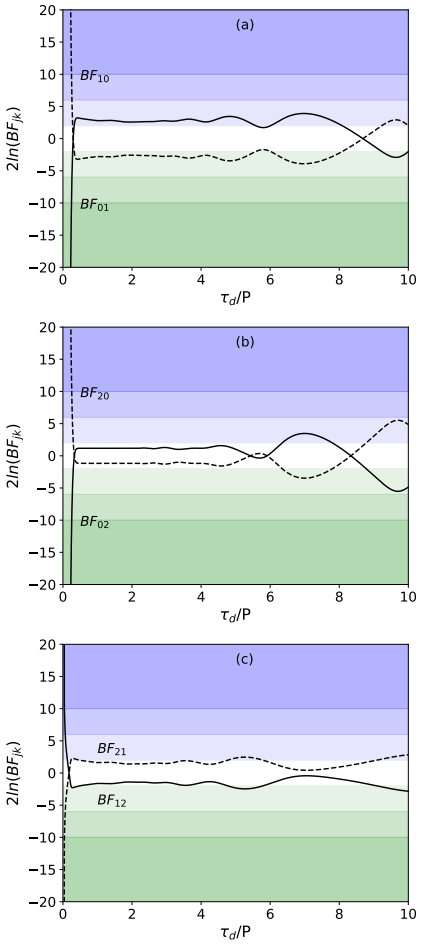

Figure 4.13: Bayes factors as a function of the damping ratio (τ_d/P) with an associated uncertainty of 10%. Subscripts 0, 1, and 2 correspond to resonant absorption in the Alfvén continuum, resonant absorption to the slow continuum, and Cowling's diffusion respectively. Partially filled tubes have been considered.

L with coronal density ρ_c. In the low frequency limit ($\omega L/v_{Ap} << \pi/2$), the period ratio can be cast as a function of the density contrast, ρ_p/ρ_c, and the length of the thread in units of the total length, L_p/L, as

$$\frac{P_1}{2P_2} \approx \frac{1}{2\sqrt{L_p/L}}\sqrt{\frac{1+L_p/L(3f^2-1)}{1+L_p/L(f^2-1)}}, \tag{4.11}$$

where $f=\sqrt{(\rho_p/\rho_c+1)/2}$. If we further assume that $\rho_p/\rho_c >> 1$, the period ratio can be approximated as

$$\frac{P_1}{2P_2} \approx \sqrt{\frac{3}{4L_p/L}}. \tag{4.12}$$

As shown by Díaz et al. (2010), the fundamental mode satisfies the condition of low frequency in Eq. (4.12) but the first overtone does not. For this reason, Díaz et al. (2010) considered the next term in their frequency series expansion, obtaining the following expression for the period ratio

$$\frac{P_1}{2P_2} \approx \sqrt{\frac{3}{4L_p/L}}\sqrt{\frac{1+\sqrt{(1+L_p/3L)/(1-L_p/L)}}{1+\sqrt{(9/5-L_p/L)/(1-L_p/L)}}}. \tag{4.13}$$

For our Bayesian inversion we consider the period ratio, $d = P_1/2P_2$ as observable and Eqs. (4.12) and (4.13) as theoretical predictions. Then, the inference of the proportion of the total length occupied by the thread, L_p/L, can be attempted. A uniform prior is applied to this analysis for $L_p/L \in (0,1)$. For this range, Eq. (4.13) predicts period ratios in between 0.9 and ∞.

Figure 4.14 shows the inferred marginal posterior distributions of L_p/L for four values of the observable period ratio and using both approximations given by Eqs. (4.12) and (4.13). The larger the period ratio is, the shorter the inferred values of L_p/L are. When comparing the results using both approximations, we find that posterior distributions obtained from Eq. (4.13) peak at slightly smaller values of the period ratio than those acquired by using the most simple equation. This means that including one more term in the series expansion of the direct problem affects the inferred value of the length of the thread. Regarding real observations, Lin et al. (2007) reported a possible detection of multiple harmonic oscillations, which have a period ratio $P_1/2P_2 \sim 2.22$. Although the reliability of this observation is questionable, seismology applications based on this event have been presented by Soler & Terradas (2015) and Arregui & Soler (2015). If we believe in the reliability of the observational estimate, this leads to an inferred value of $L_p/L = 0.16 \pm 0.03$, when an uncertainty of 10% in the period ratio is considered.

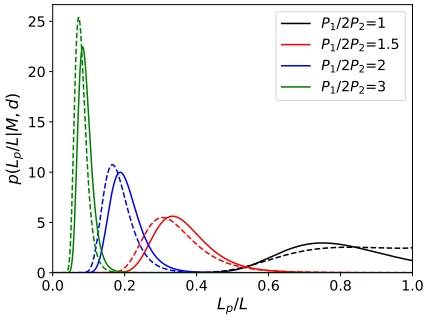

Figure 4.14: Posterior distributions of proportion of thread (L_p/L) considering Eq. (4.12) (continuous line) and Eq. (4.13) (dashed line), in the short frequency limit. Observable values of $P_1/2P_2$ with an associated uncertainty of 10% have been considered.

In addition to the limitation that Eqs. (4.12) and (4.13) are only valid in the low frequency limit, they are not very good approximations to the period ratio for short threads (see Figure 3 of Díaz et al. 2010). For the short thread limit, Díaz et al. (2010) derived an expression for the period ratio of the form

$$\frac{P_1}{2P_2} \approx 1 + (f^2 - 2)\frac{L}{L_p} - (f^2 + 1)\left(\frac{L}{L_p}\right)^2 . \tag{4.14}$$

Using the same inference procedure as before, we now use Eq. (4.14) to infer the two parameters $\boldsymbol{\theta} = \{L_p/L, \rho_p/\rho_c\}$ from the observable period ratio. Uniform priors are used for the length of the thread in the range of $L_p/L \in [0, 1]$ as a first approximation to sample all plausible values and for the density contrast $\rho_p/\rho_c \in [1.01, 300]$ to account for the large density contrast typical of prominence plasmas. Figure 4.15a and b show the resulting posterior probabilities for both parameters, L_p/L and ρ_p/ρ_c. For all considered period ratios, both the density contrast and the length of the thread can be properly inferred. Figure 4.15a, corresponding to the length of thread, shows two clearly visible peaks for each distribution with small differences between them for different period ratio values. Small values of the theoretical period ratio are compatible with large lengths of the thread and small density contrasts but also with small lengths of the thread and large density contrasts because of the negative sign of the last term in Eq. (4.14). The distributions for the density contrast in Fig. 4.15b peak at small values of the parameter and spread to larger values for larger period ratio values. In the considered range for this parameter, the

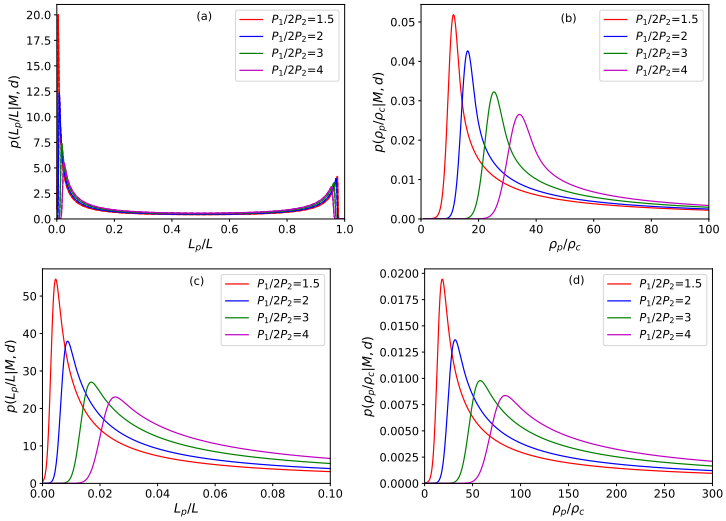

Figure 4.15: Posterior distributions of the thread length (L_p/L) and the density contrast (ρ_p/ρ_c) for several values of the period ratio ($P_1/2P_2$) with an associated uncertainty of 10%. Top panels correspond to using Eq. (4.14) with $L_p/L \in [0, 1]$ and $\rho_p/\rho_c \in [1.1, 100]$. Bottom panels show results of considering short thread limit using the same equation as top panels with $L_p/L \in [0, 0.1]$ and $\rho_p/\rho_c \in [1.1, 300]$.

secondary peak is not visible.

Note that Eq. (4.14) is only strictly valid in the short thread limit. If we constrain the possible values of L_p/L to the shorter range $L_p/L \in [0, 0.1]$, we obtain the results shown in Figs. 4.15c and d. In contrast to the tendency found for the marginal posteriors for L_p/L in the long thread approximation, the posteriors in Fig. 4.15c move towards larger values of L_p/L for larger period ratio values. A similar behaviour is obtained for the posterior distributions of density contrast which peak at larger values in comparison to those obtained considering the full range in L_p/L in the previous case. Also, a very small probability is obtained for density contrasts above 200, unless we consider wider ranges of ρ_p/ρ_c with values from tens to thousands.

To analyse possible the differences between the several equations employed in this section, i.e. Eqs. (4.11), (4.12), (4.13), and (4.14), we compute the posterior of the length of the thread proportion for all the plausible range of the

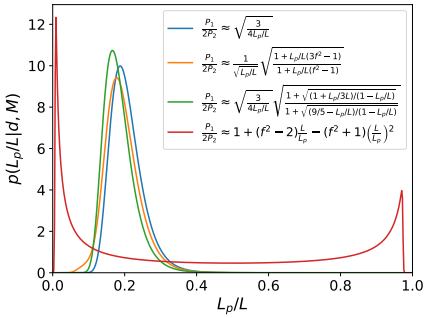

Figure 4.16: Comparison of posterior distributions of the thread length proportion (L_p/L) obtained for Eqs. (4.11), (4.12), (4.13), and (4.14). One observable period ratio of $P_1/2P_2 = 2$ has been considered with an associated uncertainty of 10%.

parameter in all cases with an observable period ratio equal to $P_1/2P_2 = 2\pm0.2$. Figure 4.16 shows posterior distributions resulting from this analysis. In the long thread approximation, distributions obtained from considering different equations do not differ. However, the result differs when we consider the equation for the short thread approximation. The posterior distribution has one peak in a value next to zero differing from the other distributions. In addition, it shows a secondary peak with smaller amplitude at the opposite side of the parameter range, next to 1, due to the sign of the last term in the Eq. (4.14).

4.3.1 Comparison between Short and Long Thread Limits

As the length of the full magnetic tube is difficult to estimate, we wish to ascertain how plausible each approximation is for a given observationally estimated period ratio. To do so, we consider Eqs. (4.13) and (4.14) and compute the marginal likelihood associated to each approximation. We also compare them through the use of Bayes factors. The ranges of plausible values for the parameters, $\boldsymbol{\theta} = \{L_p/L, \rho_p/\rho_c\}$, are the same as in the inference analysis. Uniform priors have been assumed for these parameters and values of the period ratio, $P_1/2P_2$, from 0 to 5 are taken with an uncertainty of 10%.

Figure 4.17a shows the obtained marginal likelihoods. We can appreciate that values of $P_1/2P_2$ smaller than 1 are very unlikely under the considered models. For the long thread approximation, the marginal likelihood peaks around period ratios in between 1 and 2.5 approximately, and probabilities are

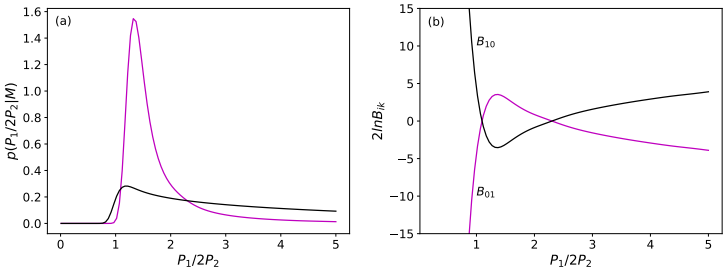

Figure 4.17: (a) Marginal likelihoods for long (magenta line) and short (black line) thread limits. $P_1/2P_2 \in (0, 5]$ with associated uncertainties of 10%. (b) Bayes factors as a function of the ratio of the fundamental kink mode period to twice the first overtone period. An uncertainty of 10% has been assumed. The subscripts 0 and 1 correspond to long and short thread limits respectively.

3 times higher than those for the short thread limit. For larger values of the period ratio, the short thread approximation seems to be more probable.

Regarding Bayes factors, the results are shown in Fig. 4.17b. Very strong evidence in favour of the short thread model is obtained when $P_1/2P_2$ values are below 1, positive evidence in favour of the long thread model for intermediate values of the period ratio, and positive evidence for the short thread limit for even larger period ratio values.

Therefore, in partially filled tubes, values of the period ratio in between 1 and 2.5 are better explained by the long thread approximation, while the short thread approximation provides greater evidence for period ratio values below and above that range. This model comparison analysis enables us to quantify the goodness of the inference results under a given period ratio approximation for a given period ratio measurement, with its corresponding observational error.

4.4 Length of Flowing and Oscillating Threads

Prominence threads are observed to flow at the same time that they support transverse oscillations (Okamoto et al. 2007; Okamoto et al. 2015). Some theoretical models have considered the properties of transverse waves in non-static equilibria and the influence of mass flows in their oscillatory features (Dymova & Ruderman 2005), with first applications to Hinode observations (Terradas et al. 2008).

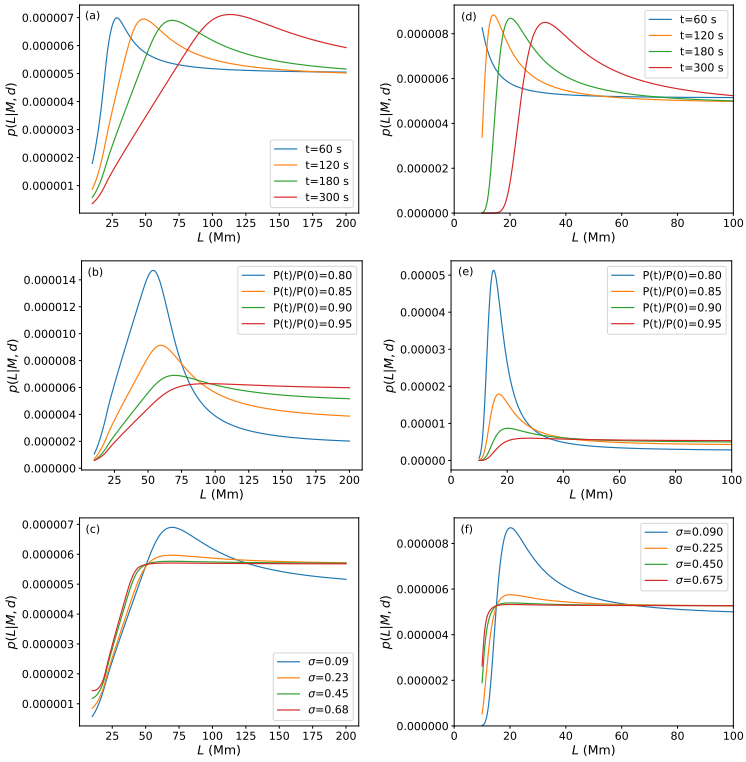

Figure 4.18: Posterior distributions of the total length of the flux tube (L) with uniform (left panels) and Gaussian (right panels) priors. Gaussian priors are centred in $v_0 = 22$ km s^{-1} and $L_p = 4$ Mm with an uncertainty of 10%. The first row shows results of considering multiple observation times with $P(t)/P(0) = 0.9$ and an associated uncertainty of 10%. The second row shows results of considering multiple period ratios with $t = 180$ s and 10% as uncertainty for all observables. The third row conforms results associated with different uncertainties, $\sigma = 10, 25, 50, 75\%$, with $P(t)/P(0) = 0.9$ and $t = 180$ s.

To perform our analysis, we consider again the partially filled tube model based on Díaz et al. (2002) but the thread is permitted to flow along the magnetic field direction. In this scenario, the inclusion of a flowing thread with velocity v_0 produces the period of the fundamental kink mode to vary in time. Soler & Goossens (2011) analysed the temporal evolution of the period and gave an analytical expression for the ratio of the period at any time, t, to the period at time $t = 0$, of the form

$$\frac{P(t)}{P(0)} = \sqrt{1 - \frac{4v_0^2 t^2}{(L + \frac{1}{3}L_p)(L - L_p)}}. \tag{4.15}$$

This expression depends on three physical quantities, the flow velocity, v_0, the length of the thread, L_p, and the total length of the flux tube, L.

Considering the theoretical prediction given by Eq. (4.15), we first compute the posterior distribution for each model parameter $\boldsymbol{\theta} = \{L, v_0, L_p\}$ assuming a time of observation equal to 180 s and an observable $d = P(t = 180 \text{ s})/P(0) = 0.9$, where the associated uncertainty is 10%. The possible values of parameters inside the square root are limited by mathematical reasons since the second term should be less than 1, so that the considered ranges of parameters are $v_0 \in [0.01, 100]$ km s^{-1}, $L_p \in [0.01, 20]$ Mm, and $L \in [10, 200]$ Mm, but not all combinations of these values will be possible. Uniform priors have been assumed for the three quantities in the first scenario and Gaussian priors for the flux velocity and length of the thread in a second scenario.

The resulting posterior distributions for the total length of the flux tube are presented in Fig. 4.18 for the two scenarios. Different values of observation times, period ratios, and uncertainties are studied. The flow velocity and the thread length cannot be properly inferred and they are omitted for clarity. In general, the distributions are not well constrained, showing long tails for large values of the parameter but more defined distributions are obtained when Gaussian priors are assumed. Panels (a) and (d) show posteriors of L for different times of observations. Larger values of L are more plausible for larger times. A lower limit of L could be inferred in the second scenario. Panels (b) and (e) present posterior distributions for various period ratio values. Smaller values of L are more likely and more defined distributions are obtained with smaller period ratio values. Regarding the influence of considering different uncertainties in measurements, panels (c) and (f) show that posterior distributions for the total length of the flux tube do not change significantly except for the smallest value of the uncertainty. The length of the flux tube cannot be well inferred, unless the uncertainty associated with the period ratio measurement is very small.

After analysing the general case, we focus on applying the same model to particular real observations reported by Okamoto et al. (2007). These authors report on the simultaneous presence of flowing and transversally oscillating threads observed with Hinode. Although period variations in time were not reported, we assume hypothetical period changes to exemplify a possible application to infer the total length of the flux tube from this kind of observations. Table 4.2 gives a summary of the thread lengths and flow velocities reported by Okamoto et al. (2007). In our inference, the observable and its uncertainty remain the same as in the previous scenario but Gaussian priors are used for the length of the thread and the flow velocity, where Gaussians are centred at those values measured by Okamoto et al. (2007). Uncertainties are not given in their work, so that we have considered uncertainties of 10% for all measurements. Regarding the total length of the flux tube, a uniform prior is assumed.

Results for the inferred distributions and summary values of median with errors for the total length for all six threads are shown in Fig. 4.19 and Table 4.2, third column. The total length of the flux tube cannot be properly inferred because the posterior distributions show long and high tails at the right-hand side of the distributions. However, all six distributions show a common tendency to peak at values of the length in between approximately 20 Mm and 40 Mm. Analysing the median values in Table 4.2, the total length takes values roughly in between 20 and 90 Mm within the errors, being this last value next to values reported in some previous studies which fixed a minimum value of 100 Mm (Soler et al. 2010; Terradas et al. 2008). Hence, L_p represents less than 10% of the total flux tube.

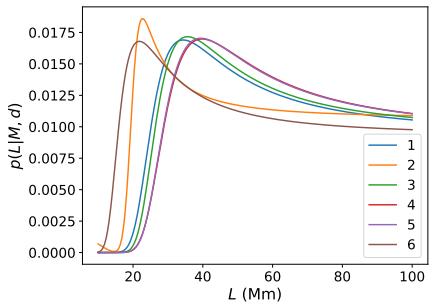

Figure 4.19: Posterior distributions of the total length of threads analysed by Okamoto et al. (2007). An observation time of $t = 180$ s and a ratio of 0.9 have been assumed with an associated uncertainty of 10%.

Thread #	L_p (Mm)	v_0 (km s^{-1})	L (Mm)
1	3.6	39	57^{+28}_{-23}
2	16	15	55^{+31}_{-27}
3	6.7	39	58^{+28}_{-22}
4	2.2	46	59^{+27}_{-21}
5	3.5	45	59^{+27}_{-21}
6	1.7	25	52^{+33}_{-26}

Table 4.2: Threads data analysed by Okamoto et al. (2007). Columns contain the number of thread (#), the observed thread length (L_p), the measured velocity of flow (v_0), and the median values of posterior distributions of the total length of the flux tube (L) with a credible interval of 68%.

Slow Flows

Looking at the result presented by Soler & Goossens (2011), we can note a great difference between their estimation of the total length of the flux tube of about 160 Mm ($P(t)/P(0) = 0.9$, $v_0 = 40$ km s^{-1}, $L_p = 10$ Mm, and $t = 300$ s) and our results in Table 4.2. Taking into consideration that flows in threads are slow, Soler & Goossens (2011) derived the expression

$$L \approx L_p + \frac{v_0^2 t^2}{L_p} \frac{3}{1 - \left(\frac{P(t)}{P(0)}\right)^2} \tag{4.16}$$

for the total length of the flux tube, with a typo corrected (their estimated total length would change to 237 Mm). Solving the temporal evolution of the period, Eq. (4.15) transforms into

$$\frac{P(t)}{P(0)} \approx \sqrt{1 - \frac{3v_0^2 t^2}{L_p(L - L_p)}} \tag{4.17}$$

for slow flows. To determine the effect of such a consideration, we first take the direct problem. Figure 4.20a shows the temporal period as a function of time by considering the general expression (red line) and the equation for slow flows (magenta line), when $v_0 = 40$ km s^{-1}, $L_p = 10$ Mm, and $L = 237$ Mm. The dashed black lines indicate $P(t)/P(0) = 0.9$ and $t = 300$ s. Results from both equations differ with increasing deviation for larger times. In fact, the considered conditions are only possible for slow flows.

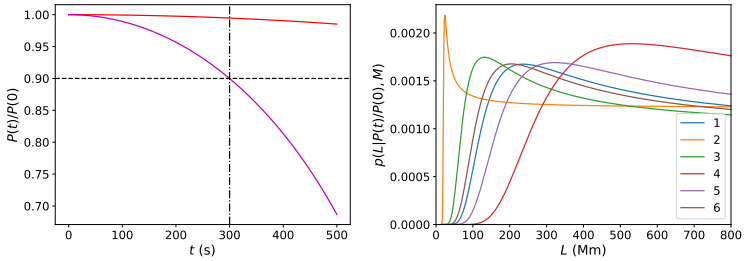

Figure 4.20: (a) Temporal evolution of the period applying Eqs. (4.15) and (4.17) to considered data by Soler & Goossens (2011). (b) Results of applying Bayesian methods to the observed threads by Okamoto et al. (2007) when flows are considered slow..

On the other hand, we repeat the inference analysis for the observations by Okamoto et al. (2007) but considering Eq. (4.17) instead. Figure 4.20b shows the resulting posterior distribution for the total length of each considered thread. We can appreciate that posterior distributions have shifted towards much larger values of the total length. Hence, results of total flux tube lengths are over-estimated by considering slow flows.

4.5 Propagating Waves

Thanks to observations (Tomczyk et al. 2007; Tomczyk & McIntosh 2009; Okamoto et al. 2007; Lin et al. 2007, 2009), it has been possible to discern fast propagating waves not only in coronal loops, but also in the whole corona including prominence threads, with similar spatial damping scales. Hence, studies of propagating waves have been normally performed by considering a wave-guide, in principle applicable to any coronal structure. In this context, assumptions and expressions used within Chapter 3 for resonant absorption of propagating waves are valid for prominence threads.

Taking advantage of this, we take large density contrasts typical of prominence threads, so that Eqs. (3.7) and (3.8) can be expressed as

$$\frac{L_d}{\lambda} = \left(\frac{2}{\pi}\right)^2 \frac{R}{l} \tag{4.18}$$

for an exponential decay or

$$\frac{L_g}{\lambda} = \frac{2}{\pi}\left(\frac{R}{l}\right)^{1/2} \tag{4.19}$$

for a Gaussian one. Both expressions are sole functions of one parameter, the thickness of the non-uniform layer, $\boldsymbol{\theta}_{d,g} = \{l/R\}$.

Applying the same Bayesian methods developed for coronal loops, we infer the model parameter for the exponential and Gaussian decays by assuming a uniform prior in the range $l/R \in [0.01, 2]$ and an observable of $L/\lambda = 3$ (remember that L here is the damping length, not the length of prominence threads). Figure 4.21 shows results from these computations. Smaller values of the radial inhomogeneity scale are obtained for a Gaussian decay, with posterior distributions peaking at 0.05 while for an exponential decay, the posterior peaks at around 0.014. These results are in agreement with the outcomes for propagating coronal loops oscillations. Nonetheless, in the case of prominence threads, the distributions are shifted to half the values obtained for coronal loops.

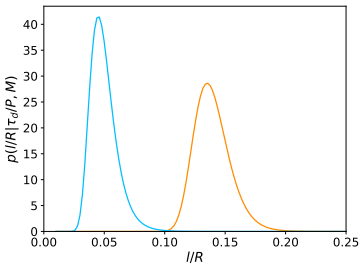

Figure 4.21: Posterior distribution of the thickness of the non-uniform layer under the assumption of an exponential (orange line) or a Gaussian (blue line) decay of propagating oscillations by resonant absorption in prominence threads. An spatial damping ratio of $L_d/\lambda = L_g/\lambda = 3$ has been fixed with an associated uncertainty of 10%.

Moving to the comparison of both profiles, we compute the marginal likelihood associated to each one and present our results in Fig. 4.22a. Smaller values of the spatial scale are more likely for an exponential decay than for a Gaussian one. Bayes factors as a function of the observable can be seen in Fig. 4.22b. Clearly, for the selected conditions, an exponential damping explains better the smallest and largest values of the ratio between the damping length and the wavelength. Gaussian decay is only adequate for some values around 0.5 to 0.75 with positive evidence. Intermediate values in between 0.75 and 6 corresponding to real observations are not supported by any of these two profiles.

Finally, we have split the previous observable into its two components and we have computed the Bayes factors corresponding to each point in the plane of observables, $d = \{L, \lambda\}$. The results are presented in Figure 4.23 with colours indicating the levels of evidence according to the criteria by Kass & Raftery (1995) in Table 2.2. Evidences depend on the particular pair of values

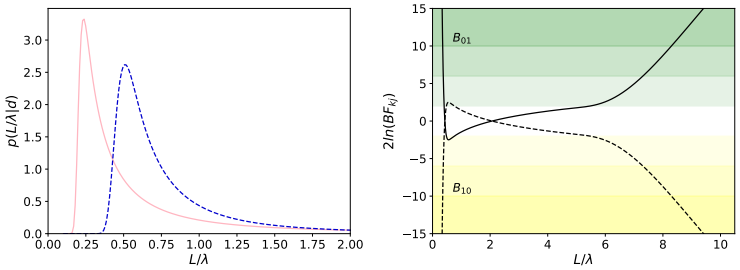

Figure 4.22: (a) Marginal likelihoods for exponential (pink continuous line) and Gaussian (cyan dashed line) decays by resonant absorption in prominence threads. The observable values have been taken in the interval $L/\lambda \in [0.01, 10]$ with an associated uncertainty of 10%. Here, L/λ-axis goes up to 2 for clarity. (b) Bayes factors for the comparison between exponential and Gaussian decays, here represented with the subscripts 0 and 1 respectively. Values in the range $L/\lambda \in [0.01, 10]$ have been considered with an uncertainty of 10%. Colours indicate levels of evidence in Table 2.2.

that we select i.e., they depends on each observable. If we look at results for coronal loops in Fig. 3.29, we see that the results for prominence threads differ. While almost all the plane of observables for coronal loops does not show evidence strong enough in favour of neither exponential nor Gaussian decays, different evidences are found for prominences threads depending on the selected observable.

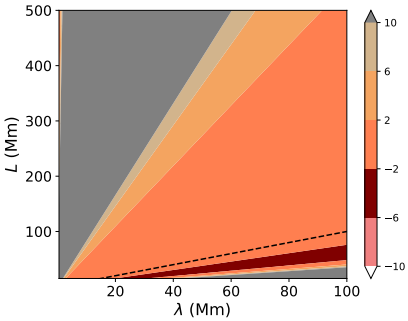

Figure 4.23: Bayes factors in the comparison between exponential and Gaussian decays by resonant absorption as a function of the observables length (L) and wavelength (λ) with uncertainties of 10% for each spatial damping ratio resulting in each l, λ combination. The dashed lines indicate $L = \lambda$. The different levels of evidence of Table 2.2 are indicated in the colour bars. NW (blue), PE (dark blue/green), SE (purple/green), VSE (white/grey).

4.6 Conclusions

In this chapter, we have inferred several physical properties of solar prominence threads by applying Bayesian techniques. The main results are the following:

- Regarding the inference of physical properties in prominence threads, our results indicate that the magnetic field strength can be properly inferred and magnitudes smaller than 20 G are obtained for a totally filled tube and even smaller for a partially tube, with a large variability depending on the particular thread that is considered in a quiescent prominence.
- With respect to damping mechanisms, resonant absorption in the Alfvén continuum is clearly the most plausible mechanism in explaining currently observed damped transverse oscillations in infinite homogeneous prominence threads. Evidence in favour of a single model becomes less clear when an longitudinally inhomogeneous tube is considered instead.
- Observations of period ratios between the fundamental kink mode and the first longitudinal overtone enable to infer the lengths of prominence threads in relation to the total length of the flux tube. Different results are obtained depending on whether the long or short thread approximations are considered. The analysis also leads to the conclusion that for the short thread approximation, density contrasts larger than 200 have a very low probability. The comparison between two analytical approximations for the period ratio of thread oscillations indicates that values of the period ratio around 1 are better explained by the long thread model, while period ratio values below 1 and above 2.5 are better explained by the short thread model.
- When flows are included in the modelling, the total length of the flux tube can be inferred leading to values in between 20-40 Mm in a particular application to an active region prominence observed with Hinode/SOT. These values are lower than those expected. In a more general case, the total length of the flux tube seems to depend on the flow velocity measurements more than on the observed length of the thread.
- As far as propagating waves are concerned, exponential or Gaussian decays are suitable for different prominence thread conditions when the same observable is considered. When both exponential and Gaussian profiles are compared, realistic spatial damping ratios do not provide us with evidence in favour of any of the profiles but the level of evidence depends on the particular observable.

Comparing the results of this Chapter with those in Chapter 3, we see that both structures, coronal loops and prominence threads, are essentially the same in terms of plasma supporting oscillations except for their density, which is key to constrain the proper values of their particular physical parameters and to extract information of their dynamics.

5

Future prospects

We keep moving forward,
opening new doors, and doing new things,
because we're curious and curiosity keeps leading us down new paths.
Walt Disney

The whole understanding of the solar corona is far away from coming true. Direct problems in which only theoretical predictions can be acquired are insufficient to solve questions in solar physics. In spite of observational efforts and improvements in numerical simulations, consistent inversion methods are required to confront theory and observations. Moreover, we need techniques to refine our studies by distinguishing between suitable and not suitable models.

This thesis entails an advance in Bayesian studies of the corona supplying that necessity, with the creation of consistent Bayesian inversion methods and their use within coronal seismology to shed light on the structure of coronal loops and prominence threads. In particular, we have developed Bayesian tools to infer fundamental physical features of these solar structures and necessary methods to compare between alternative models for explaining physical processes related to their dynamics.

From this starting point, applications to solar physics are unlimited. We focus here on most immediate problems where Bayesian techniques developed in this thesis could be helpful:

+ Within coronal seismology, properties and processes of solar structures as for example spicules can be analysed. A deeper exploration of the propagating wave theory would be helpful to extract new physical parameters

and properties of this type of waves.

Furthermore, Bayesian tools could be created to differentiate the contribution to the observed dynamics due to the presence of flows and for waves by comparing Doppler shift and periodic line asymmetries with alternative interpretations in terms of flows (Tian et al. 2011) and for waves (Verwichte et al. 2010).

On the other hand, the characterisation of wave signals can be substantially improved. Given a model for the wave amplitude such as for example the common sinusoid with the exponential decay, we can infer posterior distributions for wave parameters (phase, period or wavelength, damping time or length, and initial amplitude) offering a more consistent method than the usual fit by least-squares method.

Besides, wave signals can be completed using posterior predictive distributions. Imagine that you are measuring the properties of a wave in time and suddenly the instrument stops gathering data for some time or that you have a lack of information from some pixels. With the computation of posterior predictive distributions, the probability of those hidden data given the available ones can be computed by considering a given model for the signal. A generic example can be seen in Fig. 5.1 which shows posterior predictive distributions computed for a hundred of proposed amplitudes for each time and considering an exponential model.

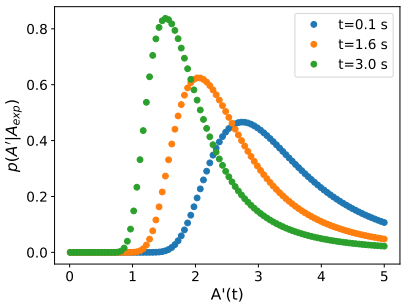

Figure 5.1: Posterior predictives of a hundred amplitudes in between 0 and 5 for three selected times. An exponential model ($A_{exp}(t) = ae^{-bt^2}$) has been assumed with uniform priors for $a \in [0.01, 5]$ and $b \in [0, 2]$.

In the same line, we could determine the profile that fits best the whole wave by model selection or by combining model selection with posterior predictive analysis. In the latter case, by creating synthetic data with very small uncertainties from different models, serving thus as templates. The

procedure starts by computing the probability of real data to belong to those models point by point, the posterior predictive distribution. Then, divide those probabilities to discern which model explains better our real data, being thus possible to differentiate even several regimes in the same signal. Figure 5.2 shows an example to illustrate the idea. Gaussian and exponential profiles have been selected to create templates and real data consisting on two points. If we compute the posterior predictive distribution of each point for each profile and divide them, we find that the probability of an exponential profile is almost the same than that for a Gaussian one for the first point ($p(d_1|d, M_{exp})/p(d_1|d, M_G) \approx 1$). However, for the second point we clearly find that the exponential profile is the most likely in explaining that data point ($p(d_2|d, M_{exp})/p(d_2|d, M_G) = 17177$).

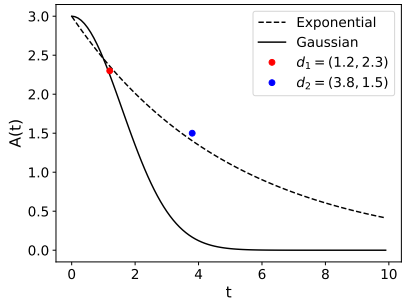

Figure 5.2: Templates of exponential and Gaussian profiles created by considering $A_{exp}(t) = ae^{-bt^2}$ and $A_G(t) = ae^{-bt}$ with uniform priors for $a \in [0.01, 5]$ and $b \in [0, 2]$. The two new points are also represented.

Bayesian techniques could also serve us to improve the efficiency of observation processes by determining how many periods are necessary to properly infer physical properties of interest in coronal structures, such as the magnetic field strength or the density.

+ But Bayesian techniques are not restricted to coronal seismology applications. In a multi-thermal corona, Differential Emission Measurements (DEMs) are widely used to quantify the amount of plasma at each temperature. However, the contribution coming from the temperature component and the density component is not clear yet. Bayesian tools are promising in this aspect because they could help us combining observations in EUV wavelengths with theoretical models of DEMs for different coronal structures.

+ Related to the previous point, different DEM models can be confronted

by using our techniques to discern dynamic processes in these structures. As an example, consider the theoretical expressions of DEMs in the appendix by Klimchuk et al. (2008) corresponding to strong evaporation, strong condensation, and static equilibrium of an active region coronal loop. If we compare them by pairs, we obtain information about the dominant physical process for the considered conditions. Figure 5.3 shows the resulting Bayes factors as a function of DEMs. Strong condensation is the most likely process in explaining values of $log_{10}DEM(T) > 10$ when it is compared with strong evaporation (panel a), static equilibrium explain better than strong evaporation all values of DEMs (panel b), and strong condensation does not seem to be the dominant process in front of static equilibrium for $log_{10}DEM(T) < 20$ but for larger values of DEMs, positive evidence in favour of strong condensation is present (panel c).

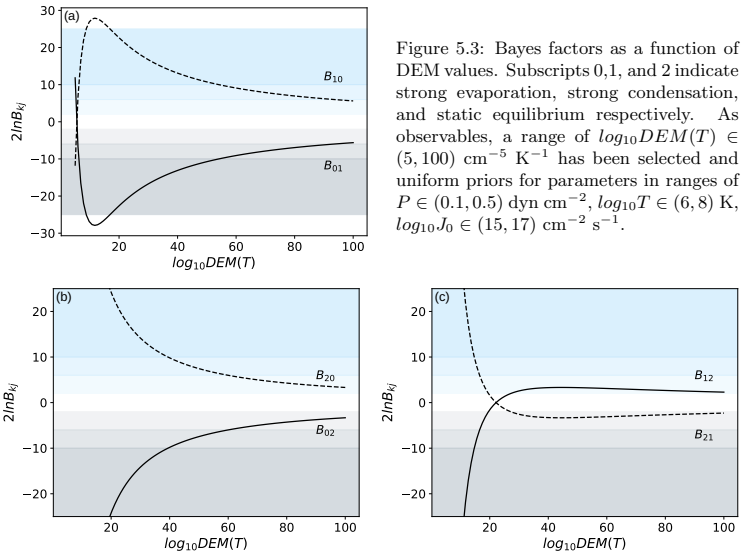

Figure 5.3: Bayes factors as a function of DEM values. Subscripts 0,1, and 2 indicate strong evaporation, strong condensation, and static equilibrium respectively. As observables, a range of $log_{10}DEM(T) \in (5, 100)$ cm^{-5} K^{-1} has been selected and uniform priors for parameters in ranges of $P \in (0.1, 0.5)$ dyn cm^{-2}, $log_{10}T \in (6, 8)$ K, $log_{10}J_0 \in (15, 17)$ cm^{-2} s^{-1}.

+ Improving methods to confront numerical simulations and observations is also a pending task in coronal analyses. The Bayesian approach could help solving this problem if the relation of uncertainties between those simulations and observations is determined.

+ Finally but not less important, Bayesian techniques for model comparison could help to solve the big question about the coronal heating, by discerning which one among the multiple proposed heating mechanisms is the most feasible or by discarding some models at least.

Hence, we do encourage to apply Bayesian statistics to coronal studies searching for new and promising knowledge of a mysterious but not less beautiful solar corona.

A

Bayesian techniques - Examples

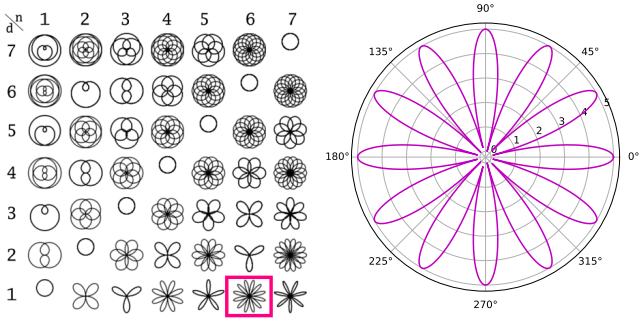

Figure A.1: Possible configurations of polar rose (left panel) with $k = n/d$ and representation of the selected polar rose for the example (right panel) where $a = 5$ and $k = 6$.

First of all, we consider a polar rose. A polar rose is a sinusoid described in polar coordinates by

$$r(\theta) = acos(k\theta), \tag{A.1}$$

where a is the length of the petals and k is a parameter that controls the number of petals. A polar rose will show 2k petals if k is even and k petals if k is odd. Figure A.1 shows possible polar roses by changing parameters (left panel) and the selected rose for this example (right panel) with $a = 5$ and $k = 6$.

Now, forget about the previous paragraph for a moment. You have received some data with their uncertainties corresponding to the radius, $d = r(\theta)$, and you decide to take Eq.(A.1) as your model. However, you do not know the values of parameters, $\boldsymbol{\theta} = \{a, k\}$, of the polar rose describing data. Your aim is to infer those two parameters using Bayesian statistics. To proceed then with this inference analysis, we must first create and plot our data set in `Python`:

```
import pylab as pb #module to plot
import numpy as np #module to do computations with arrays

"""Creation and plot of data"""
phi=np.linspace(0,2*np.pi,200) #angle values from 0 to 2pi, 200
    points
data=5*abs(np.cos(6*phi)) #data values (a*cos(k*phi))
np.random.seed(123) #indicator for repeting the same random
    process all times the code is used
data_err=0.1+0.5*np.random.rand(len(data)) #uncertainties

pb.figure(); pb.polar(data+data_err,phi,"b.") #Representation of
    data
```

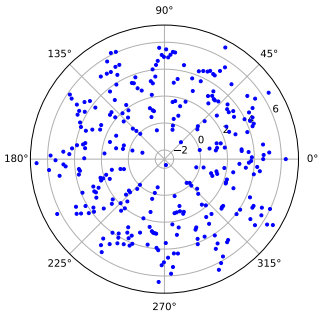

Figure A.2: Generated data in polar coordinates.

Figure A.2 shows the resulting data.

Once we have the observables $r(\theta)$, we must define our priors and the likelihood function. In this example, we assume vague information about the values of parameters, so that we cannot assign more probability to some values and less to others. Hence, a uniform prior seems to be adequate to the problem. Regarding the likelihood function, we assume a Gaussian likelihood.

A.1 Polar rose example by using direct numerical integration

To make the computations by direct numerical integration in `Python` language:

```
"""Definition of parameters"""
k=np.linspace(5.0,7.0,5000) #'k' values from 5 to 7, 5000 points
a=np.linspace(3.0,7.0,500) #'a' values from 3 to 7, 500 points
"""Definition of uniform priors"""
prior_a=1./(max(a)-min(a)) #prior of 'a'
prior_k=1./(max(k)-min(k)) #prior of 'k'

"""Computation of likelihood function"""
likelihood=np.empty((len(data),len(a),len(k)))#empty array
for q,dat in enumerate(data): #loop to consider each data value
  for i,radio in enumerate(a): #loop to each 'a' value
    for j,number in enumerate(k): #loop to each 'k' value
      model=radio*abs(np.cos(number*phi)) #theoretical value
      likelihood[q,i,j]=(1./(data_err[q]*np.sqrt(2*np.pi)))*
    np.exp(-((dat-model[q])**2)/(2*data_err[q]**2)) #Gaussian
    likelihood
#Product of likelihoods corresponding to each data value
product=1.0 #First element of the product
cont=0 #Counter initialization
while cont<len(data) :#condition of while
  product=product*likelihood[cont,:,:] #product
  cont=cont+1 #addition of one more element
```

Finally, we obtain the two-dimensional global posterior, $p(a, k|M, d)$, and one-dimensional marginal posteriors by applying the Bayes' rule and *simps* to solve the integrals:

```
import scipy.integrate as sc #Module to integrate

"""Computation and plot of global posterior"""
posterior=prior_a*prior_k*product #Bayes Rule numerator
marginal=sc.simps(sc.simps(posterior,k,axis=1),a,axis=0) #Marginal
    likelihood
posterior=posterior/marginal #Normalized global posterior

pb.figure()#New figure
x,y=pb.meshgrid(k,a) #Definition of x,y plane
pb.contourf(x,y,posterior);pb.colorbar() #plot of global prior
pb.xlabel("$k$",fontsize=16);pb.ylabel("$a$",fontsize=16 ) #labels
pb.xticks(fontsize=14);pb.yticks(fontsize=14) #axis size
pb.xlim(5.99,6.01);pb.ylim(4.9,5.1) #axis limits
pb.title("$p(\\theta|d,M)$",fontsize=14) #title

"""Computation and plot of marginal likelihoods"""
```

```
posterior_a=sc.simps(posterior,k,axis=1 )#marginal posterior for
    'a'
posterior_k=sc.simps(posterior,a,axis=0) #marginal posterior for
    'k'

pb.figure();pb.plot(a,posterior_a) #Plot of posterior distribution
    of 'a'
pb.xlabel("$a$",fontsize=16);pb.ylabel("$p(a|d,M)$",fontsize=16)
    #labels
pb.xticks(fontsize=14);pb.yticks(fontsize=14) #axis size
pb.xlim(4.8,5.2) #x-axis limits


pb.figure();pb.plot(k,posterior_k) #Plot of posterior distribution
    of 'k'
pb.xlabel("$k$",fontsize=16);pb.ylabel("$p(k|d,M)$",fontsize=16)
    #labels
pb.xticks(fontsize=14);pb.yticks(fontsize=14) #axis size
pb.xlim(5.99,6.01) #x-axis limits
```

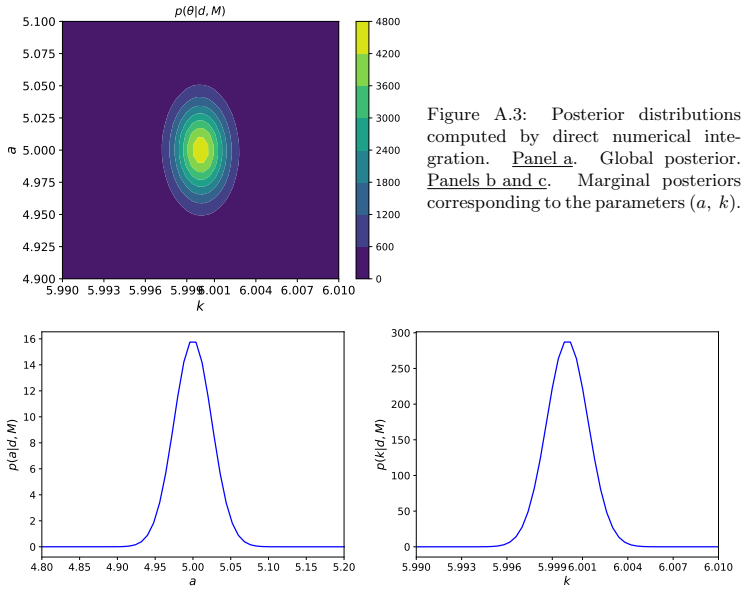

Figure A.3: Posterior distributions computed by direct numerical integration. Panel a. Global posterior. Panels b and c. Marginal posteriors corresponding to the parameters $(a,\ k)$.

Figure A.3 represents the resulting global posterior and the marginal posteriors corresponding to both a, k parameters. Clearly, the marginal posterior distributions peak at around $a = 5$ and $k = 6$ which was expected since they are the selected values at the beginning to define our data.

Note that number of points in angle and parameters arrays determine the points of parameter space that are evaluated and the smoothness of the final plots. Depending on your selection of axis and your computation capabilities you must adjust the most adequate number of points to your study.

A.2 Markov Chain Monte Carlo methods

Using the same data as before, our first step is to define the necessary functions of prior, likelihood, and posterior to sample the parameter space with them. In `Python` language:

```
"""Definition of prior.
Input: theta, array with parameters
Output: global prior value"""
def logprior(theta):
  if theta0_min<theta[0]<theta0_max and
    theta1_min<theta[1]<theta1_max:
     return
    -np.log(theta0_max-theta0_min)-np.log(theta1_max-theta1_min)
  return -np.inf

"""Definition of the likelihood.
Input: theta, angulo, y, sigma (arrays with parameters, angles,
    data, and uncertainties respectively)
Output: likelihood"""
def loglike(theta,angulo,y,sigma):
  model =theta[0]*abs(np.cos(theta[1]*angulo))
  return -sum((((y-model)**2)/(2*sigma**2)) -
    np.log(sigma*np.sqrt(2*np.pi)))

"""Definition of the posterior.
Input:  theta, angulo, y, sigma (arrays with parameters, angles,
    data, and uncertainties respectively)
Output: global posterior"""
def logprob(theta,angulo,y,sigma):
  lp=logprior(theta)
  if not np.isfinite(lp):
    return -np.inf
  return lp+loglike(theta,angulo,y,sigma)
```

Now, we introduce the initial values for the parameters, their plausible ranges, and perform the MCMC sampling:

```
import emcee #MCMC sampler package
theta0_true=5.1 #initial value of a
theta1_true=5.9 #initial value of k

theta0_min=3.0;theta0_max=7.0 #minimum and maximum values of a
theta1_min=4.0;theta1_max=8.0 #minimum and maximum values of k

N=len(data) #number of data
ndim,nwalkers=2,20 #dimensions (number of parameters) and walkers
nsteps=300 #steps given by each walker
p0=np.array([theta0_true,theta1_true]) #initial values of
    parameters
disp=np.array([0.01*theta0_true,0.01*theta1_true]) #dispersed
    initial values
pos=[p0+disp*np.random.randn(ndim) for i in range(nwalkers)]
    #initial value per each walker
sampler = emcee.EnsembleSampler(nwalkers, ndim, logprob,
    args=(phi,data,data_err)) #parameter space to sample
sampler.run_mcmc(pos,nsteps) #SAMPLING
```

To check that the algorithm has sampled well, we represent the *trace plot* which shows the chains i.e. the walkers ways in the parameter space. In `Python` language:

```
fig, axes=plt.subplots(2,1,sharex=True,figsize=(8,9)) #define a
    subplot with 2 panels
axes[0].plot(sampler.chain[:, :, 0].T,color="k",alpha=0.4) #chain
    of first parameter
axes[0].yaxis.set_major_locator(plt.MaxNLocator(5)) #adjustment of
    y-axis in the best possible location
axes[0].axhline(theta0_true,color="#888888",lw=2) #horizontal line
    at the initial value
axes[0].set_ylabel("a") #y-label
axes[1].plot(sampler.chain[:,:,1].T,color="k",alpha=0.4)#chain of
    second parameter
axes[1].yaxis.set_major_locator(plt.MaxNLocator(5)) #adjustment of
    y-axis in the best possible location
axes[1].axhline(theta1_true,color="#888888",lw=2) #horizontal line
    at the initial value
axes[1].set_ylabel("k") #y-label
axes[1].set_xlabel("steps") #x-label
plt.tight_layout(h_pad=0.0) #adjustment of panels
```

Figure A.4 shows the trace plot for a well sampled (left) parameter space. We have included a trace plot of a bad sampled (right) parameter space for comparison purposes. We can be sure that MCMC works properly when after some steps the walkers ways converge and oscillate around one value, the walkers

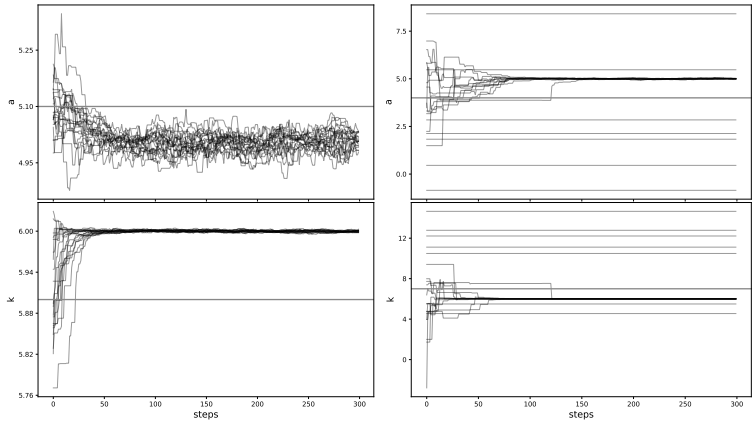

Figure A.4: Trace plots. Panel a. Proper MCMC sampling. Panel b. Non-convergent case where MCMC sampling does not works well.

agreed in that value.

At the same left panel of Fig. A.4, we further observe that because the initial value is far away from the most probable, a transient feature appears at the beginning where the walker moves to the important region. This transient feature lasts for about 20% of the steps and is called burn-in and it is normally excluded from the sample. The effect of discarding these points can be seen in Fig. A.5 where the sampled parameter space with the density of points proportional to the global posterior is plotted before (left) and after (right) burn-in. This procedure is translated to the code as:

```
plt.figure() #new figure
plt.plot(sampler.chain[:,:,0],sampler.chain[:,:,1],"k.") #sampled
    space before burn-in
plt.xlabel("a",fontsize=14);plt.ylabel("k",fontsize=14) #labels

burnin=0.2 #percentage of removed samples (20%)
samples=sampler.chain[:,int(nsteps*burnin):,:].reshape((-1,ndim))
    #selection of remaining samples

plt.figure() #new figure
plt.plot(samples[:,0],samples[:,1],"k.") #sampled space after
    burn-in
plt.xlabel("a",fontsize=14);plt.ylabel("k",fontsize=14) #labels
```

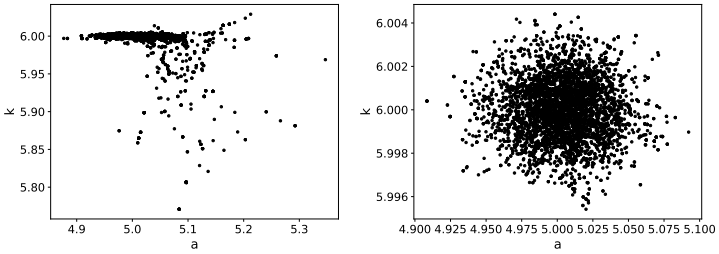

Figure A.5: Global posterior before (*left*) and after (*right*) burn-in.

After burn-in, we obtain the marginal posteriors. At this point, the two common ways to represent them are corner plots and histograms. In the former, global and marginal posteriors can be looked with a single view as in Fig. A.7. At the left panel is the corner plot of the well sampled case and at the right panel the corner plot corresponding to the bad sampled case.

```
fig=corner(samples,labels=["a","k"],smooth=3,bins=100,
    truths=[theta0_true,theta1_true]) #corner plot
```

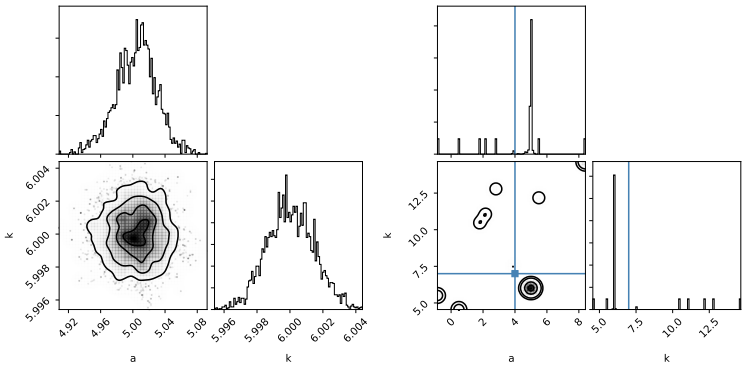

Figure A.6: Corner plots. Left. Proper cornet plot. Right. Non-convergent case. Blue lines indicate initial points.

The second way for representing the posteriors is the histogram for each parameter separately. Figure A.7 shows the results for this example.

```
plt.figure()
plt.hist(samples[:,0],bins=100,density=True,color="b") #marginal
    posterior for the first parameter
plt.xlabel("a",fontsize=14);plt.ylabel("p($a|d,M$)",fontsize=14)
    #labels

plt.figure()
plt.hist(samples[:,1],bins=100,density=True,color="b") #marginal
    posterior for the second parameter
plt.xlabel("k",fontsize=14);plt.ylabel("p($k|d,M$)",fontsize=14)
    #labels
```

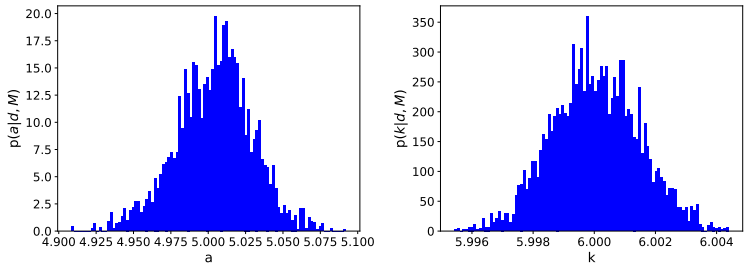

Figure A.7: Marginal posteriors for parameters associated to polar rose (a, k) by MCMC sampling.

From both Figs. A.6 and A.7, we conclude that the marginal posterior distributions peak at around $a = 5$ and $k = 6$ as one might expect.

Performing the polar rose example by using both computation techniques, we notice that the computational time of around seconds by using the MCMC code, even when plausible ranges for parameters are wider than for direct integration code, whose computational time is about hours (by using a commercial computer with i5 intel processor and 4 GB RAM).

B

Bayesian seismology of coronal loops

B.1 Physical parameters depending on different priors

In Section 3.1 we mentioned that a uniform prior for ρ_i could not be the best option in the inference of the magnetic field strength, since the range of plausible values for this parameter spreads over decades (see Chapter 2 for the explanation of the uniform prior non-adequacy). In this section of the appendix, we show the results of performing the first inference analysis in Section 3.1, but with different priors for both parameters, ζ and ρ_i.

We propose uninformative priors in order to represent the same state of belief than with a uniform one, but trying to solve the inherent problem of this type of prior. First, we considered different priors for ζ with a uniform prior for ρ_i. Priors are (explicit expressions can be found in Chapter 2):

- Uniform. The same prior than in Fig. 3.5 in order to compare.
- Normal distribution with $\mu_\zeta = 5.5$ and $\sigma_\zeta = 7.75$.
- Cauchy distributions.
- Exponential distribution with $a = C/4$ and $b = 1/4$, where C is the normalisation constant.

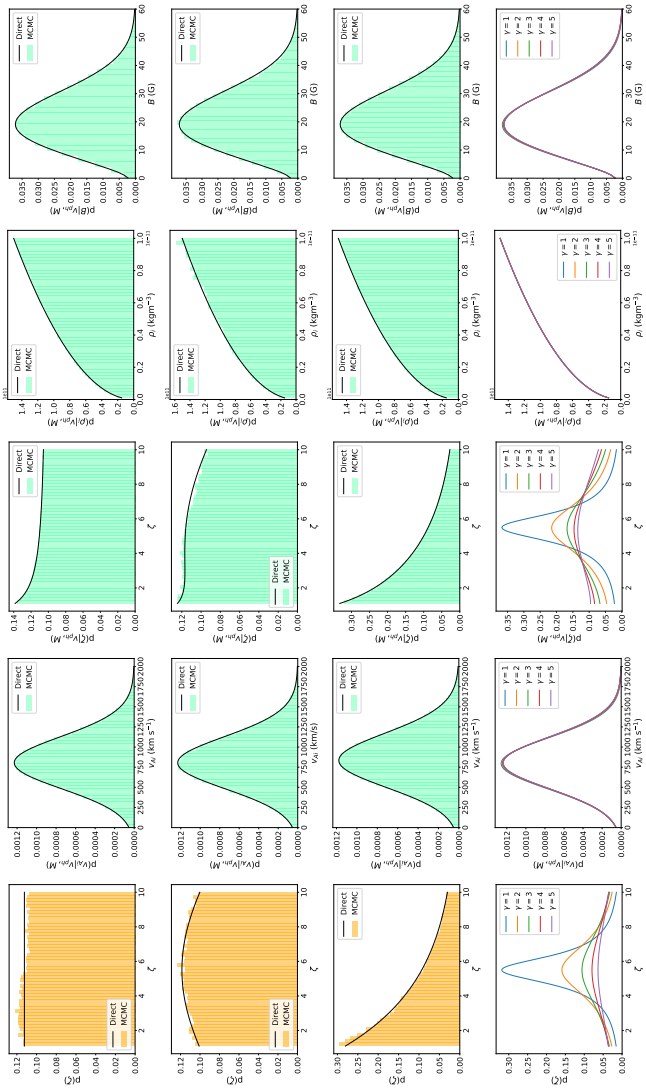

Figure B.1: Posterior distributions inferred for v_{Ai} (second column), ζ (third column), ρ_i (fourth column), and B (last column) when changing prior of ζ (first column). Selected prior sorted by rows from up to down are uniform, normal ($\mathcal{N}(5.5, 7.75^2)$), exponential ($C/4 \exp 1/4$), and Cauchy distributions ($1/\left(\pi\gamma\left[1+((\zeta-\mu_\zeta)/\gamma)^2\right]\right)$) with γ values in the legend).

Figure B.1 shows the priors (left most panels) and the posterior distributions for internal Alfvén velocity (first column), density contrast (second column), density (third column), and magnetic field strength (last column). The results have been computed using both direct numerical integration (continuous lines) and also MCMC sampling (histograms) of the prior and the posterior, although only results by direct integration are shown in the case of Cauchy priors to not deface the plot. As can be seen, the use of uniform, normal, Cauchy, or exponential priors for the density contrast influences the marginal posterior obtained for the same parameter. Basically, what one gets as posterior is very similar to what we had as input in the prior. In all four cases, the marginal posterior for the density is unaffected. More importantly, the marginal posterior for the magnetic field strength is unaffected. The inference of magnetic field strength is therefore robust in front of changes in the employed prior distribution for density contrast.

Now, we assume a uniform prior for ζ and different priors for ρ_i in the analysis. In this case, the priors are:

- A Jeffreys prior with $\rho_i^{\min} = 10^{-13}$ kg m^{-3} and $\rho_i^{\max} = 10^{-11}$ kg m^{-3}, corresponding to the full range considered in Fig. 3.5.

- A normal distribution with $\mu_{\rho_i} = 10^{-12}$ kg m^{-3} and $\sigma^2_{\rho_i} = 5 \times 10^{-12}$ kg m^{-3}.

The results from this analysis are shown in Fig. B.2. Again, each row corresponds to results from the inversion using a different prior on density, indicated on the leftmost panel. Similarly to the previous case, changes in the prior information for the density do affect the marginal posterior obtained for this parameter, but do not influence significantly the marginal posteriors for the other three parameters of the problem, internal Alfvén velocity, density contrast and magnetic field strength. The posterior for density contrast seems to be completely independent of the information on the density of the waveguide. Only in the case of a Jeffreys prior for the density, the posterior for the magnetic field strength is slightly affected (see rightmost panel in Fig. B.2).

In summary, what one is willing to accept a priori about the density and the density contrast affects their corresponding posteriors, but very little the inference of the magnetic field strength. The four parameters seem to be rather independent, since changes in the prior information do not seem to affect the regions of parameter space where the likelihood is large. Hence, depending on the information we require, the use of a uniform or another uninformative prior does not change our conclusions. However, this is not true if we consider

specific measurements, with for example, an informative Gaussian prior (see Fig. 3.7).

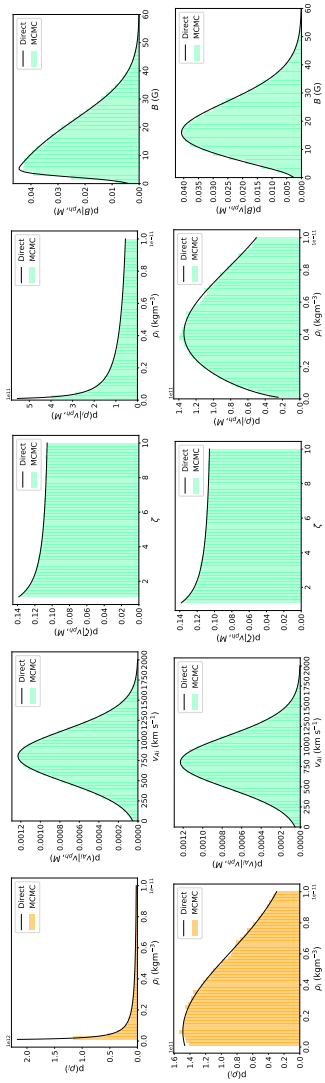

Figure B.2: Posterior distributions inferred for v_{Ai} (second column), ζ (third column), ρ_i (fourth column), and B (last column) when changing prior of ρ_i (first column). Selected prior sorted by rows from up to down are Jeffreys $\left(\left[\rho_i log\left(\rho_i^{\max}/\rho_i^{\min}\right)\right]^{-1}\right)$ and normal $(\mathcal{N}(10^{-12}, (5\times10^{-12})^2))$ distributions.

B.2 Magnetic field strength in solar coronal loops

Table B.1: Data of coronal loop oscillations and medians of the inferred distributions.

Ev.ID	Lp.ID	L (Mm)	P (s)	v_{ph} (km s^{-1})	v_{Ai} (km s^{-1})	B_0 (G)	B_u (G)	B_G (G)
Nakariakov & Ofman (2001)								
1	1	130	256	1020 ± 132	829 ± 121	-	23^{+5}_{-7}	19^{+5}_{-4}
2	1	190	360	1030 ± 410	829 ± 323	13 ± 9	22^{+11}_{-10}	19^{+9}_{-8}
Aschwanden et al. (2002)								
a	1	168	261	1287	1031^{+121}_{-101}	13	29^{+6}_{-9}	14 ± 3
b	1	72	265	543	445^{+61}_{-40}	6	13^{+2}_{-4}	7^{+1}_{-2}
d	1	174	316	1101	889 ± 101	11	25^{+5}_{-8}	12^{+3}_{-2}
f	1	204	277	1473	1172^{+141}_{-121}	16	33^{+7}_{-10}	16^{+4}_{-3}
g	1	162	272	1191	950^{+121}_{-101}	10	27^{+6}_{-9}	11^{+3}_{-2}
a	3	390	522	1494	1192^{+141}_{-121}	11	33^{+8}_{-10}	12 ± 3
a	4	258	435	1186	950^{+121}_{-101}	13	26^{+7}_{-8}	14 ± 3
c	5	166	143	2322	1778 ± 162	27	52^{+12}_{-16}	27^{+7}_{-6}
a	10	406	423	1920	1515^{+202}_{-162}	20	43^{+10}_{-13}	21 ± 5
a	16	192	185	2076	1637^{+182}_{-162}	15	47^{+10}_{-15}	15^{+4}_{-3}
a	17	146	396	737	607^{+61}_{-81}	6	17^{+4}_{-5}	7^{+1}_{-2}
Van Doorsselaere et al. (2008b)								
1	1	390	296 ± 24	2600 ± 500	1758^{+182}_{-283}	39 ± 8	56 ± 18	35^{+11}_{-10}

Ev.ID	Lp.ID	L (Mm)	P (s)	v_{ph} (km s^{-1})	v_{Ai} (km s^{-1})	B_0 (G)	B_u (G)	B_G (G)
White & Verwichte (2012b)								
1	1	121 ± 2	225 ± 40	1080 ± 220	869 ± 182	3.9-5.6 (12.5-17.6)	23^{+8}_{-7}	15^{+5}_{-4}
1	2	111 ± 6	215 ± 5	1030 ± 110	829 ± 101	3.8-5.3 (11.9-16.8)	23^{+5}_{-7}	15^{+3}_{-4}
1	3	132	213 ± 9	1240 ± 140	990^{+141}_{-121}	4.5-6.4 (14.3-20.3)	27^{+7}_{-8}	17^{+5}_{-4}
1	4	113 ± 4	216 ± 30	1050 ± 170	849 ± 141	3.8-5.4 (14.4-20.4)	23 ± 7	15 ± 4
2	1	396	520 ± 5	1520 ± 150	1213^{+141}_{-121}	5.6-7.9 (17.6-24.8)	34^{+7}_{-11}	21 ± 5
2	2	374	596 ± 50	1260 ± 160	1011 ± 141	4.6-6.5 (14.6-20.6)	28^{+7}_{-9}	18 ± 4
3	1	279 ± 3	212 ± 20	2630 ± 360	1838^{+121}_{-202}	9.6-13.6 (30.4-42.9)	58^{+15}_{-18}	36 ± 9
3	2	240 ± 4	256 ± 20	1880 ± 250	1495^{+222}_{-202}	6.8-9.7 (21.7-30.7)	41^{+11}_{-13}	26^{+7}_{-6}
3	3	241	135 ± 9	3570 ± 430	1939^{+61}_{-121}	13.0-18.4 (41.2-58.3)	75^{+16}_{-23}	50 ± 12
3	4	159 ± 6	115 ± 2	2770 ± 280	1919^{+81}_{-141}	10.1-14.3 (32.0-45.3)	61^{+15}_{-18}	38 ± 9
3	5	132	103 ± 8	2560 ± 330	1838^{+121}_{-202}	9.4-13.2 (29.6-41.8)	56^{+15}_{-17}	35 ± 9

Ev.ID	Lp.ID	L (Mm)	P (s)	v_{ph} (km s^{-1})	v_{Ai} (km s^{-1})	B_0 (G)	B_u (G)	B_G (G)
Verwichte et al. (2013)								
-	-	301 ± 30	565 ± 4	1065 ± 106	849^{+121}_{-81}	- (12.3 - 17.4)	24^{+5}_{-7}	15^{+4}_{-3}
-	-	274 ± 30	222 ± 18	2468 ± 336	1798^{+162}_{-202}	- (28.5 - 40.3)	54^{+15}_{-17}	34 ± 9
-	-	400 ± 30	474 ± 12	1688 ± 134	1334^{+162}_{-101}	- (19.5 - 27.5)	37^{+9}_{-11}	24^{+5}_{-6}
-	-	400 ± 30	1170 ± 6	684 ± 51	546^{+61}_{-40}	- (7.9 - 11.2)	16^{+3}_{-5}	10 ± 2
-	-	270 ± 30	623 ± 4	867 ± 96	708 ± 81	- (10.0 - 14.1)	19 ± 5	12^{+3}_{-2}
-	-	188 ± 20	150 ± 5	2507 ± 279	1838^{+121}_{-162}	- (28.9 - 40.9)	56^{+13}_{-17}	34^{+9}_{-8}
-	-	160 ± 20	122 ± 6	2623 ± 352	1838^{+121}_{-182}	- (30.3 - 42.8)	58^{+15}_{-18}	36 ± 9
-	-	171 ± 20	273 ± 54	1253 ± 288	1011 ± 242	- (14.5 - 20.4)	27^{+9}_{-10}	17^{+6}_{-5}
-	-	122 ± 20	282 ± 6	865 ± 143	708 ± 121	- (10.0 - 14.1)	19 ± 6	12^{+4}_{-3}
-	-	262 ± 20	491 ± 18	1067 ± 90	849^{+101}_{-81}	- (12.3 - 17.4)	24^{+5}_{-7}	15^{+4}_{-3}
-	-	238 ± 20	348 ± 7	1368 ± 118	1091^{+121}_{-101}	- (15.8 - 22.3)	30^{+7}_{-9}	19^{+5}_{-4}
-	-	200 ± 20	340 ± 3	1176 ± 118	950 ± 101	- (13.6 - 19.2)	26^{+6}_{-8}	17^{+3}_{-4}

Ev.ID	Lp.ID	L (Mm)	P (s)	v_{ph} (km s^{-1})	v_{Ai} (km s^{-1})	B_0 (G)	B_u (G)	B_G (G)
Goddard et al. (2016)								
1	1	232	205 ± 4	2261 ± 40	1764^{+166}_{-60}	- (26.1 - 36.9)	51^{+10}_{-15}	32^{+6}_{-7}
1	2	78	2467 ± 3	633 ± 8	498^{+45}_{-15}	- (7.3 - 10.3)	15^{+2}_{-5}	9^{+2}_{-1}
2	1	156	398 ± 4	783 ± 7	619^{+60}_{-15}	- (9.0 - 12.8)	18^{+3}_{-5}	12^{+2}_{-3}
3	1	213	148 ± 2	2886 ± 35	2246^{+211}_{-75}	- (33.3 - 47.1)	65^{+12}_{-20}	40^{+8}_{-9}
3	2	262	217 ± 5	2413 ± 53	1885^{+166}_{-75}	- (27.8 - 39.4)	55^{+10}_{-17}	34^{+6}_{-8}
3	3	311	242 ± 6	2566 ± 64	2005^{+181}_{-90}	- (29.6 - 41.9)	58^{+11}_{-18}	36^{+7}_{-8}
4	1	183	137 ± 2	2664 ± 35	2066^{+196}_{-60}	- (30.7 - 43.5)	60^{+11}_{-18}	37^{+7}_{-8}
4	2	181	208 ± 2	1739 ± 15	1357^{+121}_{-45}	- (20.1 - 28.4)	39^{+7}_{-12}	24 ± 5
5	1	438	422 ± 4	2077 ± 18	1614^{+151}_{-45}	- (24.0 - 33.9)	47^{+9}_{-14}	29 ± 6
6	1	430	483 ± 16	1781 ± 58	1403^{+121}_{-75}	- (20.5 - 29.1)	40^{+7}_{-12}	25 ± 5
7	1	162	101 ± 1	3195 ± 38	2473^{+211}_{-75}	- (36.9 - 52.2)	72^{+13}_{-22}	44^{+9}_{-10}
8	1	207	224 ± 4	1845 ± 35	1448^{+136}_{-60}	- (21.3 - 30.1)	41^{+8}_{-12}	26^{+5}_{-6}

Ev.ID	Lp.ID	L (Mm)	P (s)	v_{ph} (km s^{-1})	v_{Ai} (km s^{-1})	B_0 (G)	B_u (G)	B_G (G)
9	1	264	308 ± 10	1712 ± 57	1342^{+121}_{-60}	- (19.8 - 27.9)	38^{+8}_{-11}	24 ± 5
9	2	326	537 ± 8	1214 ± 19	950^{+90}_{-30}	- (14.0 - 19.8)	27^{+6}_{-8}	17^{+4}_{-3}
10	1	397	688 ± 10	1155 ± 17	905^{+90}_{-30}	- (13.3 - 18.8)	26^{+5}_{-8}	17^{+3}_{-4}
10	2	279	509 ± 10	1097 ± 21	860^{+75}_{-30}	- (12.7 - 17.9)	25^{+4}_{-8}	16^{+3}_{-4}
11	1	78	238 ± 4	657 ± 12	528^{+45}_{-30}	- (7.6 - 10.7)	15^{+3}_{-4}	10 ± 2
11	2	95	231 ± 7	823 ± 24	649^{+60}_{-30}	- (9.5 - 13.4)	19^{+3}_{-6}	12 ± 2
11	3	118	156 ± 3	1513 ± 29	1192^{+105}_{-45}	- (17.5 - 24.7)	34^{+6}_{-10}	21^{+5}_{-4}
11	4	125	229 ± 2	1094 ± 11	860^{+75}_{-30}	- (12.6 - 17.8)	25^{+4}_{-8}	16^{+3}_{-4}
11	5	135	305 ± 4	884 ± 10	694^{+75}_{-15}	- (10.2 - 14.4)	20^{+4}_{-6}	13^{+2}_{-3}
11	6	160	368 ± 13	870 ± 30	694^{+60}_{-30}	- (10.0 - 14.2)	20^{+4}_{-6}	13^{+2}_{-3}
12	1	148	334 ± 4	887 ± 11	694^{+75}_{-15}	- (10.2 - 14.5)	20^{+4}_{-6}	13^{+2}_{-3}
15	1	174	458 ± 22	759 ± 37	604^{+60}_{-30}	- (8.8 - 12.4)	17^{+4}_{-5}	11 ± 2
16	1	242	157 ± 2	3079 ± 47	2397^{+211}_{-90}	-	69^{+13}_{-21}	43^{+8}_{-10}

Ev.ID	Lp.ID	L (Mm)	P (s)	v_{ph} (km s^{-1})	v_{Ai} (km s^{-1})	B_0 (G)	B_u (G)	B_G (G)
16	2	146	141 ± 4	2071 ± 62	1629^{+136}_{-75}	- (35.5 - 50.3)	47^{+9}_{-14}	29 ± 6
16	3	318	314 ± 11	2027 ± 74	1598^{+136}_{-90}	- (23.9 - 33.8)	46^{+9}_{-14}	28 ± 6
17	1	153	124 ± 2	2464 ± 48	1915^{+181}_{-60}	- (23.4 - 33.1)	56^{+10}_{-17}	34 ± 7
18	1	289	431 ± 19	1342 ± 60	1056^{+105}_{-60}	- (28.4 - 40.2)	30^{+6}_{-9}	19 ± 4
18	2	284	571 ± 7	994 ± 11	785^{+75}_{-30}	- (15.5 - 21.9)	23^{+4}_{-7}	14 ± 3
18	3	393	781 ± 10	1006 ± 13	785^{+75}_{-15}	- (11.5 - 16.2)	23^{+4}_{-7}	15^{+2}_{-4}
19	1	123	584 ± 12	421 ± 9	348^{+30}_{-15}	- (11.6 - 16.4)	10^{+2}_{-3}	7^{+1}_{-2}
19	2	348	676 ± 7	1029 ± 11	815^{+75}_{-30}	- (4.9 - 6.9)	23^{+5}_{-7}	15 ± 3
20	1	253	322 ± 14	1573 ± 68	1237^{+121}_{-60}	- (11.9 - 16.8)	35^{+7}_{-11}	22 ± 5
21	1	499	429 ± 121	2326 ± 654	1840^{+512}_{-512}	- (18.2 - 25.7)	49^{+20}_{-18}	31^{+12}_{-10}
22	1	288	162 ± 7	3556 ± 145	2744^{+151}_{-136}	- (26.8 - 38.0)	78^{+14}_{-24}	50^{+10}_{-11}
23	1	365	922 ± 24	792 ± 21	634^{+45}_{-30}	- (41.0 - 58.0)	18^{+4}_{-5}	12^{+2}_{-3}
						- (9.1 - 12.9)		

Ev.ID	Lp.ID	L (Mm)	P (s)	v_{ph} (km s^{-1})	v_{Ai} (km s^{-1})	B_0 (G)	B_u (G)	B_G (G)
24	1	432	1072 ± 18	806 ± 14	634^{+60}_{-15}	- (9.3 - 13.2)	19^{+3}_{-6}	12^{+2}_{-3}
24	2	427	987 ± 17	865 ± 15	679^{+60}_{-15}	- (10.0 - 14.1)	20^{+3}_{-6}	13^{+2}_{-3}
24	3	538	12288 ± 35	877 ± 25	694^{+60}_{-30}	- (10.1 - 14.3)	20^{+4}_{-6}	13^{+2}_{-3}
25	1	156	308 ± 7	1014 ± 22	800^{+75}_{-30}	- (11.7 - 16.5)	23^{+4}_{-7}	15^{+2}_{-3}
25	2	264	438 ± 10	1205 ± 26	950^{+90}_{-45}	- (13.9 - 19.7)	27^{+5}_{-8}	17^{+4}_{-3}
26	1	473	717 ± 8	1319 ± 14	1026^{+105}_{-30}	- (15.2 - 21.5)	30^{+5}_{-9}	19^{+3}_{-4}
26	2	185	751 ± 11	493 ± 7	393^{+45}_{-15}	- (5.7 - 8.0)	12^{+2}_{-4}	8^{+1}_{-2}
27	1	244	917 ± 24	532 ± 14	423^{+45}_{-15}	- (6.1 - 8.7)	13^{+2}_{-4}	8 ± 2
29	1	154	223 ± 3	1384 ± 19	1086^{+105}_{-30}	- (16.0 - 22.6)	31^{+6}_{-9}	20^{+4}_{-5}
31	1	162	460 ± 2	704 ± 4	559^{+45}_{-15}	- (8.1 - 11.5)	16^{+3}_{-5}	10 ± 2
31	2	138	575 ± 5	480 ± 5	378^{+45}_{-6}	- (5.5 - 7.8)	11^{+2}_{-3}	7^{+2}_{-1}
31	3	532	694 ± 7	1534 ± 16	1192^{+121}_{-30}	- (17.7 - 25.0)	34^{+7}_{-10}	22^{+4}_{-5}
32	1	234	257 ± 1	1822 ± 9	1418^{+136}_{-45}	-	41^{+7}_{-13}	26^{+5}_{-6}

Ev.ID	Lp.ID	L (Mm)	P (s)	v_{ph} (km s^{-1})	v_{Ai} (km s^{-1})	B_0 (G)	B_u (G)	B_G (G)
						(21.0 - 29.7)		
32	2	233	203 ± 1	2298 ± 14	1779^{+181}_{-45}	-	52^{+10}_{-16}	32^{+6}_{-7}
						(26.5 - 37.5)		
33	1	314	281 ± 5	2232 ± 38	1734^{+166}_{-60}	-	51^{+9}_{-16}	31^{+6}_{-7}
						(25.8 - 36.4)		
33	2	407	391 ± 6	2081 ± 32	1629^{+151}_{-60}	-	47^{+9}_{-14}	29 ± 6
						(24.0 - 34.0)		
34	1	333	597 ± 16	1116 ± 30	875^{+90}_{-30}	-	25^{+5}_{-7}	16 ± 3
						(12.9 - 18.2)		
35	1	327	527 ± 8	1241 ± 18	981^{+90}_{-45}	-	28^{+5}_{-8}	18^{+3}_{-4}
						(14.3 - 20.3)		
35	2	312	346 ± 6	1802 ± 31	1403^{+136}_{-45}	-	40^{+8}_{-12}	25 ± 5
						(20.8 - 29.4)		
36	1	282	401 ± 6	1407 ± 21	1101^{+105}_{-30}	-	32^{+6}_{-10}	20 ± 4
						(16.2 - 23.0)		
37	1	358	496 ± 13	1443 ± 38	1131^{+105}_{-45}	-	32^{+7}_{-9}	20 ± 4
						(16.7 - 23.6)		
38	1	224	182 ± 2	2456 ± 24	1915^{+181}_{-60}	-	56^{+10}_{-17}	34 ± 7
						(28.3 - 40.1)		
38	2	270	312 ± 5	1731 ± 27	1357^{+121}_{-45}	-	39^{+7}_{-12}	24 ± 5
						(20.0 - 28.2)		
38	3	424	785 ± 13	1081 ± 17	845^{+90}_{-30}	-	25^{+4}_{-8}	16^{+3}_{-4}
						(12.5 - 17.6)		
38	4	478	644 ± 11	1484 ± 25	1161^{+105}_{-45}	-	33^{+7}_{-10}	21^{+4}_{-5}
						(17.1 - 24.2)		

Ev.ID	Lp.ID	L (Mm)	P (s)	v_{ph} (km s^{-1})	v_{Ai} (km s^{-1})	B_0 (G)	B_u (G)	B_G (G)
39	1	402	647 ± 6	1242 ± 12	966^{+105}_{-15}	- (14.3 - 20.3)	28^{+5}_{-8}	18^{+3}_{-4}
39	2	334	641 ± 7	1042 ± 12	815^{+75}_{-15}	- (12.0 - 17.0)	24^{+4}_{-7}	15 ± 3
39	3	376	754 ± 22	997 ± 29	785^{+75}_{-30}	- (11.5 - 16.3)	23^{+4}_{-7}	14 ± 3
39	4	454	858 ± 10	1058 ± 13	830^{+75}_{-30}	- (12.2 - 17.3)	24^{+4}_{-7}	15 ± 3
40	1	171	341 ± 4	1004 ± 11	785^{+75}_{-15}	- (11.6 - 16.4)	23^{+4}_{-7}	14 ± 3
40	2	347	337 ± 2	2062 ± 11	1598^{+166}_{-45}	- (23.8 - 33.7)	47^{+9}_{-14}	29 ± 6
40	3	325	355 ± 42	1830 ± 216	1448^{+211}_{-181}	- (21.1 - 29.9)	40^{+10}_{-12}	25^{+7}_{-6}
40	4	258	332 ± 2	1555 ± 11	1207^{+121}_{-30}	- (17.9 - 25.4)	35^{+6}_{-11}	22^{+4}_{-5}
40	5	297	325 ± 1	1827 ± 7	1418^{+136}_{-30}	- (21.1 - 29.8)	41^{+7}_{-13}	26^{+5}_{-6}
40	6	425	416 ± 2	2044 ± 12	1583^{+166}_{-45}	- (23.6 - 33.4)	47^{+8}_{-14}	29^{+5}_{-7}
40	7	353	343 ± 4	2057 ± 22	1598^{+151}_{-45}	- (23.7 - 33.6)	47^{+8}_{-14}	29^{+6}_{-7}
40	8	238	260 ± 5	1832 ± 34	1433^{+136}_{-45}	- (21.1 - 29.9)	41^{+8}_{-13}	26^{+5}_{-6}
40	9	473	371 ± 3	2551 ± 21	1975^{+196}_{-45}	-	58^{+10}_{-18}	35^{+8}_{-7}

Ev.ID	Lp.ID	L (Mm)	P (s)	v_{ph} (km s^{-1})	v_{Ai} (km s^{-1})	B_0 (G)	B_u (G)	B_G (G)
						(29.4 - 41.6)		
40	10	238	376 ± 2	1265 ± 6	996^{+90}_{-30}	-	29^{+5}_{-9}	18 ± 4
						(14.6 - 20.7)		
40	11	220	286 ± 2	1541 ± 13	1207^{+105}_{-45}	-	35^{+6}_{-11}	22^{+4}_{-5}
						(17.8 - 25.1)		
43	1	363	428 ± 4	1695 ± 17	1327^{+121}_{-45}	-	38^{+7}_{-12}	24 ± 5
						(19.6 - 27.7)		
43	2	241	216 ± 2	2231 ± 19	1734^{+166}_{-45}	-	51^{+9}_{-16}	31^{+6}_{-7}
						(25.8 - 36.4)		
43	3	368	501 ± 5	1469 ± 14	1146^{+105}_{-30}	-	33^{+6}_{-10}	21^{+4}_{-5}
						(17.0 - 24.0)		
43	4	222	310 ± 2	1434 ± 8	1116^{+105}_{-30}	-	32^{+6}_{-10}	20 ± 4
						(16.6 - 23.4)		
43	5	260	270 ± 1	1926 ± 9	1493^{+151}_{-45}	-	43^{+8}_{-13}	27^{+5}_{-6}
						(22.2 - 31.4)		
44	1	295	434 ± 4	1360 ± 11	1071^{+90}_{-45}	-	31^{+5}_{-10}	19 ± 4
						(15.7 - 22.2)		
44	2	512	587 ± 11	1745 ± 34	1357^{+136}_{-45}	-	39^{+7}_{-12}	25^{+4}_{-6}
						(20.1 - 28.5)		
44	3	352	417 ± 8	1688 ± 34	1327^{+121}_{-60}	-	38^{+7}_{-12}	24^{+4}_{-5}
						(19.5 - 27.6)		
44	4	202	145 ± 3	2794 ± 58	2171^{+211}_{-75}	-	63^{+12}_{-19}	39^{+8}_{-9}
						(32.2 - 45.6)		
45	1	92	149 ± 2	1237 ± 20	966^{+90}_{-30}	-	28^{+5}_{-9}	18^{+3}_{-4}
						(14.3 - 20.2)		

Ev.ID	Lp.ID	L (Mm)	P (s)	v_{ph} (km s^{-1})	v_{Ai} (km s^{-1})	B_0 (G)	B_u (G)	B_G (G)
46	1	430	724 ± 14	1188 ± 23	935^{+90}_{-30}	- (13.7 - 19.4)	27^{+5}_{-8}	17^{+3}_{-4}
46	2	498	659 ± 7	1510 ± 15	1176^{+121}_{-30}	- (17.4 - 24.7)	34^{+6}_{-10}	21^{+5}_{-4}
46	3	384	594 ± 6	1293 ± 13	1011^{+90}_{-30}	- (14.9 - 21.1)	29^{+6}_{-9}	18 ± 4
47	1	225	316 ± 8	1423 ± 38	1116^{+105}_{-45}	- (16.4 - 23.2)	32^{+6}_{-10}	20 ± 4
47	2	222	301 ± 7	1474 ± 35	1161^{+105}_{-45}	- (17.0 - 24.1)	33^{+6}_{-10}	21^{+4}_{-5}
48	1	540	917 ± 10	1178 ± 12	920^{+90}_{-30}	- (13.6 - 19.2)	27^{+5}_{-8}	17^{+3}_{-4}
48	2	588	946 ± 7	1244 ± 9	981^{+90}_{-30}	- (14.4 - 20.3)	28^{+5}_{-8}	18^{+3}_{-4}
48	3	597	965 ± 13	1238 ± 16	966^{+90}_{-30}	- (14.3 - 20.2)	28^{+5}_{-8}	18^{+3}_{-4}
48	4	426	554 ± 14	1538 ± 38	1207^{+105}_{-45}	- (17.8 - 25.1)	35^{+6}_{-11}	22^{+4}_{-5}
48	5	471	950 ± 13	992 ± 13	785^{+75}_{-30}	- (11.4 - 16.2)	23^{+4}_{-7}	14 ± 3
49	1	484	907 ± 28	1067 ± 33	845^{+75}_{-45}	- (12.3 - 17.4)	24^{+5}_{-7}	15 ± 3
49	2	197	464 ± 8	850 ± 15	664^{+75}_{-15}	- (9.8 - 13.9)	20^{+3}_{-6}	12^{+3}_{-2}
49	3	386	627 ± 10	1231 ± 20	966^{+90}_{-30}	-	28^{+5}_{-9}	18^{+3}_{-4}

Ev.ID	Lp.ID	L (Mm)	P (s)	v_{ph} (km s^{-1})	v_{Ai} (km s^{-1})	B_0 (G)	B_u (G)	B_G (G)
						(14.2 - 20.1)		
49	4	191	482 ± 11	793 ± 18	634^{+45}_{-30}	-	18^{+4}_{-5}	12^{+2}_{-3}
						(9.2 - 12.9)		
52	1	183	356 ± 7	1029 ± 21	815^{+75}_{-30}	-	23^{+5}_{-7}	15 ± 3
						(11.9 - 16.8)		
53	1	420	569 ± 13	1477 ± 34	1161^{+105}_{-45}	-	33^{+6}_{-10}	21^{+4}_{-5}
						(17.0 - 24.1)		
54	1	408	500 ± 4	1633 ± 14	1267^{+121}_{-30}	-	37^{+6}_{-12}	23 ± 5
						(18.8 - 26.6)		
54	2	400	448 ± 6	1787 ± 24	1387^{+136}_{-30}	-	40^{+7}_{-12}	25 ± 5
						(20.6 - 29.2)		
54	3	238	139 ± 3	3420 ± 74	2638^{+166}_{-90}	-	76^{+14}_{-23}	48 ± 10
						(39.5 - 55.8)		
54	4	355	226 ± 8	3139 ± 108	2457^{+196}_{-121}	-	70^{+14}_{-21}	43 ± 9
						(36.2 - 51.2)		
54	5	257	288 ± 6	1785 ± 37	1403^{+121}_{-60}	-	40^{+7}_{-12}	25 ± 5
						(20.6 - 29.1)		
55	1	405	518 ± 14	1564 ± 44	1222^{+121}_{-45}	-	35^{+7}_{-11}	22^{+4}_{-5}
						(18.1 - 25.5)		
55	2	477	392 ± 10	2431 ± 63	1900^{+181}_{-75}	-	55^{+10}_{-17}	34^{+7}_{-8}
						(28.1 - 39.7)		
56	1	403	544 ± 8	1481 ± 23	1161^{+105}_{-45}	-	33^{+7}_{-10}	21^{+4}_{-5}
						(17.1 - 24.2)		
56	2	314	713 ± 8	881 ± 10	694^{+60}_{-15}	-	20^{+4}_{-6}	13^{+2}_{-3}
						(10.2 - 14.4)		

Ev.ID	Lp.ID	L (Mm)	P (s)	v_{ph} (km s^{-1})	v_{Ai} (km s^{-1})	B_0 (G)	B_u (G)	B_G (G)
56	3	205	193 ± 10	2122 ± 105	1674^{+151}_{-105}	- (24.5 - 34.6)	48^{+10}_{-14}	30^{+6}_{-7}
56	4	501	863 ± 20	1161 ± 27	920^{+75}_{-45}	- (13.4 - 19.0)	26^{+5}_{-8}	17^{+3}_{-4}
56	5	431	810 ± 10	1064 ± 13	830^{+90}_{-15}	- (12.3 - 17.4)	24^{+5}_{-7}	15 ± 3
56	6	392	455 ± 12	1722 ± 45	1342^{+136}_{-45}	- (19.9 - 28.1)	39^{+7}_{-12}	24 ± 5
56	7	457	850 ± 33	1076 ± 42	845^{+90}_{-30}	- (12.4 - 17.6)	24^{+5}_{-7}	15^{+4}_{-3}
56	8	379	638 ± 9	1187 ± 17	935^{+90}_{-30}	- (13.7 - 19.4)	27^{+5}_{-8}	17^{+3}_{-4}

Columns present the event ID (Ev.ID) and loop ID (Lp.ID), the loop length (L), the period (P), the phase speed (v_{ph}), the inferred median values of the internal Alfvén velocity (v_{Ai}), the magnetic field strength from the cited references (B_0), the magnetic field strength under the uniform prior assumption (B_u), and the magnetic field strength under the Gaussian prior assumption (B_G). Plausible values of parameters are $v_{Ai} \in [1, 3000]$ km s^{-1}, $B \in [0.1, 100]$ G, $\zeta \in [1.1, 10]$, and $\rho_i \in [10^{-13}, 10^{-11}]$ kg m^{-3}.

Table B.1 shows a comparison between magnetic field strength estimates from previous works and summaries of posteriors using Bayesian analysis.

Note that exact values in Table B.1 come from computing v_{ph} values as $2L/P \pm \sqrt{(2\Delta L/P)^2 + (2L\Delta P/P^2)^2}$ for those references in which the phase speed was not computed. Events with neither uncertainty in L or P by Aschwanden et al. (2002) have been supposed to have an uncertainty of 10% in phase speed. In addition, note that to infer the magnetic field strength using Gaussian priors (last column of Table B.1), density measurements from the corresponding references have been taken, i.e. $\rho_i = 1.99 \times 10^{-12}(1 \pm 10^{-9})$ kg m^{-3} by Nakariakov & Ofman (2001), density values in Table III by Aschwanden et al. (2002), $\rho_i = (2.08 \pm 0.06) \times 10^{-12}$ kg m^{-3} by Van Doorsselaere et al. (2008b), and $\rho_i = 2.12 \times 10^{-12}$ kg m^{-3} with an associated uncertainty of 50% for the rest of events. Transformations to the SI have been implemented using a corrector factor of $\tilde{\mu} = 1.27$, except for Nakariakov & Ofman (2001) density which has been computed using a corrector factor equal to 1.16.

We found a discrepancy between our posterior summaries and previous magnetic field strength estimates in the events analysed by White & Verwichte (2012a). White & Verwichte (2012a) obtained possible ranges of variation for the magnetic field strength according to the inequalities

$$\frac{v_{ph}}{\sqrt{2}}\sqrt{\mu_0\rho_i} \leq B \leq v_{ph}\sqrt{\mu_0\rho_i}. \tag{B.1}$$

By inserting the previous values, we obtain the magnetic field strength ranges shown into parenthesis in Table B.1, which differ from the ranges in Table 3 by White & Verwichte (2012b) but agree well with our Bayesian posterior summaries using a Gaussian prior on density. Magnetic field strengths did not computed for events by (Verwichte et al. 2013) and (Goddard et al. 2016), but considering the inequality of (White & Verwichte 2012a) with the assumed density, $\rho_i = 2.12 \times 10^{-12}$ kg m^{-3}, we estimated the ranges visible in Table B.1.

To summarise results of inferred magnetic field strengths, we have represented them as a function of the period of wave and the length of the coronal loop in Fig. B.3. Clearly, resulting magnetic field strengths from the Gaussian prior condition are weakly in comparison to those from uniform prior and values are more constrained. In addition, inversely proportional dependency between the magnetic field strength and the period of the wave still remains present after Bayesian inference. Although the prior information of the density is important in the inference of the magnetic field strength, its effect combined with that from the length and the density contrast is less significant that the period of the wave is.

On the other hand, histograms of periods, loop lengths, and magnetic field

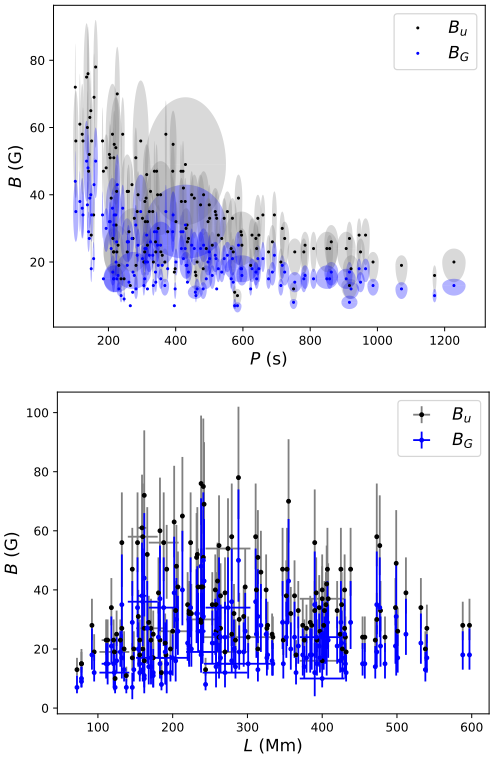

Figure B.3: Inferred median values of the magnetic field strength as a function of the period of wave (*left*) and the length of the loop (*right*). Ovoids and bars represent the associated uncertainty. Events of the previous table have been considered.

strengths (uniform priors) associated with events of Table B.1 have been acquired, in order to get a general idea of waves features observed in solar coronal loops. In Fig. B.4 it is appreciable that the majority of periods are of only few minutes, a great variety of coronal loop lengths have been observed, and magnetic field strengths from 20 to 40 G predominate in these structures.

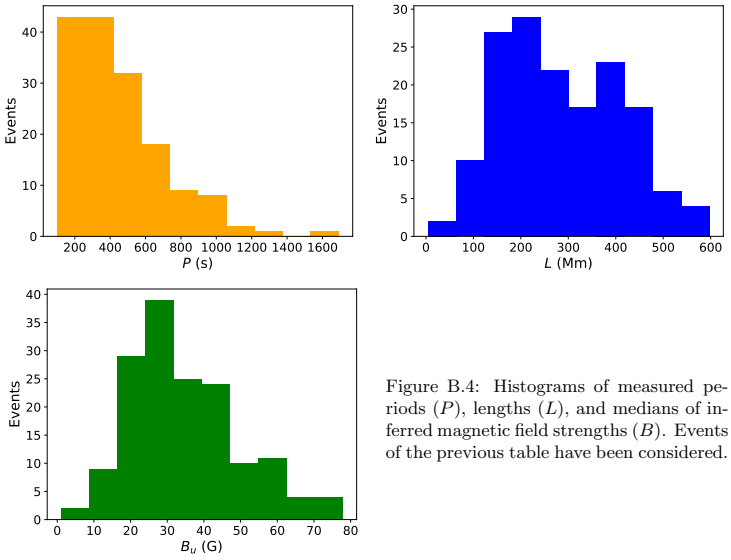

Figure B.4: Histograms of measured periods (P), lengths (L), and medians of inferred magnetic field strengths (B). Events of the previous table have been considered.

B.3 Computations with Monte Carlo methods

In Chapter 2, we showed how the integrals in the computation of posteriors and marginal likelihoods could be achieved by direct integration but also by Monte Carlo (MC) methods. In this section of the appendix, we present some examples of results already described in the main text by integrating directly but obtained here by MC methods (Section 2.6). First, we plotted in Fig. B.5 the marginal posterior distributions of the parameters corresponding to the three damping models, when $\tau_d/P = 3.0 \pm 0.3$ is considered. In addition, we have added in Table B.2 the median results of those distributions resulting by direct integration and MCMC sampling to search for possible differences. However, as we mentioned before, it is appreciable as differences between both integration methods do not exist.

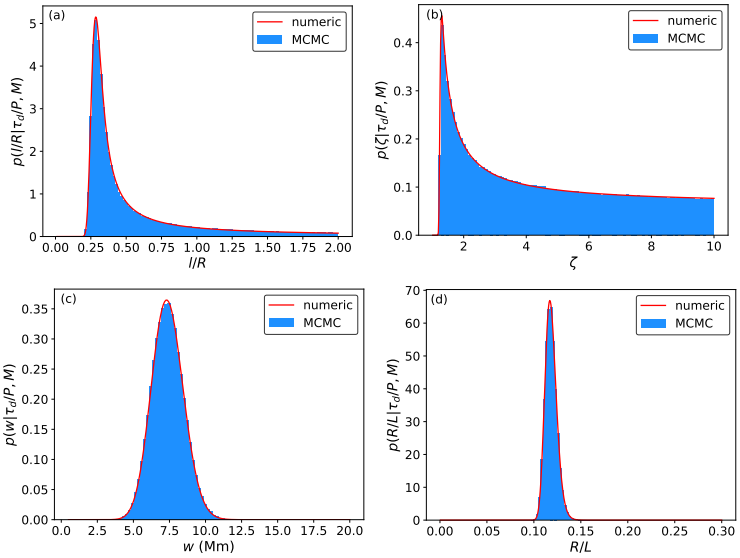

Figure B.5: Marginal posterior distributions of parameters associated to resonant absorption, phase mixing, and wave leakage. Numerical integration (red) and MCMC sampling (blue) have been applied to the case with $\tau_d = 3 \pm 0.3$.

On the other hand, in Chapter 2, we further indicated that marginal likelihoods can be equally well acquired by means of MC integration. Figure B.6

Method	ζ	l/R	w (Mm)	R/L
Numeric	4^{+4}_{-2}	$0.4^{+0.5}_{-0.2}$	8 ± 1	0.12 ± 0.01
MCMC	4^{+4}_{-3}	$0.4^{+0.5}_{-0.1}$	7 ± 1	0.12 ± 0.01

Table B.2: Inferred parameters from Figure B.5.

represents one example of marginal likelihoods computed by both, direct and MC integrations. In particular, the represented distributions correspond to the three plausible damping models, resonant absorption, phase mixing ($P = 150$ s), and wave leakage. The results confirm the goodness of MC integration to compute marginal likelihoods.

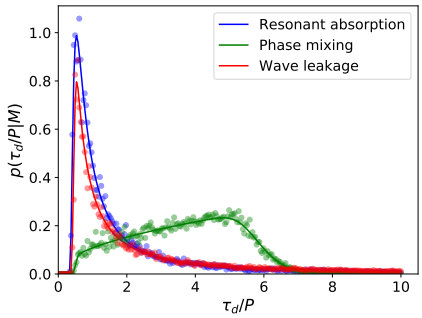

Figure B.6: Comparison between the marginal likelihoods obtained by direct numerical integration (continuous lines) and the MC integration (filled circles) for resonant absorption, phase mixing, and wave leakage as a function of the observable damping ratio with uncertainty of 10%. For phase mixing, $P = 150$ s is fixed.

These two examples demonstrate that the MC methods applied to Bayesian coronal seismology can be confidently used to integrate when the dimension of the parameter space is too large for direct integration to be feasible.

B.4 Summary of inferred damping parameters and Bayes factors

Table B.3: Transverse loop oscillations data, inference results and Bayes factors.

Ref	Ev.ID	Lp.ID	P (s)	τ_d (s)	τ_d/P	l/R	ζ	w (Mm)	R/L	$2lnBF_{01}$	$2lnBF_{02}$	$2lnBF_{12}$
1	24	...	895 ± 2	521 ± 8	0.6 ± 0.1	$1.5^{+0.3}_{-0.1}$	7 ± 2	1.6 ± 0.1	0.27 ± 0.01	3.45	0.48	−2.97
2	10	1	688 ± 10	481 ± 65	0.7 ± 0.1	$1.4^{+0.3}_{-0.2}$	6^{+3}_{-2}	$1.9^{+0.4}_{-0.3}$	0.25 ± 0.02	2.80	0.56	−2.24
2	56	7	850 ± 33	818 ± 236	1.0 ± 0.3	$1.2^{+0.5}_{-0.3}$	6 ± 3	3^{+2}_{-1}	$0.22^{+0.04}_{-0.03}$	1.43	0.56	−0.87
2	48	3	965 ± 13	946 ± 185	1.0 ± 0.2	$1.1^{+0.4}_{-0.3}$	6 ± 3	4 ± 1	$0.21^{+0.03}_{-0.02}$	1.21	0.56	−0.65
2	9	1	308 ± 10	305 ± 59	1.0 ± 0.2	$1.1^{+0.4}_{-0.3}$	6 ± 3	2.2 ± 0.6	$0.21^{+0.03}_{-0.02}$	2.31	0.56	−1.75
1	40	...	302 ± 14	306 ± 43	1.0 ± 0.1	$1.0^{+0.4}_{-0.2}$	5 ± 3	$2.2^{+0.5}_{-0.4}$	0.21 ± 0.02	2.18	0.56	−1.62
1	44	...	1170 ± 6	1218 ± 48	1.0 ± 0.1	$0.9^{+0.5}_{-0.1}$	5 ± 3	$4.2^{+0.3}_{-0.2}$	0.20 ± 0.01	0.62	0.55	−0.07
1	25	...	452 ± 1	473 ± 6	1.0 ± 0.1	$0.9^{+0.5}_{-0.1}$	5 ± 3	2.8 ± 0.1	0.20 ± 0.01	1.57	0.55	−1.02
2	43	1	428 ± 4	452 ± 87	1.1 ± 0.2	$1.0^{+0.5}_{-0.2}$	5 ± 3	$2.8^{+0.8}_{-0.7}$	$0.21^{+0.03}_{-0.02}$	1.72	0.55	−1.18
1	32	...	216 ± 27	230 ± 23	1.1 ± 0.2	$1.0^{+0.4}_{-0.2}$	5 ± 3	$2.0^{+0.5}_{-0.4}$	0.20 ± 0.02	2.32	0.55	−1.78
1	29	...	225 ± 40	240 ± 45	1.1 ± 0.3	$1.1^{+0.5}_{-0.3}$	6 ± 3	$2.1^{+0.8}_{-0.7}$	$0.21^{+0.04}_{-0.02}$	2.40	0.54	−1.85
2	3	2	217 ± 5	247 ± 28	1.1 ± 0.1	$0.9^{+0.4}_{-0.2}$	5 ± 3	$2.2^{+0.4}_{-0.3}$	0.19 ± 0.01	1.97	0.52	−1.45
2	16	2	141 ± 4	161 ± 38	1.1 ± 0.3	$1.0^{+0.5}_{-0.3}$	5 ± 3	1.9 ± 0.6	$0.20^{+0.03}_{-0.02}$	2.57	0.53	−2.04
2	49	5	482 ± 11	562 ± 73	1.2 ± 0.2	$0.9^{+0.5}_{-0.2}$	5 ± 3	3.3 ± 0.6	$0.19^{+0.02}_{-0.01}$	1.09	0.51	−0.57
1	31	...	213 ± 9	251 ± 36	1.2 ± 0.2	$0.9^{+0.5}_{-0.2}$	5 ± 3	2.3 ± 0.5	$0.19^{+0.02}_{-0.01}$	1.88	0.51	−1.37
1	41	...	565 ± 4	666 ± 42	1.2 ± 0.1	$0.8^{+0.5}_{-0.1}$	5 ± 3	$3.6^{+0.3}_{-0.4}$	0.19 ± 0.01	0.82	0.50	−0.31
2	23	1	922 ± 24	1151 ± 93	1.2 ± 0.1	$0.8^{+0.5}_{-0.1}$	5 ± 3	5.0 ± 0.6	0.18 ± 0.01	0.09	0.48	0.39
2	18	2	571 ± 7	732 ± 208	1.3 ± 0.4	$1.0^{+0.5}_{-0.3}$	5 ± 3	4 ± 2	$0.19^{+0.04}_{-0.03}$	0.76	0.50	−0.26
1	34	...	596 ± 50	771 ± 336	1.3 ± 0.6	$1.1^{+0.6}_{-0.4}$	6 ± 3	$4.9^{+2.9}_{-2.4}$	$0.20^{+0.06}_{-0.04}$	0.71	0.51	−0.20
2	44	3	417 ± 8	540 ± 180	1.3 ± 0.4	$1.0^{+0.6}_{-0.4}$	6 ± 3	4 ± 2	$0.20^{+0.05}_{-0.03}$	1.08	0.50	−0.57
2	9	2	537 ± 8	710 ± 286	1.3 ± 0.5	$1.1^{+0.6}_{-0.4}$	6 ± 3	5^{+3}_{-2}	$0.20^{+0.05}_{-0.04}$	0.76	0.51	−0.25
2	40	3	332 ± 2	439 ± 65	1.3 ± 0.2	$0.8^{+0.5}_{-0.2}$	5 ± 3	3.3 ± 0.7	$0.18^{+0.02}_{-0.01}$	0.92	0.46	−0.46

Ref	Ev.ID	Lp.ID	P (s)	τ_d (s)	τ_d/P	l/R	ζ	w (Mm)	R/L	$2lnBF_{01}$	$2lnBF_{02}$	$2lnBF_{12}$
1	30	...	215 ± 5	293 ± 18	1.4 ± 0.1	$0.7^{+0.5}_{-0.1}$	5 ± 3	$2.8^{+0.3}_{-0.2}$	0.18 ± 0.01	1.14	0.44	−0.70
1	35	...	212 ± 20	298 ± 30	1.4 ± 0.2	$0.8^{+0.5}_{-0.2}$	5 ± 3	2.9 ± 0.6	0.18 ± 0.01	1.09	0.43	−0.66
1	33	...	520 ± 5	735 ± 53	1.4 ± 0.1	$0.7^{+0.5}_{-0.1}$	5 ± 3	4.5 ± 0.5	0.17 ± 0.01	0.09	0.42	0.32
2	48	1	917 ± 10	1319 ± 936	1.4 ± 1.0	$1.1^{+0.6}_{-0.5}$	6 ± 3	8^{+6}_{-5}	$0.20^{+0.06}_{-0.05}$	−0.17	0.50	0.67
1	46	...	150 ± 5	216 ± 60	1.4 ± 0.4	$0.9^{+0.6}_{-0.3}$	5 ± 3	3 ± 1	$0.18^{+0.04}_{-0.02}$	1.62	0.46	−1.16
2	19	2	676 ± 7	993 ± 86	1.5 ± 0.1	$0.7^{+0.5}_{-0.1}$	5^{+4}_{-3}	$5.4^{+0.8}_{-0.7}$	0.17 ± 0.01	−0.33	0.40	0.73
2	49	4	627 ± 10	923 ± 155	1.5 ± 0.2	$0.8^{+0.5}_{-0.2}$	5 ± 3	5 ± 1	$0.17^{+0.02}_{-0.01}$	−0.15	0.42	0.57
2	44	2	587 ± 11	877 ± 298	1.5 ± 0.5	$0.9^{+0.6}_{-0.4}$	5 ± 3	6^{+3}_{-2}	$0.19^{+0.05}_{-0.03}$	0.19	0.46	0.28
1	27	...	2418 ± 5	3660 ± 80	1.5 ± 0.1	$0.7^{+0.5}_{-0.1}$	5^{+4}_{-3}	$10.6^{+0.4}_{-0.3}$	0.17 ± 0.01	−1.78	0.38	2.15
1	38	...	115 ± 2	175 ± 30	1.5 ± 0.3	$0.7^{+0.5}_{-0.2}$	5 ± 3	2.5 ± 0.6	0.17 ± 0.02	1.40	0.40	−1.00
2	24	1	1072 ± 18	1646 ± 256	1.5 ± 0.2	$0.7^{+0.5}_{-0.2}$	5^{+4}_{-3}	7 ± 2	$0.17^{+0.02}_{-0.01}$	−0.90	0.39	1.29
1	45	...	623 ± 4	960 ± 60	1.5 ± 0.1	$0.7^{+0.5}_{-0.1}$	5^{+4}_{-3}	5.6 ± 0.5	0.16 ± 0.01	−0.48	0.37	0.86
2	25	1	308 ± 7	480 ± 300	1.6 ± 1.0	$1.1^{+0.6}_{-0.5}$	6 ± 3	5^{+4}_{-3}	$0.20^{+0.06}_{-0.05}$	0.64	0.48	−0.16
2	1	1	205 ± 4	320 ± 67	1.6 ± 0.3	$0.8^{+0.5}_{-0.2}$	5 ± 3	3 ± 1	0.17 ± 0.02	0.79	0.40	−0.39
2	26	1	717 ± 8	1123 ± 270	1.6 ± 0.4	$0.8^{+0.5}_{-0.2}$	5 ± 3	6 ± 2	$0.17^{+0.03}_{-0.02}$	−0.39	0.41	0.81
1	26	...	630 ± 30	1000 ± 300	1.6 ± 0.5	$0.9^{+0.6}_{-0.3}$	5 ± 3	6^{+3}_{-2}	$0.18^{+0.05}_{-0.03}$	−0.18	0.43	0.61
2	56	2	713 ± 8	1177 ± 178	1.7 ± 0.2	$0.7^{+0.5}_{-0.2}$	5^{+4}_{-3}	7^{+2}_{-1}	$0.16^{+0.02}_{-0.01}$	−0.83	0.35	1.18
2	34	1	597 ± 16	1002 ± 62	1.7 ± 0.1	$0.6^{+0.5}_{-0.1}$	5^{+4}_{-3}	$6.2^{+0.7}_{-0.6}$	0.16 ± 0.01	−0.83	0.32	1.15
2	48	2	946 ± 7	1598 ± 130	1.7 ± 0.1	$0.6^{+0.5}_{-0.1}$	5^{+4}_{-3}	8 ± 1	0.16 ± 0.01	−1.31	0.32	1.63
1	50	...	491 ± 18	834 ± 6	1.7 ± 0.1	$0.6^{+0.5}_{-0.1}$	5^{+4}_{-3}	$5.7^{+0.4}_{-0.3}$	0.16 ± 0.01	−0.70	0.31	1.02
2	24	3	1228 ± 35	2101 ± 386	1.7 ± 0.3	$0.7^{+0.5}_{-0.2}$	5^{+4}_{-3}	9^{+3}_{-2}	0.16 ± 0.02	−1.46	0.35	1.81
1	48	...	273 ± 54	468 ± 36	1.7 ± 0.4	$0.7^{+0.5}_{-0.2}$	5^{+4}_{-3}	5 ± 1	0.16 ± 0.02	0.09	0.36	0.26
1	36	...	256 ± 22	444 ± 105	1.7 ± 0.4	$0.7^{+0.6}_{-0.2}$	5 ± 3	5 ± 2	$0.16^{+0.03}_{-0.02}$	0.22	0.37	0.16
2	56	5	810 ± 10	1450 ± 308	1.8 ± 0.4	$0.7^{+0.5}_{-0.2}$	5^{+4}_{-3}	8^{+3}_{-2}	0.16 ± 0.02	−1.19	0.34	1.52
2	43	3	501 ± 5	902 ± 109	1.8 ± 0.2	$0.6^{+0.5}_{-0.1}$	5^{+4}_{-3}	6 ± 1	0.15 ± 0.01	−0.92	0.29	1.22

Ref	Ev.ID	Lp.ID	P (s)	τ_d (s)	τ_d/P	l/R	ζ	w (Mm)	R/L	$2lnBF_{01}$	$2lnBF_{02}$	$2lnBF_{12}$
2	31	2	575 ± 5	1054 ± 141	1.8 ± 0.2	$0.6^{+0.5}_{-0.1}$	5^{+4}_{-3}	7^{+2}_{-1}	0.15 ± 0.01	-1.12	0.29	1.41
1	42	...	222 ± 18	420 ± 360	1.9 ± 1.6	1.1 ± 0.6	6 ± 3	7^{+6}_{-4}	$0.19^{+0.07}_{-0.06}$	0.21	0.44	0.23
1	43	...	474 ± 12	900 ± 120	1.9 ± 0.3	$0.6^{+0.5}_{-0.1}$	5^{+4}_{-3}	7 ± 1	0.15 ± 0.01	-1.09	0.27	1.36
2	40	8	260 ± 5	541 ± 130	2.1 ± 0.5	$0.6^{+0.5}_{-0.2}$	5^{+4}_{-3}	6 ± 2	$0.15^{+0.03}_{-0.02}$	-0.65	0.27	0.92
2	29	1	223 ± 3	470 ± 37	2.1 ± 0.2	$0.5^{+0.5}_{-0.1}$	4^{+4}_{-3}	$5.4^{+0.6}_{-0.7}$	0.14 ± 0.01	-0.89	0.19	1.07
2	40	9	371 ± 3	789 ± 160	2.1 ± 0.4	$0.6^{+0.5}_{-0.2}$	5^{+4}_{-3}	7 ± 2	$0.14^{+0.02}_{-0.01}$	-1.22	0.23	1.45
2	4	2	208 ± 1.8	446 ± 60	2.1 ± 0.3	$0.5^{+0.5}_{-0.1}$	5^{+4}_{-3}	5 ± 1	0.14 ± 0.01	-0.83	0.19	1.02
1	49	...	282 ± 6	606 ± 186	2.1 ± 0.7	$0.7^{+0.6}_{-0.3}$	5 ± 3	7 ± 3	$0.15^{+0.04}_{-0.02}$	-0.65	0.30	0.95
2	44	1	434 ± 4	945 ± 185	2.2 ± 0.4	$0.6^{+0.5}_{-0.2}$	5^{+4}_{-3}	8 ± 2	$0.14^{+0.02}_{-0.01}$	-1.50	0.22	1.72
2	56	1	544 ± 8	1243 ± 283	2.3 ± 0.5	$0.6^{+0.5}_{-0.2}$	5^{+4}_{-3}	10 ± 3	0.14 ± 0.02	-1.85	0.21	2.06
1	37	...	135 ± 9	311 ± 85	2.3 ± 0.6	$0.6^{+0.6}_{-0.2}$	5^{+4}_{-3}	5 ± 2	$0.15^{+0.04}_{-0.02}$	-0.30	0.25	0.55
1	39	...	103 ± 8	242 ± 114	2.3 ± 1.1	$0.9^{+0.7}_{-0.4}$	5 ± 3	5 ± 3	$0.17^{+0.07}_{-0.04}$	0.37	0.35	-0.02
2	40	7	343 ± 4	850 ± 164	2.5 ± 0.5	$0.5^{+0.5}_{-0.1}$	4^{+4}_{-3}	9 ± 2	$0.13^{+0.02}_{-0.01}$	-1.87	0.13	2.00
1	51	...	348 ± 7	906 ± 288	2.6 ± 0.8	$0.6^{+0.7}_{-0.3}$	5^{+4}_{-3}	10 ± 4	$0.14^{+0.05}_{-0.02}$	-1.61	0.22	1.83
2	1	2	247 ± 3	646 ± 167	2.6 ± 0.7	$0.5^{+0.6}_{-0.2}$	5^{+4}_{-3}	8 ± 3	$0.13^{+0.03}_{-0.02}$	-1.57	0.16	1.72
2	43	2	216 ± 2	566 ± 55	2.6 ± 0.3	$0.4^{+0.5}_{-0.1}$	4^{+4}_{-2}	7 ± 1	0.13 ± 0.01	-1.85	0.05	1.90
2	8	1	224 ± 4	600 ± 60	2.7 ± 0.3	$0.4^{+0.5}_{-0.1}$	4^{+4}_{-2}	8 ± 1	0.13 ± 0.01	-1.97	0.04	2.01
1	52	...	340 ± 3	930 ± 144	2.7 ± 0.4	$0.4^{+0.5}_{-0.1}$	4^{+4}_{-2}	10 ± 2	0.13 ± 0.01	-2.41	0.05	2.46
1	13	...	448 ± 18	1260 ± 500	2.8 ± 1.1	$0.7^{+0.7}_{-0.4}$	5 ± 3	12 ± 5	$0.15^{+0.07}_{-0.03}$	-1.58	0.25	1.83
1	47	...	122 ± 6	348 ± 360	2.9 ± 3.0	$1.0^{+0.7}_{-0.6}$	6 ± 3	9^{+7}_{-6}	$0.18^{+0.08}_{-0.07}$	-0.21	0.36	0.57
1	16	...	358 ± 30	1030 ± 570	2.9 ± 1.6	$0.9^{+0.7}_{-0.5}$	5 ± 3	11 ± 6	$0.16^{+0.08}_{-0.05}$	-0.99	0.32	1.31
2	38	2	312 ± 5	914 ± 330	2.9 ± 1.1	$0.7^{+0.7}_{-0.3}$	5^{+4}_{-3}	11 ± 5	$0.14^{+0.06}_{-0.03}$	-1.72	0.20	1.92
1	17	...	326 ± 45	980 ± 400	3.0 ± 1.3	$0.7^{+0.8}_{-0.4}$	5 ± 3	11 ± 5	$0.15^{+0.08}_{-0.03}$	-1.46	0.25	1.71
2	20	1	322 ± 14	971 ± 460	3.0 ± 1.4	$0.8^{+0.7}_{-0.4}$	5 ± 3	11 ± 6	$0.15^{+0.08}_{-0.04}$	-1.28	0.27	1.55
2	43	5	270 ± 1	840 ± 120	3.1 ± 0.4	$0.4^{+0.5}_{-0.1}$	4^{+4}_{-2}	11 ± 2	0.12 ± 0.01	-2.80	-0.05	2.76

Ref	Ev.ID	Lp.ID	P (s)	τ_d (s)	τ_d/P	l/R	ζ	w (Mm)	R/L	$2lnBF_{01}$	$2lnBF_{02}$	$2lnBF_{12}$
2	4	1	137 ± 2	431 ± 90	3.1 ± 0.7	$0.4^{+0.5}_{-0.1}$	4^{+4}_{-3}	8 ± 2	$0.12^{+0.02}_{-0.01}$	-2.00	-0.01	2.00
2	45	1	149 ± 2	469 ± 100	3.2 ± 0.7	$0.4^{+0.5}_{-0.1}$	4^{+4}_{-3}	8^{+3}_{-2}	$0.12^{+0.02}_{-0.01}$	-2.10	-0.01	2.09
2	31	1	460 ± 2	1453 ± 121	3.2 ± 0.3	$0.4^{+0.5}_{-0.1}$	4^{+4}_{-2}	14 ± 2	0.12 ± 0.01	-3.49	-0.08	3.41
2	11	3	156 ± 3	530 ± 90	3.4 ± 0.6	$0.4^{+0.5}_{-0.1}$	4^{+4}_{-2}	9 ± 2	0.11 ± 0.01	-2.61	-0.09	2.52
1	15	...	382 ± 12	1330 ± 528	3.5 ± 1.4	$0.7^{+0.8}_{-0.3}$	5 ± 3	13^{+5}_{-6}	$0.13^{+0.07}_{-0.03}$	-1.81	0.16	1.97
2	3	1	148 ± 2	528 ± 108	3.6 ± 0.7	$0.4^{+0.5}_{-0.1}$	4^{+4}_{-2}	10 ± 3	$0.11^{+0.02}_{-0.01}$	-2.70	-0.10	2.60
2	32	1	257 ± 1	933 ± 73	3.6 ± 0.3	$0.3^{+0.5}_{-0.1}$	4^{+4}_{-2}	13 ± 2	0.11 ± 0.01	-3.57	-0.18	3.39
1	12	...	249 ± 33	920 ± 360	3.7 ± 1.5	$0.7^{+0.8}_{-0.4}$	5^{+4}_{-3}	12^{+5}_{-6}	$0.13^{+0.08}_{-0.03}$	-1.81	0.15	1.96
1	18	...	357 ± 89	1320 ± 720	3.7 ± 2.2	$0.9^{+0.7}_{-0.5}$	5 ± 3	12 ± 6	$0.16^{+0.09}_{-0.05}$	-1.01	0.26	1.27
2	54	5	288 ± 6	1183 ± 194	4.1 ± 0.7	$0.3^{+0.5}_{-0.1}$	4^{+4}_{-2}	16 ± 3	0.10 ± 0.01	-3.68	-0.23	3.45
2	7	1	101 ± 1	434 ± 78	4.3 ± 0.8	$0.3^{+0.5}_{-0.1}$	4^{+4}_{-2}	11 ± 3	0.10 ± 0.01	-3.24	-0.25	2.99
2	40	2	337 ± 2	1490 ± 205	4.4 ± 0.6	$0.3^{+0.5}_{-0.1}$	4^{+4}_{-2}	17^{+2}_{-3}	0.10 ± 0.01	-3.35	-0.30	3.06
1	14	...	392 ± 31	1830 ± 790	4.7 ± 2.0	$0.6^{+0.8}_{-0.4}$	5^{+4}_{-3}	14^{+5}_{-6}	$0.13^{+0.09}_{-0.03}$	-1.45	0.09	1.53
2	17	1	124 ± 2	599 ± 275	4.8 ± 2.2	$0.7^{+0.8}_{-0.4}$	5 ± 3	12^{+5}_{-6}	$0.13^{+0.09}_{-0.04}$	-1.78	0.10	1.88
1	22	...	436 ± 5	2129 ± 280	4.9 ± 0.6	$0.2^{+0.5}_{-0.1}$	4^{+4}_{-2}	18^{+1}_{-2}	0.09 ± 0.01	-0.88	-0.37	0.51
1	23	...	243 ± 6	1200	4.9 ± 0.1	$0.2^{+0.5}_{-0.1}$	4^{+4}_{-2}	$19.4^{+0.5}_{-0.6}$	0.09 ± 0.01	-4.20	-0.38	3.82
2	32	2	203 ± 1	1147 ± 291	5.7 ± 1.4	$0.3^{+0.5}_{-0.1}$	4^{+4}_{-2}	16^{+3}_{-5}	$0.09^{+0.02}_{-0.01}$	-2.89	-0.35	2.53

*Columns present the reference (Ref), the event ID (Ev.ID) and loop ID (Lp.ID) from references, the observed period (P), the damping time (τ_d), damping rate (τ), the parameter inferred median values of the three selected theoretical models (ζ, l/R, w, R/L) with their uncertainties, and Bayes factor. The symbol (*) indicates Positive Evidence according to the corresponding Bayes factor.
(1) Verwichte et al. (2013); (2) Goddard et al. (2016)

Bibliography

Andries, J., Arregui, I., & Goossens, M. 2005, ApJ, 624, L57

Andries, J., Van Doorsselaere, T., Roberts, B., et al. 2009, Space Sci. Rev., 149, 3

Anfinogentov, S., Nisticò, G., & Nakariakov, V. M. 2013, A&A, 560, A107

Anfinogentov, S. A., Nakariakov, V. M., & Nisticò, G. 2015, A&A, 583, A136

Arregui, I. 2018, Advances in Space Research, 61, 655

Arregui, I., Andries, J., Van Doorsselaere, T., Goossens, M., & Poedts, S. 2007, A&A, 463, 333

Arregui, I., & Asensio Ramos, A. 2011, ApJ, 740, 44

—. 2014, A&A, 565, A78

Arregui, I., Asensio Ramos, A., & Díaz, A. J. 2013a, ApJ, 765, L23

Arregui, I., Asensio Ramos, A., & Pascoe, D. J. 2013b, ApJ, 769, L34

—. 2013c, ApJ, 769, L34

Arregui, I., & Ballester, J. L. 2011, Space Science Reviews, 158, 169

Arregui, I., Ballester, J. L., & Goossens, M. 2008, ApJ, 676, L77

Arregui, I., Oliver, R., & Ballester, J. L. 2012, Living Reviews in Solar Physics, 9, 2

—. 2018, Living Reviews in Solar Physics, 15, 3

Arregui, I., & Soler, R. 2015, A&A, 578, A130

Arregui, I., Soler, R., & Asensio Ramos, A. 2015, ApJ, 811, 104

Arregui, I., Soler, R., Ballester, J. L., & Wright, A. N. 2011, A&A, 533, A60

Arregui, I., Van Doorsselaere, T., Andries, J., Goossens, M., & Kimpe, D. 2005, A&A, 441, 361

Aschwanden, M. J. 1987, Sol. Phys., 111, 113

—. 2005, Physics of the Solar Corona. An Introduction with Problems and Solutions (2nd edition) (Springer-Praxis)

—. 2006, Philosophical Transactions of the Royal Society of London Series A, 364, 417

Aschwanden, M. J., de Pontieu, B., Schrijver, C. J., & Title, A. M. 2002, Sol. Phys., 206, 99

Aschwanden, M. J., Fletcher, L., Schrijver, C. J., & Alexander, D. 1999, ApJ, 520, 880

Aschwanden, M. J., & Schrijver, C. J. 2011, ApJ, 736, 102

Asensio Ramos, A., & Arregui, I. 2013, A&A, 554, A7

Asensio Ramos, A., & Arregui, I. 2018, Bayesian Astrophysics, Canary Islands Winter School of Astrophysics (Cambridge University Press)

Ballester, J. L., Carbonell, M., Soler, R., & Terradas, J. 2018, A&A, 609, A6

Bayes, M., & Price, M. 1763, Royal Society of London Philosophical Transactions Series I, 53, 370

Berger, T. E., Shine, R. A., Slater, G. L., et al. 2008, ApJ, 676, L89

Berghmans, D., & de Bruyne, P. 1995, ApJ, 453, 495

Cally, P. S. 1986, Sol. Phys., 103, 277

—. 2003, Sol. Phys., 217, 95

—. 2017, MNRAS, 466, 413

Cally, P. S., & Maddison, S. T. 1997, Journal of Plasma Physics, 57, 591

Carbonell, M., Oliver, R., & Ballester, J. 2009, New Astronomy, 14, 277

Carbonell, M., Oliver, R., & Ballester, J. L. 2004, A&A, 415, 739

Carbonell, M., Terradas, J., Oliver, R., & Ballester, J. L. 2006, A&A, 460, 573

Chen, F., & Peter, H. 2015, A&A, 581, A137

De Moortel, I. 2005, Philosophical Transactions of the Royal Society of London Series A, 363, 2743

De Moortel, I., & Brady, C. S. 2007, ApJ, 664, 1210

De Moortel, I., Hood, A. W., & Ireland, J. 2002a, A&A, 381, 311

De Moortel, I., Hood, A. W., Ireland, J., & Walsh, R. W. 2002b, Sol. Phys., 209, 89

De Moortel, I., Ireland, J., & Walsh, R. W. 2000, A&A, 355, L23

De Moortel, I., & Nakariakov, V. M. 2012, Philosophical Transactions of the Royal Society of London Series A, 370, 3193

De Moortel, I., & Pascoe, D. J. 2009, ApJ, 699, L72

De Pontieu, B., Martens, P. C. H., & Hudson, H. S. 2001, ApJ, 558, 859

Díaz, A. J., Oliver, R., & Ballester, J. L. 2002, ApJ, 580, 550

—. 2010, ApJ, 725, 1742

Díaz, A. J., Oliver, R., Erdélyi, R., & Ballester, J. L. 2001, A&A, 379, 1083

Dymova, M. V., & Ruderman, M. S. 2005, Sol. Phys., 229, 79

Edwin, P. M., & Roberts, B. 1983, Sol. Phys., 88, 179

Evans, M., & Swartz, T. 1995, Statist. Sci., 10, 254

Forteza, P., Oliver, R., & Ballester, J. L. 2008, A&A, 492, 223

Forteza, P., Oliver, R., Ballester, J. L., & Khodachenko, M. L. 2007, A&A, 461, 731

Foullon, C., Verwichte, E., & Nakariakov, V. M. 2004, A&A, 427, L5

Gelman, A., Carlin, J., Stern, H., et al. 2013, Bayesian Data Analysis, Chapman & Hall/CRC Texts in Statistical Science (CRC Press)

Gelman, A., & Hennig, C. 2015, arXiv e-prints, arXiv:1508.05453

Goddard, C. R., Nisticò, G., Nakariakov, V. M., & Zimovets, I. V. 2016, A&A, 585, A137

Golub, L., & Pasachoff, J. M. 1997, The Solar Corona

Goodman, J., & Weare, J. 2010, Communications in Applied Mathematics and Computational Science, 5, 65

Goossens, M., Andries, J., & Arregui, I. 2006, Philosophical Transactions of the Royal Society of London Series A, 364, 433

Goossens, M., Andries, J., & Aschwanden, M. J. 2002, A&A, 394, L39

Goossens, M., Arregui, I., Ballester, J. L., & Wang, T. J. 2008, A&A, 484, 851

Goossens, M., Erdélyi, R., & Ruderman, M. S. 2011, Space Sci. Rev., 158, 289

Goossens, M., Hollweg, J. V., & Sakurai, T. 1992, Sol. Phys., 138, 233

Goossens, M., Ruderman, M. S., & Hollweg, J. V. 1995, Sol. Phys., 157, 75

Goossens, M., Soler, R., Arregui, I., & Terradas, J. 2012, ApJ, 760, 98

Gregory, P. 2005, Bayesian Logical Data Analysis for the Physical Sciences: A Comparative Approach with Mathematica® Support (Cambridge University Press), doi:10.1017/CBO9780511791277

Gregory, P. C. 2005, Bayesian Logical Data Analysis for the Physical Sciences: A Comparative Approach with 'Mathematica' Support (Cambridge University Press)

Guillermier, P., & Koutchmy, S. 1999, Total Eclipses: Science, Observations, Myths and Legends, Springer Praxis Books (Springer London)

Heyvaerts, J., & Priest, E. R. 1983, A&A, 117, 220

Hollweg, J. V., & Yang, G. 1988, Journal of Geophysical Research, 93, 5423

Hood, A. W., Ruderman, M., Pascoe, D. J., et al. 2013, A&A, 551, A39

Hori, K., Ichimoto, K., & Sakurai, T. 2007, in New Solar Physics with Solar-B Mission ASP Conference Series, Vol. 369, proceedings of the conference held 8-11 November, 2005 at The Kyoto International Community House, Kyoto, Japan. Edited by Kazunari Shibata, Shin'ichi Nagata, Takashi Sakurai. San Francisco: Astronomical Society of the Pacific, 2007., p.213, Vol. 369, 213

Isobe, H., & Tripathi, D. 2006, A&A, 449, L17

Jeffreys, F., & Jeffreys, H. 1973, Scientific Inference (Cambridge University Press)

Joarder, P. S., Nakariakov, V. M., & Roberts, B. 1997, Sol. Phys., 173, 81

Kass, R. E., & Raftery, A. E. 1995, JASA, 90, 773

Klimchuk, J. A., Patsourakos, S., & Cargill, P. J. 2008, ApJ, 682, 1351

Laplace, P. 1774, l'Academie Royale des Sciences, 6, 621

Leake, J. E. 2005, in ESA Special Publication, Vol. 600, The Dynamic Sun: Challenges for Theory and Observations, 13.1

Lin, Y. 2004, PhD thesis, University of Oslo, Norway

Lin, Y., Engvold, O., der Voort, L. R. v., Wiik, J. E., & Berger, T. E. 2005, Solar Physics, 226, 239

Lin, Y., Engvold, O., Rouppe van der Voort, L. H. M., & van Noort, M. 2007, Sol. Phys., 246, 65

Lin, Y., Martin, S. F., Engvold, O., Rouppe van der Voort, L. H. M., & van Noort, M. 2008, Advances in Space Research, 42, 803

Lin, Y., Soler, R., Engvold, O., et al. 2009, ApJ, 704, 870

MacKay, D. J. C. 2003, IEEE Transactions on Information Theory, 50, 2544

McDougall, A. M. D., & Hood, A. W. 2007, Sol. Phys., 246, 259

McLaughlin, J. A., & Hood, A. W. 2006, A&A, 459, 641

Montes-Solís, M., & Arregui, I. 2019a, in Highlights on Spanish Astrophysics X, 514–519

Montes-Solís, M., & Arregui, I. 2019b, A&A, 622, A88

Montes-Solís, M., & Arregui, I. 2017, The Astrophysical Journal, 846, 89

Morton, R. J., Verth, G., Hillier, A., & Erdélyi, R. 2014, ApJ, 784, 29

Mrozek, T. 2011, Solar Phys, 270, 191

Nakariakov, V. M. 2008, in Journal of Physics Conference Series, Vol. 118, 012038

Nakariakov, V. M., & Ofman, L. 2001, A&A, 372, L53

Nakariakov, V. M., Ofman, L., DeLuca, E. E., Roberts, B., & Davila, J. M. 1999, Science, 285, 862

Nakariakov, V. M., & Verwichte, E. 2005, Living Reviews in Solar Physics, 2, 3

Nakariakov, V. M., Verwichte, E., Berghmans, D., & Robbrecht, E. 2000, A&A, 362, 1151

Nightingale, R. W., Aschwanden, M. J., & Hurlburt, N. E. 1999, Sol. Phys., 190, 249

Ning, Z., Cao, W., Okamoto, T. J., Ichimoto, K., & Qu, Z. Q. 2009, A&A, 499, 595

Nisticò, G., Nakariakov, V. M., & Verwichte, E. 2013, A&A, 552, doi:10.1051/0004-6361/201220676

Ofman, L. 2002, ApJ, 568, L135

Ofman, L., & Aschwanden, M. J. 2002, ApJ, 576, L153

Okamoto, T., Tsuneta, S., Berger, T., et al. 2007, Science, 318, 1577

Okamoto, T. J., Antolin, P., De Pontieu, B., et al. 2015, ApJ, 809, 71

Oliver, R., & Ballester, J. L. 2002, Sol. Phys., 206, 45

Pagano, P., & De Moortel, I. 2017, A&A, 601, A107

Pagano, P., Pascoe, D. J., & De Moortel, I. 2018, A&A, 616, A125

Pascoe, D. J., Anfinogentov, S., Nisticò, G., Goddard, C. R., & Nakariakov, V. M. 2017a, A&A, 600, A78

Pascoe, D. J., & De Moortel, I. 2014, ApJ, 784, 101

Pascoe, D. J., Goddard, C. R., Anfinogentov, S., & Nakariakov, V. M. 2017b, A&A, 600, L7

Pascoe, D. J., Hood, A. W., de Moortel, I., & Wright, A. N. 2012, A&A, 539, A37

Pascoe, D. J., Hood, A. W., De Moortel, I., & Wright, A. N. 2013, A&A, 551, A40

Pascoe, D. J., Wright, A. N., & De Moortel, I. 2010, ApJ, 711, 990

Priest, E. R. 1982, Solar magneto-hydrodynamics

Reale, F. 2014, Living Reviews in Solar Physics, 11, 4

Robert, C., & Casella, G. 2011, Statist. Sci., 26, 102

Robert, C. P., & Casella, G. 2004, Monte Carlo Integration (New York, NY: Springer New York), 79–122

Roberts, B. 2000, Sol. Phys., 193, 139

Roberts, B., Edwin, P. M., & Benz, A. O. 1984, ApJ, 279, 857

Ruderman, M. S. 2003, A&A, 409, 287

Ruderman, M. S. 2005, in ESA Special Publication, Vol. 600, The Dynamic Sun: Challenges for Theory and Observations, 96.1

Ruderman, M. S., & Erdélyi, R. 2009, Space Sci. Rev., 149, 199

Ruderman, M. S., & Petrukhin, N. S. 2017, A&A, 600, A122

Ruderman, M. S., & Roberts, B. 2002a, in Solar Variability: From Core to Outer Frontiers, ed. A. Wilson, Vol. 2, 745–748

Ruderman, M. S., & Roberts, B. 2002b, ApJ, 577, 475

Rusland, N. F., Wahid, N., Kasim, S., & Hafit, H. 2017, IOP Conference Series: Materials Science and Engineering, 226, 012091

Safari, H., Nasiri, S., & Sobouti, Y. 2007, A&A, 470, 1111

Sakurai, T., Goossens, M., & Hollweg, J. V. 1991, Sol. Phys., 133, 227

Schrijver, C. J., Aschwanden, M. J., & Title, A. M. 2002, Sol. Phys., 206, 69

Schutgens, N. A. J. 1997a, A&A, 323, 969

—. 1997b, A&A, 325, 352

Schutgens, N. A. J., & Tóth, G. 1999, A&A, 345, 1038

Selwa, M., Ofman, L., & Solanki, S. K. 2011, ApJ, 726, 42

Sharma, S. 2017, Annual Review of Astronomy and Astrophysics, 55, 213

Smith, J. M., Roberts, B., & Oliver, R. 1997, A&A, 317, 752

Soler, R. 2010, PhD thesis, Universitat de les Illes Balears, Spain

Soler, R., Arregui, I., Oliver, R., & Ballester, J. L. 2010, ApJ, 722, 1778

Soler, R., & Goossens, M. 2011, A&A, 531, A167

Soler, R., Goossens, M., & Ballester, J. L. 2015, A&A, 575, A123

Soler, R., Goossens, M., Terradas, J., & Oliver, R. 2014, ApJ, 781, 111

Soler, R., Oliver, R., & Ballester, J. 2009, New Astronomy, 14, 238

Soler, R., Oliver, R., & Ballester, J. L. 2007, A&A, 471, 1023

—. 2008, ApJ, 684, 725

—. 2009a, ApJ, 693, 1601

—. 2009b, ApJ, 707, 662

—. 2011a, ApJ, 726, 102

Soler, R., Oliver, R., Ballester, J. L., & Goossens, M. 2009c, ApJ, 695, L166

Soler, R., & Terradas, J. 2015, The Astrophysical Journal, 803, 43

Soler, R., Terradas, J., & Goossens, M. 2011b, ApJ, 734, 80

Soler, R., Terradas, J., Verth, G., & Goossens, M. 2011c, ApJ, 736, 10

Spruit, H. 1982, Solar Phys., 75, 3

Tak, H., Ghosh, S. K., & Ellis, J. A. 2018, MNRAS, 481, 277

Tandberg-Hanssen, E. 1995, The nature of solar prominences, Vol. 199, doi:10.1007/978-94-017-3396-0

Terradas, J., Andries, J., & Goossens, M. 2007, Sol. Phys., 246, 231

Terradas, J., Arregui, I., Oliver, R., & Ballester, J. L. 2008, ApJ, 678, L153

Terradas, J., Carbonell, M., Oliver, R., & Ballester, J. L. 2005, A&A, 434, 741

Terradas, J., Goossens, M., & Verth, G. 2010, A&A, 524, A23

Terradas, J., Molowny-Horas, R., Wiehr, E., et al. 2002, A&A, 393, 637

Terradas, J., Oliver, R., & Ballester, J. L. 2006, ApJ, 650, L91

Tian, H., McIntosh, S. W., Pontieu, B. D., et al. 2011, The Astrophysical Journal, 738, 18

Tomczyk, S., & McIntosh, S. W. 2009, ApJ, 697, 1384

Tomczyk, S., McIntosh, S. W., Keil, S. L., et al. 2007, Science, 317, 1192

Tripathi, D., Isobe, H., & Jain, R. 2009, Space Sci. Rev., 149, 283

Trotta, R. 2008, Contemporary Physics, 49, 71

Tsubaki, T. 1988, in Solar and Stellar Coronal Structure and Dynamics, ed. R. C. Altrock, 140–149

Uchida, Y. 1970, Publications of the Astronomical Society of Japan, 22, 341

van den Oord, G. H. J., & Kuperus, M. 1992, Sol. Phys., 142, 113

van den Oord, G. H. J., Schutgens, N. A. J., & Kuperus, M. 1998, A&A, 339, 225

Van Doorsselaere, T., Andries, J., Poedts, S., & Goossens, M. 2004, ApJ, 606, 1223

Van Doorsselaere, T., Birtill, D. C. C., & Evans, G. R. 2009, A&A, 508, 1485

Van Doorsselaere, T., Nakariakov, V. M., & Verwichte, E. 2007, A&A, 473, 959

Van Doorsselaere, T., Nakariakov, V. M., & Verwichte, E. 2008a, ApJ, 676, L73

Van Doorsselaere, T., Nakariakov, V. M., Young, P. R., & Verwichte, E. 2008b, A&A, 487, L17

Van Doorsselaere, T., Wardle, N., Del Zanna, G., et al. 2011, ApJ, 727, L32

VanderPlas, J. 2014, arXiv e-prints, arXiv:1411.5018

Verth, G., & Erdélyi, R. 2008, A&A, 486, 1015

Verth, G., Terradas, J., & Goossens, M. 2010, ApJ, 718, L102

Verwichte, E., Aschwanden, M. J., Van Doorsselaere, T., Foullon, C., & Nakariakov, V. M. 2009, The Astrophysical Journal, 698, 397

Verwichte, E., Foullon, C., & Van Doorsselaere, T. 2010, The Astrophysical Journal, 717, 458

Verwichte, E., Marsh, M., Foullon, C., et al. 2010, ApJ, 724, L194

Verwichte, E., Nakariakov, V. M., Ofman, L., & Deluca, E. E. 2004, Sol. Phys., 223, 77

Verwichte, E., Van Doorsselaere, T., White, R. S., & Antolin, P. 2013, A&A, 552, A138

von Toussaint, U. 2011, Reviews of Modern Physics, 83, 943

Vršnak, B., Veronig, A. M., Thalmann, J. K., & Žic, T. 2007, A&A, 471, 295

Wang, T., Ofman, L., Davila, J. M., & Su, Y. 2012, ApJ, 751, L27

Wang, T., Solanki, S. K., Curdt, W., Innes, D. E., & Dammasch, I. E. 2002, ApJ, 574, L101

Wang, T. J., & Solanki, S. K. 2004, A&A, 421, 33

Wang, T. J., Solanki, S. K., Innes, D. E., Curdt, W., & Marsch, E. 2003, A&A, 402, L17

White, R. S., & Verwichte, E. 2012a, A&A, 537, A49

—. 2012b, A&A, 537, A49

White, R. S., Verwichte, E., & Foullon, C. 2012, A&A, 545, doi:10.1051/0004-6361/201219856

Yi, Z., & Engvold, O. 1991, Sol. Phys., 134, 275

Yi, Z., Engvold, O., & Keil, S. L. 1991, Sol. Phys., 132, 63

Zaqarashvili, T. V. 2003, A&A, 399, L15

Zirker, J. B., Engvold, O., & Martin, S. F. 1998, Nature, 396, 440

List of Figures

List of Tables